

Elastically Averaged Precision Alignment

by

Patrick Willoughby

B. S. Mechanical Engineering
University of Pittsburgh, 2000

S.M. Mechanical Engineering
Massachusetts Institute of Technology, 2001

Submitted to the Department of Mechanical Engineering
in Partial Fulfillment of the Requirements for the Degree of

Doctor of Philosophy in Mechanical Engineering
at the
Massachusetts Institute of Technology

June 2005

© 2005 Massachusetts Institute of Technology
All Rights Reserved

Signature of Author
Department of Mechanical Engineering
May 6, 2005

Certified by
Alexander H. Slocum
Professor of Mechanical Engineering
Thesis Supervisor

Accepted by
Lallit Anand
Chairman, Department Committee on Graduate Students

(This page is intentionally left blank.)

Elastically Averaged Precision Alignment

by

PATRICK WILLOUGHBY

Submitted to the Department of Mechanical Engineering
on May 20, 2005 in Partial Fulfillment of the
Requirements for the Degree of Doctor of Philosophy in
Mechanical Engineering

ABSTRACT

One of the most important steps in designing a machine is the consideration of the effect of interfaces between components. A badly designed interface can vary from costly difficulties such as additional control or calibration to machine failure. For precision assemblies such as automobile engines, robotics, and many measurement devices, exact constraint techniques have been used to align removable components. Exact constraint typically requires controlled precision machining to allow an interface to be repeatable and interchangeable. Elastic averaging techniques can be used instead of exact constraint to create less repeatable interfaces with more generous machining requirements. Elastic averaging represents a subset of coupling types where improved accuracy is derived from the averaging of errors over a large number of relatively compliant contacting members. Repeatability and accuracy obtained through elastic averaging can be nearly as high as in deterministic systems, elastic averaging design allows for higher stiffness and lower local stress when compared to kinematic couplings. In this thesis, a model of elastic averaging has been developed to predict the effects of manufacturing variations on design. To demonstrate the capabilities of this model, a new fiber optic connector has been designed with elastic averaging and precision injection molding in mind. Simulations predict repeatability of approximately 5 micrometers for a 5X scale version, which agreed with experimental measurements. Fidelity parts were produced using the Silicon Insert Molded Plastics process (SIMP). SIMP uses microfabricated silicon inserts in a traditional injection mold to create parts with micro-scale features. The SIMP fidelity parts were measured to estimate manufacturing repeatability of approximately 5 micrometers. Using this repeatability, simulations predict that the actual scale version has repeatability of approximately 0.5 micrometers.

Thesis Supervisor:
Prof. Alexander H. Slocum
Professor of Mechanical Engineering, Massachusetts Institute of Technology

(This page is intentionally left blank.)

ACKNOWLEDGMENTS

First, I would like to thank Prof. Alex Slocum for his guidance and mentoring throughout my academic career, as well as the unique independence and responsibilities he allowed me. I have learned much from the many experiences working with him that I could not have received working for anyone else.

Next, I would like to thank my committee members Professor Martin Culpepper and Professor Samir Nayfeh of MIT, Dr. Sepehr Kiani of Teradyne, and Dr. William Plummer of WTP Optics. Thanks to Samir for making me step back and look at the simple case and for Marty for making me look at the whole.

I would like to thank my mother Audrey Willoughby for providing the LEGOs and an educational background which has allowed me to get as far as I have. She also receives a great deal of thanks for constantly keeping my remote control and VCR programming skills current.

I would also like to acknowledge the people at MIT who made my time at MIT enjoyable, including Gerry Wentworth of the LMP machine shop, the Pappalardo shop guys, the members of PERG, and Maureen Lynch.

The last, but definitely not least, person deserving acknowledgements is Jaime Werkmeister of MIT. Her work on the SIMP process kept me from having to enter the MTL fab and her connection to her father's company made progress on SIMP and the fiber optic connector much quicker. JaimeB also helped make sure that we both managed to see more of Boston than the wall inside MIT. Her companionship around the world has made trips much more entertaining, from the Deutsches Museum in Munich to the elephants in Thailand. . .

(This page is intentionally left blank, but by saying so it no longer is blank. . .)

TABLE OF CONTENTS

Acknowledgments	5
Chapter 1. Table of Contents	7
List Of Figures	11
List Of Tables	15
Chapter 2. Introduction	17
1.1 Motivation	17
1.2 Contributions	19
1.3 Thesis Scope and Organization	20
Chapter 3. Design of Exact Constraint Interfaces	21
2.1 Introduction	21
2.1.1 Exact Constraint Design	21
2.1.2 Terminology	22
2.2 Coupling Interface Types	24
2.2.1 Pin Joints	24
2.2.2 Elastic Averaging	26
2.2.3 Quasi-Kinematic Couplings	26
2.2.4 Planar or Directional Kinematic Coupling	27
2.2.5 Kinematic Couplings	28
2.3 Design of Standard Kinematic Couplings	28
2.3.1 General Coupling Design Process	28
2.3.2 Specific Design Considerations	29
2.4 Three Pin Coupling	36
2.4.1 General Coupling Description	36
2.4.2 General Coupling Design Process	37
2.4.3 Specific Design Considerations	38
Chapter 4. A Model for Elastic Averaging	41
3.1 The Principle of Elastic Averaging	41
3.1.1 Background	41
3.1.2 Examples of Elastic Averaging	41

3.2	Modeling and Analysis of Elastic Averaging	47
3.2.1	Background	47
3.2.2	Overview of an Elastic Averaging Modeling Process	48
3.2.3	Detailed Description of Process Steps	49
3.3	Simple Example - One Dimensional Rigid Beam	58
3.3.1	Example Description and Application of Model	58
3.3.2	Results from Simple Model	59
Chapter 5.	Design Case Study: Fiber Optic Connector	63
4.1	Problem Description	63
4.2	Background	64
4.2.1	Basic Optics for Fiber Optics	64
4.2.2	Fiber Types	65
4.2.3	Connecting Fibers	67
4.3	New Connector Design	71
4.4	Large Scale Connector Simulations	73
4.4.1	Elastic Averaging Model Application	75
4.5	Experiments	85
Chapter 6.	Precision Injection Molding of Fidelity Parts	89
5.1	Introduction to Precision Molding	89
5.2	Review of Existing Technologies	91
5.3	The Silicon Insert Molded Plastics (SIMP) Process	93
5.4	Research to Date	95
5.4.1	Edge and Surface Capabilities	95
5.4.2	Mask to Wafer Alignment	96
5.4.3	Backside Protection	97
5.5	Preliminary Mold Trials	98
Chapter 7.	Conclusion	101
6.1	Contributions of this Thesis	101
6.2	Future Work	102
6.2.1	Further Development of SIMP and Actual Scale Model Connector Tests	102
6.2.2	Extension of Symmetric Elastically Averaged Design	104
6.2.3	Metric for Determinism of Elastic Averaging	104

Chapter 8. References	107
Appendix A. Sensitivity Analysis Plots and Example FEA Figures	111
6.3 Sensitivity Plots	111
6.4 FEA Figures	124
Appendix B. Mathematics for Simple Elastic Averaging Model	129
Appendix C. Analysis for an Elastically Averaged Connector	141
Appendix D. Mathematics for Preload Beam	153

LIST OF FIGURES

Figure 1.1	Illustration demonstrating 6 Degrees of Freedom to be constrained between two surfaces	18
Figure 2.1	Illustration of terminology [4]	22
Figure 2.2	Example of a pin joint using the MT Ferrule	25
Figure 2.3	Physical Components of a Generic QKC [2]	27
Figure 2.4	Three Ball - Three Groove Coupling	29
Figure 2.5	Standard Coupling Geometry [4]	29
Figure 2.6	Coupling Geometry Stability	30
Figure 2.7	Instant Centers and Stability	31
Figure 2.8	Canoe Ball and Groove Element	34
Figure 2.9	Nomenclature for Three Pin Coupling	37
Figure 2.10	Three Pin Structure on Robot Interface	37
Figure 2.11	Kinematic Sheet Drawing	39
Figure 2.12	Spring Pin Schematic	39
Figure 3.1	Open and closed photographs of elastically averaged tooth couplings (figure by W. R. Moore [14])	43
Figure 3.3	Compliant wiffle tree structure created by Slocum for a semiconductor tester 44	
Figure 3.2	Schematic of a typical turret indexing and locking mechanism in engaged and disengaged positions using a curvic coupling (Courtesy of Hardinge Brothers, Inc. from Slocum [4])	44
Figure 3.4	Lego brick setup for evaluation of repeatability using elastic averaging principle with plastic parts	45
Figure 3.5	Convex pyramids on cantilever tips on wafer 1	46
Figure 3.6	Array of mating concave structures on wafer 2	46
Figure 3.7	Testing of passively mechanically aligned wafers	46
Figure 3.8	Example of elastically averaged torsional coupling [19]	47
Figure 3.9	Sample equivalent spring model for the torsional coupling	50
Figure 3.10	Example of elastic averaging including force cross coupling	53

Figure 3.11	Example of elastic averaging including force and displacement coupling	54
Figure 3.12	Equilibrium for a simple 2D case where d is the simulated tolerance of each contact point and x is the corresponding deflection of the part.	57
Figure 3.13	Schematic of simple one dimensional rigid beam model	58
Figure 3.14	Plot of standard deviation versus number of contact points for various cross coupling cases	60
Figure 3.15	Plot of displacement cross coupling factor based on percentage of cross coupling	61
Figure 3.16	Plot of standard deviation of angle versus number of contact points for various cross coupling cases	62
Figure 4.1	Schematic of total internal reflection in optical fiber - dashed lines show reflected rays while solid lines show refracted or lost rays.	64
Figure 4.2	Schematic of a single mode fiber	66
Figure 4.3	Schematic of rays in a step-index multimode fiber	67
Figure 4.4	Schematic of rays in a graded-index multimode fiber	67
Figure 4.5	Schematic showing components in a typical fiber connector	69
Figure 4.6	The MT Connector Ferrule	71
Figure 4.7	Trapezoidal half showing grooves (top) and Joined hexagon element with 21 cylinders laid in V-grooves (bottom)	72
Figure 4.8	Two connector elements shown mated inside sleeve - end view (left) and isometric view with cutout showing preload beam (right)	73
Figure 4.9	Bench-level experimental setup including a waterjet aluminum sleeve and a Delrin ferrule	74
Figure 4.10	Angle vs. Trial and Position vs. Trial result for large-scale model of assembly	75
Figure 4.11	Equivalent spring model of ferrule-sleeve interface	76
Figure 4.12	Quarter FEA Model for Sensitivity Analysis (Left) and Critical Parameter Schematic (right)	76
Figure 4.13	Stiffness Sensitivity (left) and Stiffness (right) Plots for Critical Parameters. Horizontal axis is the value for the dimension listed in the legend.	78
Figure 4.14	Error calculation locations for power loss	83
Figure 4.15	Capacitance Probe Measurement System - Sleeve mounted on Ferrule.	86
Figure 5.1	SEM of KOH etched features in Silicon (500 nm scale)	90
Figure 5.2	Basic schematic of silicon mold for blade edge	95

Figure 5.3	SEM photographs of conventionally ground steel razor blade tip (left - scale bar of 1 μm) and KOH etched Silicon edge (right - scale bar of 300 nm)	96
Figure 5.4	SEM photographs of conventionally ground steel razor blade surface (left - scale bar of 3 μm) and KOH etched Silicon surface (right - scale bar of 1 μm)	96
Figure 5.5	KOH Etching errors on $\langle 100 \rangle$ Silicon wafer due to mask misalignment - Edge mismatch (left) and surface terraces (right)	97
Figure 5.6	CAD Models of Wafer Masks for Fiber Optic Connector	98
Figure 5.7	Final Silicon Mold Inserts for Fiber Optic Connector	99
Figure 5.8	Silicon mold inserts installed in aluminum mold - Groove insert (left) and Top trapezoidal shape insert (right)	100
Figure 5.9	Full scale connector shown next to a 12-fiber ribbon cable.	100
Figure 5.10	Photographs of injection molded ferrules - Plastic grooves (left) and grooves with optical fibers installed (right)	100
Figure A.1	FEA Mesh used for determining stiffness sensitivity	125
Figure A.2	Example displacement results from FEA mesh for quarter model of sleeve	125
Figure A.3	FEA Mesh used for determining nominal stiffness behavior of sleeve using displacement boundary conditions	126
Figure A.4	Example displacement results from FEA mesh for full model of sleeve using displacement boundary conditions	126
Figure A.5	FEA Mesh used for determining coupled stiffness behavior of sleeve using gap elements	127
Figure A.6	Example displacement results from FEA mesh for full model of sleeve using gap elements and displacement at one contact point	127
Figure B.1	Schematic of simple one dimensional rigid beam model	129
Figure C.1	Ferrule Dimensions	141
Figure C.2	Sleeve Dimensions	141

LIST OF TABLES

TABLE 1.1	Summary of Various Relative Coupling Performance Criteria	19
TABLE 3.1	Summary of Results Statistics	60
TABLE 4.1	Common Fiber Core and Cladding Size	67
TABLE 4.2	Common Forms of Commercial Connectors (SM is single mode and MM is multimode)	71
TABLE 4.3	Standard Deviation from Simulations and Elastic Averaging Trend for 5X and 1X Models (All tolerances and results in mm)	83

Chapter 1

INTRODUCTION

1.1 Motivation

In precision machine design, one of the most important steps in designing a machine is the consideration of the effect of interfaces between components. A badly designed interface can vary from costly difficulties such as additional control or calibration to machine failure when degrees of freedom are improperly constrained. In order to avoid these problems, engineers have developed a series of tools known collectively as *exact constraint design* that allow for interface features to be designed to maximize performance. Within any constraint device, the position and orientation of one part with respect to another can be defined by six degrees of freedom - three translations and three rotations as shown in Figure 1.1. In exact constraint, a single contact point is used to exactly constrain one of these degrees of freedom by providing resistance to motion in each degree of freedom. A coupling in which all six degrees of freedom are constrained by exactly six contact points is often called a deterministic or kinematic coupling. The drawback of using contact points is that Hertzian contact stresses increase at the contacts, limiting load capacity and system stiffness. The boundaries of kinematic coupling applicability has been expanded in recent years to high load, industrial areas with the introduction of high load couplings using “canoe ball” couplings developed by Slocum [1] and quasi-kinematic couplings developed by Culpepper [2]. These and other coupling flavors expand beyond single points of contact to allow for contact patches and line contacts, respectively.

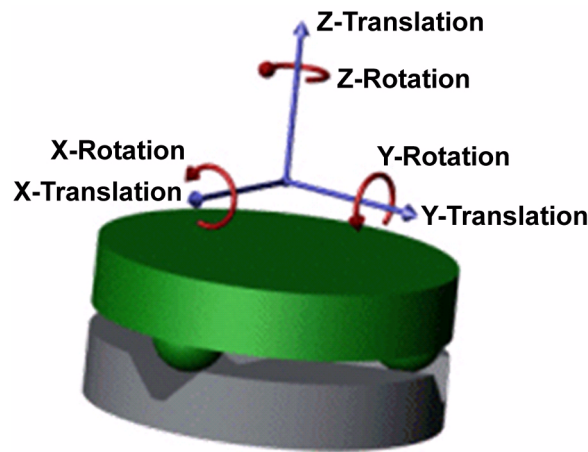


Figure 1.1 Illustration demonstrating 6 Degrees of Freedom to be constrained between two surfaces

Elastic averaging can be considered separately from pure kinematic couplings or quasi-kinematic couplings, as it represents a subset of surface coupling types where improved accuracy is derived from the averaging of errors over a large number of contacting surfaces. Contrary to kinematic design, elastic averaging is based on significantly over-constraining the solid bodies with a large number of relatively compliant members. As the system is preloaded, the elastic properties of the material allow for the size and position error of each individual contact feature to be averaged out over the sum of contact features throughout the solid body. Although the repeatability and accuracy obtained through elastic averaging may not be as high as in deterministic systems, elastic averaging design allows for higher stiffness and lower local stress when compared to kinematic couplings. In a well designed and preloaded elastically averaged coupling, the repeatability is approximately inversely proportional to the square root of the number of contact points.

Combining these options into a design menu allows designers to select the proper coupling for a specific situation. Table 1.1 summarizes the major coupling types and their relative abilities. The following chapter will give a short description of each coupling type, with a detailed description of elastic averaging in the following chapters.

TABLE 1.1 Summary of Various Relative Coupling Performance Criteria

Coupling Type	Contact Type	Repeatability	Stiffness	Load Capacity	Robustness
Basic Pin Joint	Surface	Poor	High	High	Poor
Elastic Averaging	Mixed	Good	High	High	Fair
Planar Kinematic	Mixed	Good	High	High	Good
Quasi-Kinematic	Line	Good	Medium to High	High	Good
Kinematic	Point	Excellent	Low	Varies	Good

Elastic averaging will be applied to a case study on fiber optic connectors. Traditionally, fiber optic connectors rely on extremely precise, costly manufacturing to obtain repeatable connections. The most common multi-fiber design, the MT ferrule, relies on fitting two precisely ground pins into two holes on each side of the connector. Without tight tolerances, the connector design can range from being unable to deterministically locate the connector to causing part damage during assembly. With precise tolerances on the order of 0.1 - 1.0 μm , the connector design can minimize power loss at the interface, but only at a significantly increased cost. Elastic averaging can be employed in a multifiber connector to improve the repeatability of the interface without requiring costly tolerances. To further improve the performance of the connector, a new method for creating precision injection molding tools is proposed. This process, the *Silicon Insert Molded Plastics* process (SIMP), replaces precision mold surfaces created using traditional machining process with silicon inserts which are microfabricated in batch quantities with tolerances on the order of microns.

1.2 Contributions

One of the primary contributions of this thesis is a method for modelling elastic averaging, including a process for modelling and analyzing coupling geometry and some design rules for employing elastic averaging. Out of the research, a qualitative metric for determining

the level of constraint in a coupling was recognized. This metric is another contribution that will assist designers in determining if an elastically average coupling is truly elastic averaging and can be analyzed quasi-deterministically, or if the coupling is over-constrained, leading to lack of repeatability and increased wear and surface damage. The final contribution is the co-development of the SIMP concept with the specific goal of producing a fidelity connector part.

1.3 Thesis Scope and Organization

When investigating the design of precision interfaces such as a fiber optic connector, a number of different disturbances can be considered. Disturbances usually include manufacturing errors, material variation, environmental factors, and external disturbances. In the scope of this thesis, the manufacturing error is considered to have the most significant effect and is the primary focus of modelling in the following chapters. In many cases, environmental factors such as contamination, unpredictable thermal loads, and surface damage have an equally large effect of overall system performance. However, except in cases where these factors can be easily quantified, environmental effects cannot be easily simulated and must be measured.

Thesis Organization

The second chapter in this thesis will present a basic introduction to precision assembly interfaces, including the kinematic coupling design process and an example of a planar kinematic coupling. In the third chapter, a detailed description of elastic averaging will be presented, including a model for analyzing elastically averaged couplings and a simple test example. Chapter four presents an application of the elastic averaging model to a case study on a fiber optic connector, while chapter five outlines the manufacturing process intended to produce the connector parts. The final chapter presents some conclusions and suggestions for future work.

Chapter 2

DESIGN OF EXACT CONSTRAINT INTERFACES

2.1 Introduction

This chapter gives a brief introduction into the different methods of constraining two precision interfaces. Further background is given on the most repeatable interface, the kinematic coupling, and an example of a planar kinematic coupling.

2.1.1 Exact Constraint Design

Exactly constrained assemblies are discussed extensively by Blanding [5] and Slocum [4]. In an exactly constrained device, each degree of freedom in a body is individually considered and constrained as required by the design. A properly constrained device will use only the minimum number of constraints required to restrict motion in specified directions, while all other degrees of freedom are free. In analysis, an exactly constrained assembly can be defined exactly using vector loops for displacement and force where there is the same number of equations and unknowns. These equations can be used to determine the exact location of the parts for any manufacturing deviations of the component features. Therefore, accuracy of exactly constrained assemblies can be directly correlated to the manufacturing process and corrected easily. Repeatability is often directly related to the assembly process from factors such as friction, environmental contamination, and thermal errors.

When a device is over-constrained, multiple constraints compete to locate the device in a specific direction. For ideal parts in CAD software, the over-constraint usually can not be detected and does not cause a problem. However, when real parts with tolerances are involved, the over-constraint can cause the parts to deflect, bind, or deform during assembly. These effects can be acceptable in many cases, although unintended internal stresses or gaps in the assembly can cause issues during subsequent assembly steps or failure during use. On the other hand, exactly constrained devices will assemble with a wide range of tolerances, will not bind, and are easier to assemble. Exact constrained devices can often tolerate minor errors such as wear at the contact locations, although high contact stresses tend to limit load capacity and stiffness.

2.1.2 Terminology

It is important at this point to define some terms related to precision interfaces - accuracy, repeatability, and interchangeability. When a series of data points is simulated or mea-

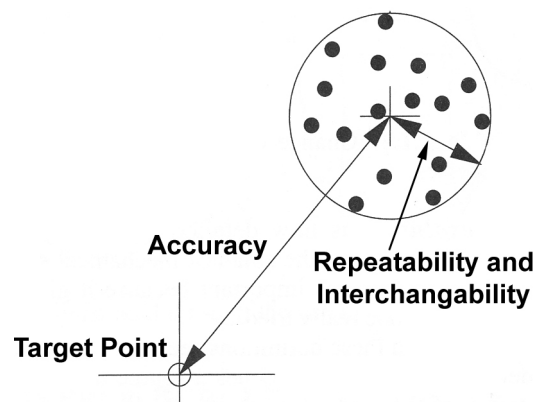


Figure 2.1 Illustration of terminology [4]

sured, a distribution of points will result. This distribution of points can usually be described as a mean and a standard deviation about that mean. In this case, accuracy can be defined as the difference between the mean and the intended target point. Most coupling inaccuracies can be directly related to a systematic error which has the same value

and sign for any measurement. Systematic errors in couplings tend to develop due to an error during machining which is common to every part produced, but they can also develop due to predictable thermal changes in the environment or deflections within the part due to loading.

Repeatability and interchangeability are difficult to distinguish in results such as those shown in Figure 2.1, although their combined effect can be captured in the standard deviation. Usually the quoted repeatability number is given as plus and minus three times the standard deviation to reflect the statistical significance that one part in a million will be outside of the distribution, although this definition of repeatability varies throughout the literature. To simplify the terminology, repeatability and interchangeability will be referred to only using the standard deviation, unless otherwise noted. Repeatability is defined as the variation around the mean due to random errors during assembly, such as unpredictable thermal changes, component damage, friction, and environmental contaminants. These factors are often very difficult to analyze or predict during the design stage, and they can only really be estimated through experimentation. In addition, these random errors are often the “real-world” or industrial effect that increases the overall error when a concept is transferred from the ideal laboratory conditions to an industrial setting.

Interchangeability is defined as the variation around the mean due to random manufacturing errors within the specified tolerances. Since the tolerances are specified statistically, interchangeability can be predicted somewhat deterministically for a large number of parts knowing that any given part must lie within a certain distribution of errors. This assumption allows the Monte Carlo process to be used to predict interchangeability of an interface. In a Monte Carlo analysis, a randomly selected set of dimensions selected from a statistical distribution of tolerances is provided to a model of the system to predict some system performance metric. Numerous sets of data can be generated and passed through the simulation to generate a distribution of the output variables. These output variables can then be analyzed to determine the interchangeability and accuracy of a given tolerance set. If the effect of the random errors used in calculating repeatability are on the same order as

the tolerances used to estimate interchangeability, the interchangeability and repeatability values converge, allowing for both values to be simulated. However, this statement is not true for all cases. Often, many systems are designed so that interchangeability is extremely low, but environmental conditions and friction can cause repeatability to be an order of magnitude worse.

2.2 Coupling Interface Types

When designing a coupling, the precision engineer can most easily distinguish the different coupling types by investigating the types of contact that occur between the coupled interfaces. The basic types of contact are surface, line, and point contact, generally in order of increasing repeatability.

2.2.1 Pin Joints

The simplest coupling design consists of surface contact, which generally occurs with direct contact between large, relatively flat interface features. Because surface contact couplings have many possible contacts spread over the interface, deterministic design becomes difficult and repeatability depends mostly on flatness, finish, and other tolerances. Generally, direct interface contact can constrain only three degrees of freedom, which requires the incorporation of additional alignment features into the design for complete constraint of the six degrees of freedom. The most common alignment geometry are pins, due to low cost and easy implementation for non-precise applications; however, strict tolerances or compliant geometries are required to achieve a reasonable repeatability. Without compliance, pin joints can easily destroy parts when the alignment features jam or deform. Compliant geometries, such as dovetails, grooves, and rails, improve repeatability of an interface by enforcing geometric congruence through predictable elastic deflections and the removal of irregular surface features through wear-in.

In cases where the interface uses a large number of pins, the coupling can begin to function like an elastically averaged joint. However, multi-pin joints are less deterministic than

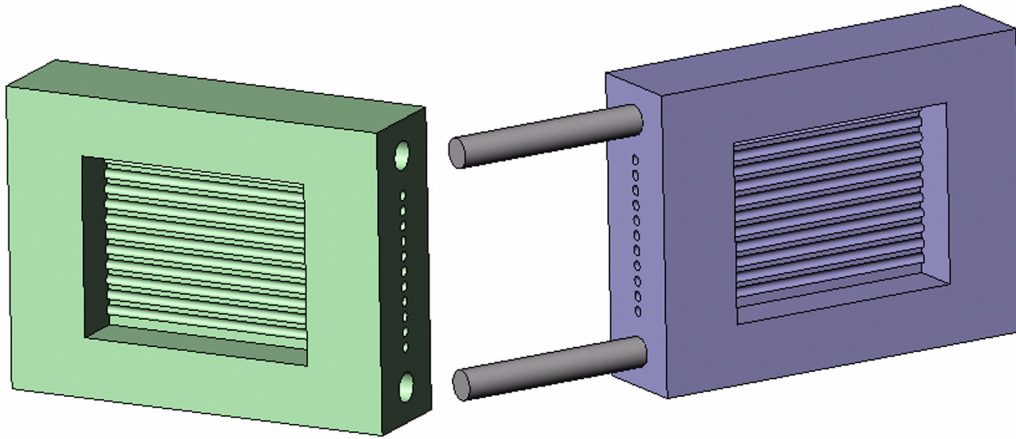


Figure 2.2 Example of a pin joint using the MT Ferrule

elastic averaging as they do not guarantee contact between contacting elements and can often overconstrain the interface. If tolerances are large in a pin joint, configurations may become possible where only a small subset of pins contacts their receptacles. The other pins “float” within the hole and do not provide any alignment function. These pins are effectively extra features which can be removed from the structure. If tolerances in the joint are small, configurations may become possible where multiple pins may initially come into contact. As the interfaced is closed, these pins must deflect to absorb any other manufacturing variances. Pins without compliance will deflect initially, but the pin or its matching hole may deform when the interface is completely closed. Repeatability of the interface will improve as the interface wears in, but interchangeability of the interface will degrade as the effective hole dimensions change.

In many industrial applications, preload to secure the joint is applied using bolts normal to the interface surfaces. Because of the frictional contact of the surfaces and the bolting load, surface contact couplings provide maximum stiffness and load capacity, which makes them suitable for most industrial applications where precision is not the crucial functional requirement.

2.2.2 Elastic Averaging

Elastic averaging represents a subset of surface coupling types where improved accuracy is derived from the averaging of errors over a large number of contacting surfaces. Repeatability and accuracy obtained through elastic averaging are generally not as high as in deterministic systems, although elastic averaged designs allow for higher stiffness and lower local stress. In a well designed and preloaded elastic averaging coupling, the repeatability is approximately inversely proportional to the square root of the number of contact points. Elastically averaged couplings are often non-repeatable due to environmental contamination, as contaminants can significantly change how the surfaces interact. In addition, many designers are hesitant at using elastic averaging due to the stresses that form in the assembly when its members are elastically deflected. Likewise, high assembly forces can develop in elastically averaged systems, which can cause damage and wear to the members. Further details on elastic averaging are available in Chapter 3.

2.2.3 Quasi-Kinematic Couplings

The next level of surface contact is the quasi-kinematic coupling, which consists of line contact situations such as a cylinder on a flat or a ball in a cone. By reducing a surface contact to a line, over constraint is reduced to only two degrees of freedom. Since line contacts only weakly overconstrained an interface, more deterministic relationships can be formed to provide improved repeatability. In industrial settings, line contacts do not appear as often as surface contacts, but the optics industry has made use of line contacts for aligning lenses in cylindrical capsules in v-grooves. Recent work by Culpepper [2] [3] has developed a framework for designing and implementing quasi-kinematic couplings for high load, industrial environments, specifically in the assembly of an automobile engine. This framework includes a constraint metric that allows the designer to assess and minimize the degree of overconstraint present in the design based on an analysis of fully constrained and weakly constrained directions.

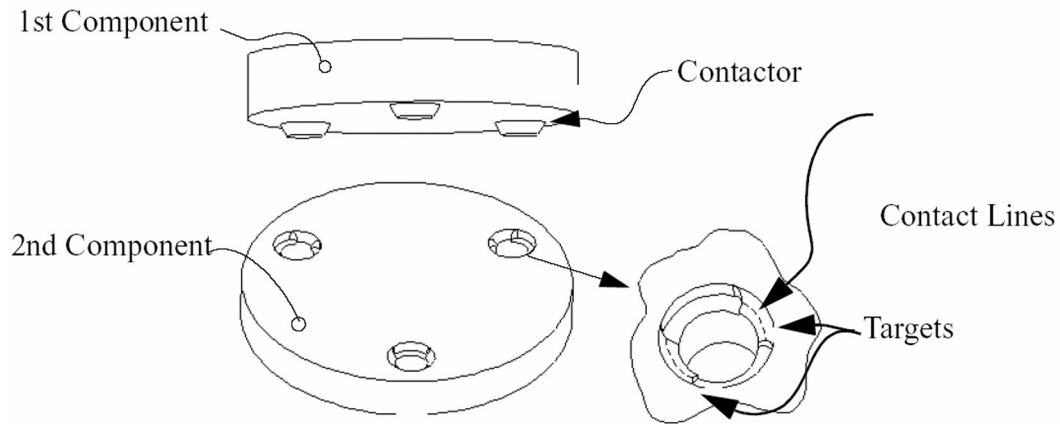


Figure 2.3 Physical Components of a Generic QKC [2]

Since quasi-kinematic couplings reduce the amount of surface interaction area, less useful area is available for the distribution of stress. Therefore, quasi-kinematic couplings can no longer support the highest loads with the best stiffness, but can provide improved precision with reasonable stiffness. Culpepper's design combines quasi-kinematic couplings using revolved line contacts with predetermined and predictable plastic and elastic deflections to optimize load capacity and stiffness, without sacrificing repeatability.

2.2.4 Planar or Directional Kinematic Coupling

The next coupling type, the planar or directional kinematic coupling, can be a combination of all three types of contact. For example, a planar coupling consists of a large surface contact area at the interface along with specially designed line or point contacts to constrain the free degrees of freedom. A directional coupling could be any type of coupling which has precision alignment features designed to repeatably constrain specific directions, while relying on surface features, tolerances, etc. in noncritical directions. The mixed contact coupling type has been formulated in the author's M.S. thesis [9] and is discussed in this thesis as the three pin kinematic coupling, which uses a large surface area and three line contacts on three pins. Preload is applied by lightly torquing a bolt normal to one of the pins and more heavily torquing securing bolts normal to the interface. More details will be given for the three pin coupling later in this document.

Due to the mixed nature of these couplings, repeatability, load capacity, and stiffness are all a function of the individual design. Overall, planar kinematic couplings can provide high stiffness and load capacity with moderate repeatability.

2.2.5 Kinematic Couplings

The final coupling type, a fully kinematic coupling, represents the gold standard of couplings by using individual point contacts that each constrain a single degree of freedom. Because the interaction between the interface surfaces can be described by six distinct points, closed loop mathematics can be formulated to deterministically describe the relationship between the surfaces. In reality, point contacts must typically tolerate high loads, therefore the theoretical point contacts deform into Hertzian contact ellipses under large applied loads. The main limit to the repeatability of a kinematic coupling is the surface finish of the contact regions, while load capacity and stiffness are limited by the Hertzian contact stress.

By far, the most common form of the standard kinematic coupling is the ball-groove coupling, which interfaces three balls on one component to three grooves on the opposing component. The balls and grooves are placed on the three points of a planar equilateral triangle with the triangle sides coincident to lines passing through the contact points. The typical coupling structure is shown in Figure 2.5, while the standard coupling geometry terminology is shown in Figure 2.6.

2.3 Design of Standard Kinematic Couplings

2.3.1 General Coupling Design Process

As mentioned above, the pure kinematic coupling can provide the most precise alignment interface. Much work has been published on the general design process of standard kinematic couplings. For a more detailed description of the design process, one should refer to the work of Slocum [4]. Many years of work by Slocum and his students have produced a fairly standardized mathematical procedure for designing kinematic couplings. Originally

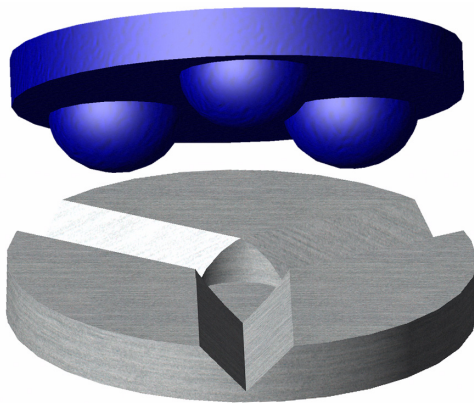


Figure 2.4 Three Ball - Three Groove Coupling

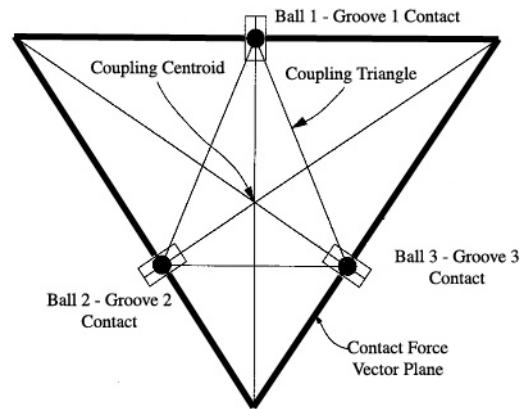


Figure 2.5 Standard Coupling Geometry [4]

formatted in a convenient Excel spreadsheet, the mathematics necessary to design a coupling have been transferred to MATLAB and MathCAD. Each component is defined by a location on the main coupling circle, as well as a vector describing the normal of the interface surface at the theoretical contact point. In addition, the preload and disturbance forces must be specified so that the Hertzian contact stress and deformations at the ideal point contacts can be determined. Two quick checks for design success are to verify that the Hertzian stress stays less than the allowable contact stress and that the contact forces should not reverse direction. The position and force vectors are then assembled into matrices and combined with the Hertzian deformation to solve for the error motions of the coupling under the disturbance loading. Throughout the design, several other critical parameters like coupling stiffness, reaction forces at the points, and contact ellipse dimensions can be calculated.

2.3.2 Specific Design Considerations

While many of these design considerations are discussed in relationship to the purely kinematic coupling form, the general concepts apply equally well to any coupling form.

Geometric Stability

In addition to the basic mechanics of the design, there are additional design considerations that must be addressed for a coupling to work. The first consideration, geometric stability,

can be generally defined that a stable coupling is a coupling that will remain properly constrained under design loads. Stability requires specific attention for designs that stray from the ideal geometry of 120 degree spaced groove to groove angle. Figure 2.6 shows a 2D representation of different groove orientations and a relative statement of the coupling stability. One of the most useful tools to analyze stability is the well known kinematics con-

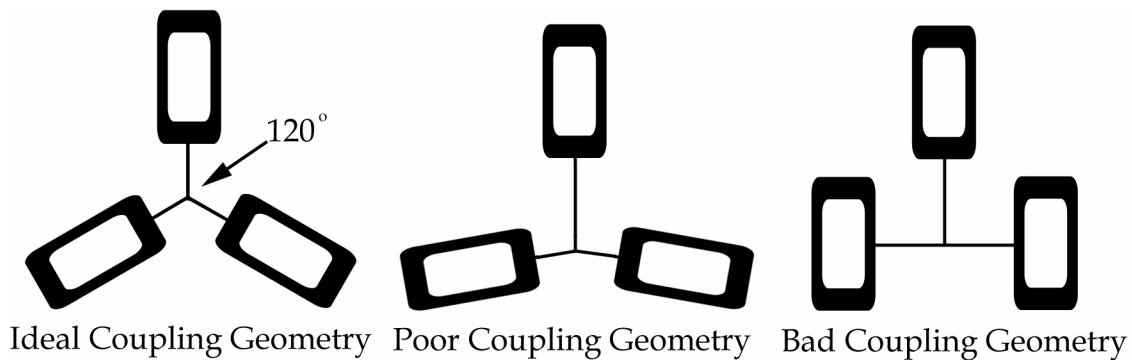


Figure 2.6 Coupling Geometry Stability

cept of instant centers, which is well described by Blanding in terms of proper constraint [5]. By determining the instant centers of two elements of a coupling, the third element can be located to provide maximum stiffness. The most stable coupling is one where each of the three instant centers is the same distance from the coupling centroid with the configuration as shown in the first schematic of Figure 2.6. This equal placement of constraints creates equal resistance to rotation at each instant center. If the coupling angles are changed as in the second schematic, the instant center of one element moves further from the coupling center than the other two instant centers. Increased distance between the instant center and the constraint introduces a longer moment arm about the coupling centroid for the constraint forces at the distant coupling element. The constraining moments about the other instant centers decrease, causing a non-symmetric stiffness in the coupling. If the angles keep increasing, stiffness in one direction can become negligible, causing instability to any disturbance force in that direction.

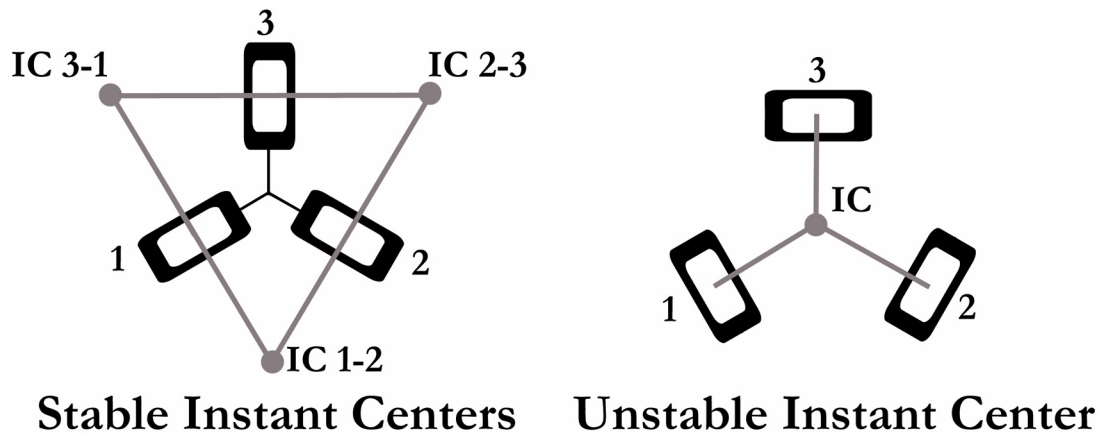


Figure 2.7 Instant Centers and Stability

In Figure 2.7, two sample instant center schematics are shown. The first schematic indicates the 120° configuration above where the instant centers are located at a distance from each other to create maximize stability. The second schematic shows a configuration that could easily be mistaken to have stability as all six points are in contact in 120° form. However, an analysis of the instant centers shows that all three instant centers coincide at the center of the coupling triangle. Any disturbance force applied to this coupling will cause rotation about the instant center with very little resistance, as no constraint forces can be applied normal to the moment arm created from the constraint to instant center. For a design similar to the third schematic in Figure 2.6, the instant centers can occur at infinity, which allows for translation in the direction normal to the lines connecting the constraint and instant center. These two designs are inherently unstable, unless sufficient friction can be introduced at the interface to resist motion along the groove. While these couplings may represent bad designs for exact constraint of interfaces, differential stiffness and frictional constraints can be cautiously included in designs where these features may be desirable.

In addition to static stability, dynamic stability must also be considered in designs where high loads are applied in directions that change over time. In the first diagram, maximum dynamic stability occurs when the planes containing the contact force vectors intersect to

form an equilateral triangle using similar logic as above. This configuration provides maximum resistance to a disturbance in any direction by properly providing a supporting surface. It can be easily seen in the second and third diagrams how a disturbance can easily cause motion in the coupling. When the design introduces dynamic loading or moving geometry, the coupling must also be checked for dynamic stability. Dynamic instability can be initiated when the forces at the interface contact points suddenly reverse or when the contact force vectors become aligned with the direction of the grooves. To prevent these dynamic instabilities, additional preload can be applied (within the allowable contact stress) and physical stops can be used to prevent improper motion.

Interface Stiffness

Integrally related to the stability of the coupling, stiffness can become a major influence on the applicability of a standard kinematic coupling to an industrial design. When the coupling components are arranged in the 120 degree configuration and the groove faces are perpendicular, the coupling provides equal stiffness in all directions. Change in the geometric parameters of any of the components will introduce changes in stiffness that must be considered if they are in sensitive directions. Since these couplings rely on six point contacts to support interface loads, stress and deformation levels can rapidly increase, causing a very undesirable change in stiffness properties when compared to a bolted joint. Changes in stiffness when using three ball - three groove couplings can amount to an order of magnitude or more reduction in stiffness. Careful comparison of finite element simulations of the original joint with approximations of the ball - groove interface are instructive for order of magnitude comparisons of the stiffness change. Since Hertzian effects at point contacts are not currently well modeled in commercially available FEA products, several approximations can be used to model the interface contact. The most accurate approximation relies on creating flexural geometries that simulate the joint stiffness predicted by traditional contact mechanics. However, careful attention must be paid to this approximation to ensure that all deflections and forces are compared at the proper locations. A less accurate method to simulate the contact is to replace the coupling

geometry with a block enclosing the coupling elements. To simulate the change in stiffness of the joint, the material properties of the new block should be altered from the basic material of the structure to reflect the reduced stiffness of the coupling determined by contact theory [9].

Contact Stress

Another item to be considered is the contact stress present at the interface. Due to the nature of the point contact, high Hertzian contact stresses can be present in the coupling under the preload alone. Stress analysis should be performed both concerning the static preload alone and with the maximum predicted disturbance force. In addition to the good practice of designing with an appropriate factor of safety, a ball-groove interface should be designed so that space of at least one diameter of the contact patch is left between the border of the Hertzian contact patch and the edge of the supporting components.

To counter the low load limitation present in traditional ball-groove couplings, Slocum has developed the specialized “canoe ball” element as described in U.S. patent number 5,711,647 (although not claimed). The canoe ball replaces the traditional hemispherical contacting element with a trapezoidal block with sections of a spherical surface ground onto the contacting surfaces. By grinding spheres with diameters as large as a meter onto the sides of the canoe ball, contact stress at the interface can be reduced while preserving the contacting components small size. The larger diameter creates an approximately kinematic elliptical contact patch that drastically increases the load capacity of a coupling while maintaining high repeatability. In Figure 2.8, the canoe ball is shown along with its matching groove. Benchtop level experiments have shown repeatability of approximately one micron for an experimental setup [9] and 0.1 microns in previous work by Mullenheld. For a good presentation of contact mechanics theory, Johnson provides detailed derivations [6].

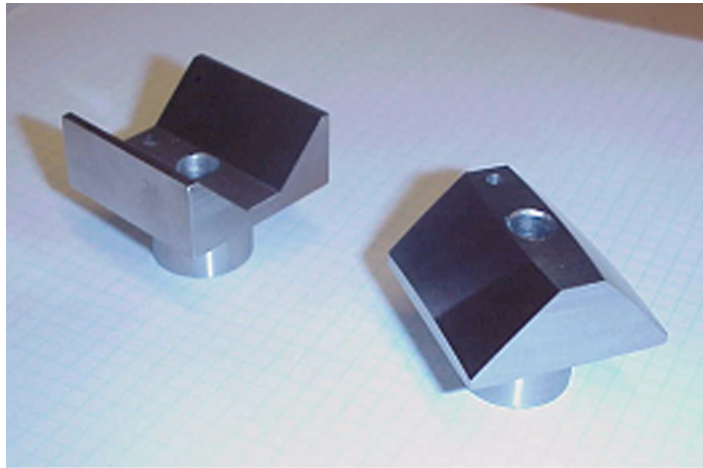


Figure 2.8 Canoe Ball and Groove Element

Surface Material Properties

Of the many factors which affect the repeatability of a coupling, the choice of material for the ball and grooves has several critical influences. As in any precision design, one of the most important factors to consider is the friction between the contacting surfaces. Friction alters repeatability the most during initial assembly of the coupling. After each of the coupling elements touch, friction between the surfaces builds up and creates forces that impede the motion of the entire coupling from settling into its lowest energy state. Each subsequent replacement of the coupling will settle into a different position based on a complex relationship between the initial position of each contact point and the exact direction of applied force. Several techniques can be used to minimize the effect of friction, including proper vibration dithering of the interface or implementation of low coefficient of friction materials such as Titanium Nitride combined with Tungsten Disulfide. During installation, frictional effects can be easily minimized using a stepped bolting procedure and by simply tapping the interface region with a hammer.

Another important material influence on the repeatability stems from the relative hardnesses of the ball to the groove. Ideally, the best repeatability can be obtained by the combination of a hardened steel ball and groove. However, some designs may stipulate that

one half of the coupling be disposable, while the opposing half must remain fixed to the rest of the structure. In these instances, it may be more useful to use hardened steel ball elements on the fixed structure and polymer or aluminium groove elements on the disposable components. This technique will help to prevent any assembly damage from being imparted on the fixed, more expensive structure and transfer the deformations to the grooves on the disposable structure. In addition, grooves can be easily milled into mild steel components using standard end mills rotated 45 degrees, while the hardened ball elements can be expensively machined or press fit into the fixed structure. When the ultimate level of precision is required, ceramics such as Silicon Nitride can be used for extreme hardness, as well as improved repeatability through decreased friction and wear-in time. During the initial assembly cycles of a single matched coupling, wear-in has been observed when coupling repeatability decreases slightly to a steady state value after many replacement cycles. This effect can occur due to the removal of surface finish aberrations by the loading and high contact stress at the point contact, as well as other interface interactions.

The final material effects involve three variations on surface geometry: surface finish, debris, and fretting. Out of the three variations, surface finish is the easiest parameter to affect during design, as the finish can be specified and measured during manufacturing. Furthermore, surfaces will tend to burnish or polish each other with increased time and load. Debris and fretting are more difficult parameters to analyze and remove, as these effects tend to develop over the lifetime of the components. In most cases, repeatability variation due to debris can be reduced by simply establishing a regular cleaning procedure to remove the debris using necessary solvents and by placing a small layer of grease on the elements. The final surface effect results from a process known as *fretting corrosion*. Fretting occurs between two surfaces of similar materials, particularly steels, when they are pressed together under large forces. On a small scale, these large forces cause surface asperities to crush together and atomically bond. When the surfaces are separated, the new bonds are ripped apart, causing the small pieces of the bonded materials to become debris on the surface. In addition, the process of ripping apart the material exposes new material

to the environment. The newly exposed material can oxidize, causing a change in surface hardness as well as surface finish. Variation due to fretting cannot be easily avoided under high loads if non-stainless steels are used, so it is recommended that stainless materials, ceramics, or combinations of dissimilar materials be used. Ceramic and stainless materials also have the added benefit of being noncorrosive in many unpleasant industrial environments.

Additional information on kinematic couplings can be found in the Master's Theses of Hart [8] and Willoughby [9], as well as previous work by Slocum (e.g. [1] or [4]).

2.4 Three Pin Coupling

2.4.1 General Coupling Description

The *three pin coupling* is categorized as a planar kinematic coupling, as contact occurs at three line or point constraints and a large surface contact. The name of this coupling is derived from the geometry of the interface, which consists of a plane contact constraining three degrees of freedom and three pins constraining motion in the plane. Each pin constrains motion by mating with a precision control surface normal to the interface plane. To prevent pins from jamming during assembly and to remove any free motion, preload is applied to an anvil pin using compliance or some adjustable mechanism. The proper design of the pin geometry and preload force will compel the coupling to deterministically seat in a repeatable position. The control surfaces and the pins are the only elements of the interface that require accurate tolerancing, as repeatability and exchangeability is affected by the location of each element. In Figure 2.9, the basic geometry and nomenclature for the three pin coupling is shown, while Figure 2.10 shows an example of one possible coupling structure suggested for use in a demountable interface on an industrial robot [9]. Since each pin interfaces with a flat or curvic surface, Hertzian contact theory can be used to describe the interface stress and deformation between the cylindrical pin or ground point contact and the control surface.

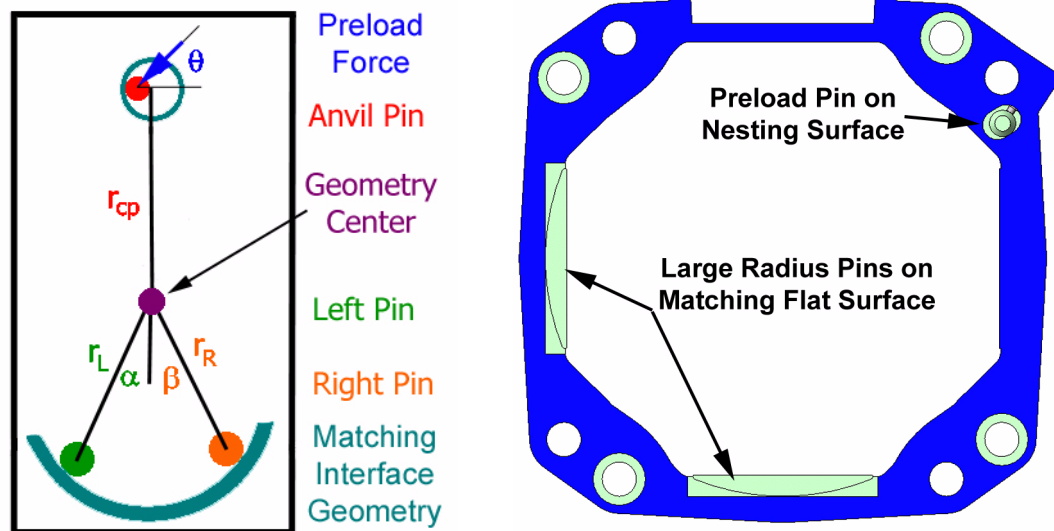


Figure 2.9 Nomenclature for Three Pin Coupling **Figure 2.10** Three Pin Structure on Robot Interface

2.4.2 General Coupling Design Process

The basic coupling design process is a rather simple process, as it involves fairly standard summations of forces with regard to preloads, disturbances, and friction. In order to implement a three pin coupling, the following steps are required:

1. Specify initial interface geometry, including locations for the support pins, anvil pin, control surfaces, and preload bolts. Determine method for applying preload and estimate static and disturbance loads. To reduce complexity of calculations, transfer external forces and moments to the location depicted as the geometry center in Figure 2.9.
2. Construct a free body diagram based on initial geometry and the static load. Perform summation of forces and moments on this geometry to sustain static loading case. Solve for the minimum required in-plane preload necessary to ensure contact of the three pins with the control surfaces and for the minimum bolting force necessary to keep the planar surfaces in contact. Throughout the calculations, it is important to include friction from static loading (but not the bolting force) to ensure that the in-plane preload is suffi-

cient to overcome the friction and seat the coupling with all possible initial positions of the coupling.

3. Construct another free body diagram based on the initial geometry and the disturbance loads. Perform summation of forces and moments on the geometry to sustain the dynamic loading case. Solve for the minimum required normal preload necessary to ensure contact of the three pins with the control surfaces and for the minimum bolting force necessary to keep the planar surfaces in contact. Throughout these calculations, it is important to include the effect of in-plane friction as a function of the normal loading, as the in-plane friction will help to resist moments and torques in the coupling plane. Therefore, the bolting force must be increased to increase frictional resistance to any dynamic disturbances.
4. Using contact forces at pins, check Hertz contact stresses, bending stresses, and any other failure modes of concern. Diameters and heights of the pins and the control surfaces can be determined based on these failure possibilities. Appropriate factors of safety should be applied to the in-plane preload, bolt forces, and stresses to ensure that the design will safely seat if estimated disturbance forces are exceeded.

2.4.3 Specific Design Considerations

Preload on Third Pin

Preload on the third pin can be applied in numerous ways, depending on the geometry and restrictions of the coupled components. In U.S. patent number 5,915,678, Slocum used a form of the three pin coupling called the *kinematic sheet* to align printed circuit boards for the electronics industry. Three pins were placed on a surface tilted with respect to vertical, while matching notches are placed in the kinematic sheet. Preload is applied to all three pins passively by using gravity to pull the sheet into place on the positioning plane. An illustration of this preload method excerpted from the patent is shown in Figure 2.11.

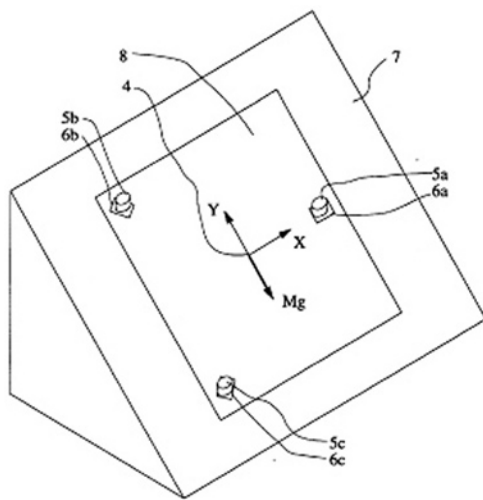


Figure 2.11 Kinematic Sheet Drawing

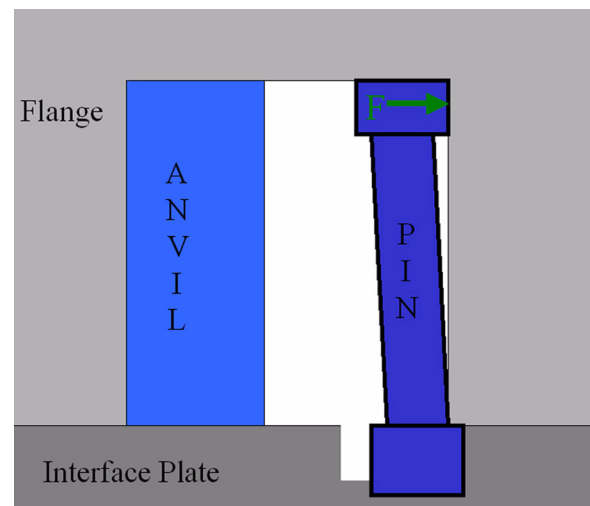


Figure 2.12 Spring Pin Schematic

In Figure 2.12, another preload method is shown using a combination of a thick, rigid anvil pin and a relatively thin and compliant spring pin. The spring pin preload method ideally operates by simultaneously inserting the anvil and spring pin into the matching hole on the opposing component. By designing the matching hole to be smaller than the maximum distance between the outer surfaces of the pins, the pins will be compressed together. Since the spring pin is more compliant than the anvil pin, the compression force will cause the spring pin to bend following standard beam theory. Ideally, the anvil pin should not deflect at all and remain in kinematic contact with the matching control surface. Preload force for this design can be specified by determining the spring pin deflection from the basic geometric parameters of matching hole diameter, spring pin head diameter, spring pin main diameter, and distance between the spring pin base and anvil base. This spring pin deflection can be passed through standard beam equations to determine the force created from the pin insertion.

The final preload method considered employs a simple preload bolt, aligned so that its force is applied in the necessary direction for coupling constraint. This preload method is the simplest to implement, as it requires only a threaded hole in the proper direction. However, careful attention should be paid to the free body diagram and force directions to

ensure that the coupling will seat in only one location. To ensure that overconstraint does not occur, a specialized bolt can be used with a copper tip to allow for some compliance at the contact point. Also, a simple wooden prototype can save much time verifying that the direction of the preload will properly seat the coupling.

Preload in Bolts

Preload applied using the bolts normal to the interface are very important to the successfulness of the three pin coupling under dynamic situations. To simplify calculations and improve precision, preload bolts should be located so that they pass through the centers of the pins. Often, the design will require that bolts be placed at separate locations or that more than three bolts will be needed to supply sufficient force. In this situations, the design must address bolt arrangement to prevent asymmetric bending of the interface plane. Bickford and Nassar have compiled a very useful handbook that can be helpful in properly designing the bolting configuration [7].

Friction on Interface

Friction on the large contact surface provides the three pin coupling with additional ability to sustain large forces and moments in the plane of the coupling. To create interface friction, large normal forces must be applied to the surface using bolts. If the required bolting force exceeds the capability of the desired or possible bolting pattern, the friction coefficient of the interface surfaces must be increased by changing the interface material using coatings, by changing the quality of surface finish, or by including a dimpled friction plate between the interface surfaces. Any changes in frictional properties must be reviewed in the second step of the generalized design process to ensure that the in-plane preload is sufficient to seat the coupling.

Additional information on the three pin coupling can be found in the Master's Theses of Hart [8] and Willoughby [9].

Chapter 3

A MODEL FOR ELASTIC AVERAGING

3.1 The Principle of Elastic Averaging

3.1.1 *Background*

The principle of elastic averaging states that the accuracy of an interface can be improved by averaging errors using controlled compliance between precision surfaces. The key to elastic averaging is to have a large number of features spread over a broad region that elastically deform when separate parts are forced into geometric compliance with each other. As the system is preloaded, the elastic properties of the material allow for the size and position error of each individual contact feature to be averaged out over the sum of contact features throughout the solid body. Although the repeatability and accuracy obtained through elastic averaging may not be as high as in deterministic systems, elastic averaging design can allow for higher stiffness, lower local stress, and improved load robustness when compared to exact constraint designs. In a well designed and preloaded elastically averaged coupling, the repeatability is approximately inversely proportional to the square root of the number of contact points [4].

3.1.2 *Examples of Elastic Averaging*

While the general concept of elastic averaging has been known for many years, the earliest appearances in the literature occurred only during the first half of the twentieth century in descriptions of ruling engines used to produce diffraction gratings. One of the first appear-

ances of elastic averaging was the use of leather nuts in the 1700's to improve the precision of machines. The first published instance was Henry Rowland's use of a wooden nut in his ruling engine [13], although Sir Thomas Merton is given credit for most effectively employing the principle with the creation of the Merton Nut to eliminate periodic errors during the replication of diffraction gratings [10]. Merton's integrating nut was formed by first ruling lines onto a smooth cylinder using a normal lathe. Due to errors inherent in the ruling lathe, the individual lines could not meet the necessary accuracy requirements. However, summed over a sufficient number of lines, these errors average out to provide the required accuracy. To leverage the averaging action, Merton introduced a compliant nut composed of a brass tube with an inner diameter approximately 0.125 inches larger than the ruled cylinder and three small strips of cork cemented within the brass tube at 120 degrees from each other. Contact between the tube and ruled cylinder was made through the strips of cork, which provide the elastic averaging action. Averaging occurs as small errors in the ruled lines are absorbed by compliant threads formed in the cork and as larger errors are reduced through a small measure of slip between the teeth and cork. As the cylinder rotates, the nut moves along the ruling lines at an averaged lead, carrying an attached diamond tool which machines a separate untouched area of the cylinder. The resulting ruled lines can be transferred to a diffraction grating with practically all periodic errors removed. While Merton's original experiment was capable of generating accurate lines at 2000 divisions per inch, a refined version by Sayce was capable of optically ruling 5000 lines per inch on an photographic plate [12].

The first instance referring to the term elastic averaging appears in a paper in 1951 by Strong [11]. In this paper, Strong developed a ruling engine which employs elastic averaging to create a dividing head generator using a large number of triangular laps. These lapping tools acted as cantilever springs and were mounted on a disc which moves normal to the workpiece. Several years later in his review of elasticity in instrument design, R.V. Jones next mentions the term elastic averaging to describe the integrating behavior of the Merton Nut. In this paper, Jones also first qualitatively mentions the understanding that the accuracy of an elastically averaged interface is on the order of $n^{1/2}$ times better than

the accuracy of the contacting elements, where n is the number of simultaneously engaged contactors [13].

After Jones, references to elastic averaging are difficult to find, although the principle is used in several different products, including curvic and Hirth couplings, wiffle trees, and plastic building blocks such as Legos™. Hirth

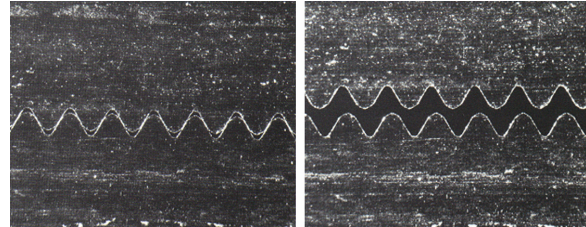


Figure 3.1 Open and closed photographs of elastically averaged tooth couplings (figure by W. R. Moore [14])

and curvic couplings, used in serrated tooth circle dividers, are examples of elastically averaged couplings [14]. These coupling types use different forms of face gear teeth (straight and curved, respectively) to form a coupling between two components, as shown in Figure 3.1. While both coupling faces are the same diameter and have equal tooth geometry and size, small errors during manufacturing will cause slight interferences or slight gaps between the teeth when the couplings are first engaged. When the couplings are clamped together under preload, the teeth wear in at first, then elastic deformations at the contacts cause the manufacturing variations to be averaged out over all of the teeth. This type of coupling provides good repeatability and high stiffness and is commonly used for indexing tables and indexing tool turrets as shown in Figure 3.2, as well as in the drive trains of some aircraft engines. Curvic couplings, for example, can be obtained commercially from the Gleason Corporation. HSK also employs flat surfaces on thin ring features in their tool holders to achieve a similar effect.

Another common example of elastic averaging is the concept of a compliant wiffle tree. The traditional mechanical wiffle tree contains a stacked arrangement of members which pivot to accommodate errors in the parts. Since the pivots have effectively no stiffness, a traditional wiffle tree is an exact constraint device. However, a wiffle tree becomes elastically averaged if the structure consists of a stacked arrangement of compliant members which funnel from a large number of contact regions on one surface to a specified number of fixed mounts on the opposing surface. Commonly, a compliant wiffle tree design is

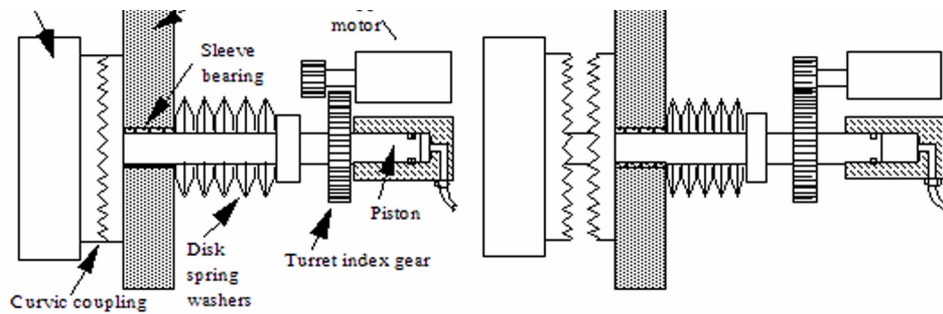


Figure 3.2 Schematic of a typical turret indexing and locking mechanism in engaged and disengaged positions using a curvic coupling (Courtesy of Hardinge Brothers, Inc. from Slocum [4])

used in the structure of automobile windshield wipers to ensure that the wiper blade remains in contact with the windshield through a wide range of motion. More advanced wiffle tree applications include the support of large mirrors for large optical telescopes. In this case, the weight of the structure cannot be supported by a purely kinematic constraint due to high contact forces, while the wiffle tree can distribute these forces amongst a large number of elements [4]. Wiffle trees have also found use in the aircraft industry in wing test structures [15]. A compliant wiffle tree structure for parallel testing of numerous semiconductor elements was created using flexures by Slocum and is shown in Figure 3.3.

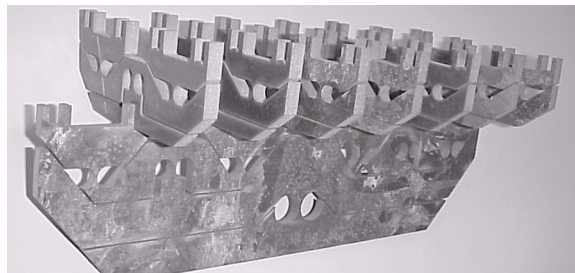


Figure 3.3 Compliant wiffle tree structure created by Slocum for a semiconductor tester

An interesting application of elastic averaging in the natural world is the use of a wiffle tree like structure on a gecko's foot. The end of a gecko's foot is covered in tiny little hairs which branch in wiffle tree fashion until their ends reach the microscopic level. Because of elastic averaging, the compliant hairs deform to ensure that all of the microscopic ends

come in contact with a surface, allowing Van der Waals forces to hold the gecko to smooth surfaces [16].

Perhaps the most common examples of elastic averaging today are the plastic toy blocks from LEGOTM¹. When two bricks are joined, the projecting cylinders on one brick mesh with a thin web on the second brick to create a small interference fit. The forced compliance of the bricks causes the cylinders and web to deflect, but elastically return when the blocks are separated for many

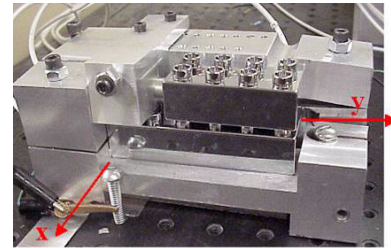


Figure 3.4 Lego brick setup for evaluation of repeatability using elastic averaging principle with plastic parts

cycles. Recent work by Weber experimentally determined the repeatability of chrome plated LEGO DUPLO blocks using a series of capacitance probes shown in Figure 3.4 [18]. In the experiments, it was loosely shown that the repeatability of elastic averaging is inversely proportional to $n^{1/2}$. Also, the experiment showed that LEGO DUPLO bricks are repeatable on the order of several microns!

In the same work, Slocum and Weber also developed a set of elastically averaged features for precision passive alignment of multiple wafers in micro-electromechanical systems, interconnects, and wafer stacks. The coupling features comprise rows of concave V-shaped trenches on one wafer and convex pyramid structures on the other wafer. To allow for elastic averaging, the pyramid structures are mounted on cantilever beams ground on the wafer. The trench, pyramid, and beam features are all created in a microfabrication laboratory using lithography, isotropic, and anisotropic etching as shown in Figure 3.5 and Figure 3.6. When two wafers come in contact, the pyramid structures engage the v-trenches, and the beams begin to bend for features where the tolerance errors have acted in the contact direction. Vibration dithering is then applied to the wafer stack to overcome friction and preload is applied.

1. LEGO is a registered trademark of the LEGO Group and LEGO Systems, Inc., Enfield, CT 06083 USA

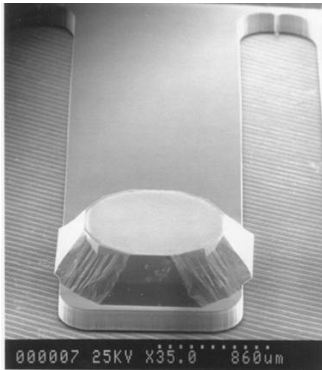


Figure 3.5 - Convex pyramids on cantilever tips on wafer 1

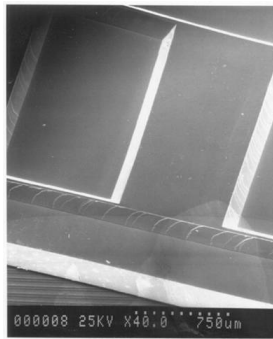


Figure 3.6 - Array of mating concave structures on wafer 2

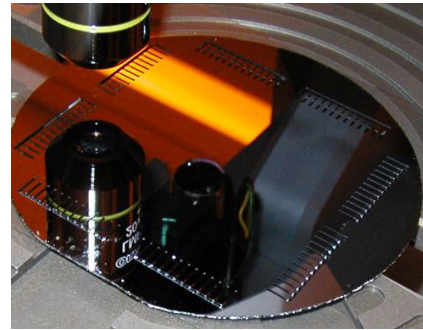


Figure 3.7 - Testing of passively mechanically aligned wafers

After sufficient preload is applied, all of the features should be in contact and all of the beams should be deflected by some amount. The sum of all the manufacturing errors are elastically averaged through the compliance of these beam structures to provide for repeatability on the order of $1\mu\text{m}$. In these experiments, the effect of the number of contact points was also investigated by breaking of certain numbers of contacting elements and repeating measurements. Due to the reduced random errors inherent in microfabrication processes and the $1\mu\text{m}$ resolution of the alignment and measuring system, the previously mentioned proportionality was not seen. Since accuracy was hypothesized to be systematic as caused by misalignment between the mask and wafer, the authors concluded that only a small number of contact features, as small as eight, are required for good repeatability.

A final instance of elastic averaging of recent note is the development of a compliant and self-locking tapered torsional coupling [19]. This coupling consists of two identical elements containing a series of finger features mounted circumferentially which mesh with finger features on the matching coupling as shown in Figure 3.8. When the coupling is engaged, the fingers act as cantilever beams with the deflecting force being provided by the base of the neighboring beams. The geometry of the beam tip is optimized to be self-locking, so that axial force caused by engaging the coupling will deflect the beam tips radially; however, applied torsional loads cannot cause additional radial deflection. Elastic

averaging occurs both in the circumferential and radial directions by ensuring that the finger end is relatively compliant in that direction compared to the root. Data on the repeatability and accuracy of this coupling was not readily available.

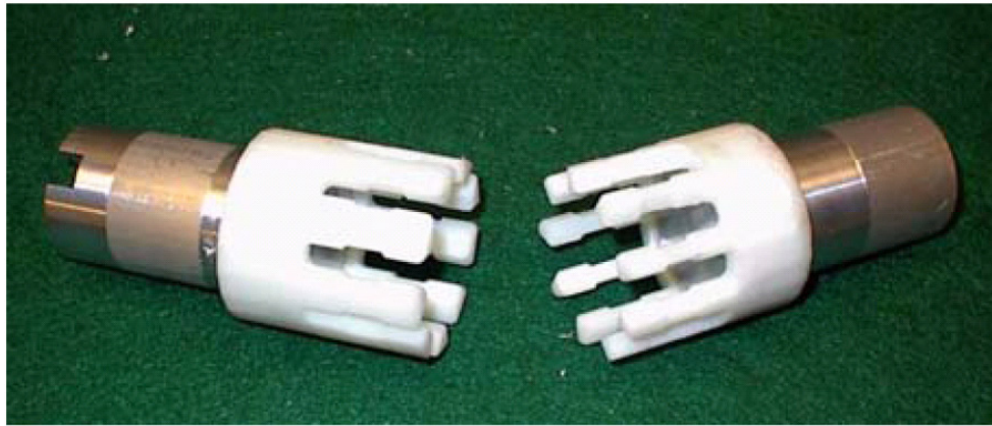


Figure 3.8 Example of elastically averaged torsional coupling [19]

3.2 Modeling and Analysis of Elastic Averaging

3.2.1 Background

While there are few references to elastic averaging available, even fewer are available relating to analytical methods for describing these types of couplings. The most likely reason for this absence is that the analysis is often intractable due to complex geometry and difficult solution methods. Often, designers also shy away from elastic averaging due to the implied risk from possibly having an overconstrained system. Assembly or disturbance forces can cause damage to the contacting elements if the design is not robust. As with any coupling, environmental contamination can decrease a coupling's performance by changing the effective dimensions or damaging contacting elements. Elastically averaged couplings with small numbers of contacting elements tend to be very prone to these effects, while higher number of elements can average out isolated errors.

Two possible routes are available for modeling and analyzing a coupling system - closed form analytical solutions and finite element solutions. For elastic averaging, closed form

solutions are only possible for the simplest of geometries, such as simple beams, flexures, and springs. Beyond these simple geometries, assumptions required to use the simplified representations may no longer hold and it becomes increasingly difficult to mathematically describe the geometry. However, closed form solutions are extremely useful as they are parametric and permit complex statistical tolerance analyses without significant time spent manipulating models or equations. Conversely, finite element analysis (FEA) methods allow for both simple and complex geometries to be described with little effort, but often cannot do parametric tolerance analyses. When the FEA model is small and relatively simple, the FEA analyses can be developed by hand to retain parametricity and allow for quick solution times. Increasingly larger and complex models require the use of a separate software package to describe the geometry, apply boundary and loading conditions, and solve cases. While many packages include routines to determine sensitivities and the worst case effect of tolerances, it is often difficult, if not impossible, to combine FEA results to easily predict statistical behaviors such as interface accuracy and repeatability in a parametric way.

3.2.2 Overview of an Elastic Averaging Modeling Process

It is the goal of this chapter, therefore, to develop a hybrid model of elastic averaging combining aspects of both closed form solutions and FEA as necessary. The basic methodology of this process is to create a simplified model of the interface where the connecting parts are joined by a number of springs equal to the number of contact points. Each spring represents the compliance of that contacting point due to material parameters, geometry, and coupled kinematics between the contact points. Initial tolerances at each contact point in a local coordinate system can be converted into the forces at the contacts using a stiffness matrix formed from the contacting springs. These forces can be transformed to a global coordinate system for the parts, then can be reduced into forces and moments applied to one part. Combining these constraint equations with forces and moments in equilibrium equations provides a system of equations which can be solved for the final locations of the contact points. By repeatedly solving this system of equations

with randomly generated tolerances, repeatability of the coupling can be statistically determined for a specific point such as the center of stiffness.

The elastic averaging modeling process can be broken down into the following steps which will be discussed in more detail in the next subsections.

1. Build a model of the flexible elements in the coupling.
2. Determine sensitivity of dimensional parameters to tolerances.
3. Create a parameterized stiffness equation to predict the stiffness due to changes in the sensitive parameters.
4. Map the effect of cross coupling of contact points.
5. Form local stiffness matrices for each contact point and merge to form a global stiffness matrix for the system.
6. Combine force and moment equilibrium conditions with geometric constraint equations.
7. Find deflections, forces, and other engineering quantities.

A simple extensible example of a completely closed-form model is shown in section Section 3.3 below, while the complete hybrid approach is demonstrated on a new fiber optic connector design in Chapter 4.

3.2.3 Detailed Description of Process Steps

Step 1 - Build an analytical model of the flexible elements in the coupling.

To construct the analytical model, each flexible element or interface should be replaced by an equivalent spring which represents both the geometric and material behaviors of the elements. Geometric behavior of most flexible elements can generally be easily modeled using traditional beam bending equations available from most undergraduate mechanics textbooks (e.g. [20] or [21]). For more complex cases, the classic Roark's Formulas for Stress and Strain can help with problems such as complicated boundary conditions, curved beams, and tapered beams, as well as references for developing more advanced cases [22]. In cases where closed form equations are not possible or too difficult, a finite element model can be constructed which can directly provide the stiffness matrix for simple cases

or can be used to map the stiffness of a contact region by running a series of FEA simulations. No real metric can be developed to instruct a designer when FEA is required instead of a closed form solution for the infinite range of possible geometries that could be conceived. In general, a design that utilizes relatively simple, linear flexible elements such as the torsional coupling mentioned above can be easily modeled using traditional beam bending equations, while large changes in curvature tend towards intractable equations. The torsional coupling could be modeled by replacing each of the flexible fingers with an equivalent spring extending from the root to a common point at the contacting surface. For 12 fingers, the torsional coupling could possibly be modeled as shown in Figure 3.9. These springs would be composed of separate elements to describe both the radial and circumferential compliance as cantilever beams. If an FEA solution is used, the stiffness result derived from the analysis can easily replace the cantilever beam equations.

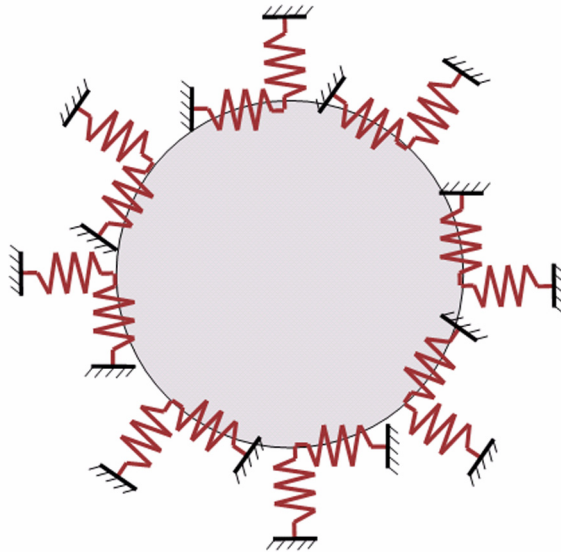


Figure 3.9 Sample equivalent spring model for the torsional coupling

In addition to compliant behavior of the geometry, certain material or mechanical behavior can introduce additional compliances into the interface. Since many coupling geometries involve point or line contacts, compliance due to Hertzian contact stress can become important. The equations describing Hertzian contact will not be reiterated here, although

their implementation is shown in Appendix C. Complete details on the theory can be found in Johnson's detailed handbook on contact mechanics [6] or in precision design references [4]. In most cases, the contact mechanics relationship can be reduced to a compliance in series with the geometric compliance, but dependent on the local contact geometry and material properties.

Step 2 - Determine sensitivity of dimensional parameters to tolerances.

After creating a model, the next step is to determine which key dimensions in the model have a greater effect on the location and stiffness of the elements. Analytically, these parameters can be found purely by investigating the sensitivities of the equations for each dimension. For example, the stiffness of an end loaded cantilever beam is highly sensitive to the length of the beam and changes in this dimension can affect the stiffness of the beam greatly.

More complex geometries like the web of a LEGO brick or the connector design shown in Chapter 4 require FEA simulations to determine sensitive parameters. Most commercial FEA codes currently provide some algorithms for determining sensitive parameters, usually as a feature within design optimizations. These algorithms generally provide an curve fit equation, graphical representation, or relative numerical value expressing the relationship between a change in displacement or stress to a particular dimension. Many solvers allow for multiple dimensions to be analyzed simultaneously, reducing solution time greatly.

Step 3 - Create a parameterized stiffness equation.

Based on the results of steps 1 and 2, a parameterized stiffness equation can be constructed. If the system can be described in closed form, the equations can be manipulated relatively easily to provide an equation expressed in terms of the important parameters. When FEA solutions are required, a series of FEA "Experiments" is required to map the stiffness of an individual contact as a function of the changing dimensions and specific loading conditions. Some solvers may include routines which will automatically run sev-

eral analysis cycles and provide displacement as a function of one or more dimensions. This feature makes generation of a parameterized stiffness equation almost automatic. However, if the solver does not provide such a feature, the designer will have to develop the equation manually by generating data for a variety of dimensional combinations and then creating a curve fit to accurately predict stiffness within an acceptable tolerance range.

Step 4 - Map the effect of cross coupling of contact points.

In many cases, the force acting at a contact point is not simply just a linear relationship to the deflection seen at that contact point. Two forms of cross coupling between contact points affect this relationship. The first form of coupling is the relationship between the force or displacement at one contact point to the corresponding displacement or force at the contact point of interest, often called stiffness or flexibility influence coefficients in literature on vibrations [23], applied mathematics [24], or the finite element method [25]. When stiffness is expressed in matrix form, those coefficients representing a non-coupled stiffness are placed along the diagonal, while the cross-coupled influence coefficients are present as the non-diagonal terms. From Maxwell's Reciprocity Theorem, it can be determined that the deflection at a contact point i due to a unit load at point j is equal to the deflection at point j due to a unit load at point i . In other words, the stiffness matrix is symmetric. A sample stiffness equation for a four spring version of the system in Figure 3.10 is shown in Equation 3.1.

$$\begin{bmatrix} F_1 \\ F_2 \\ F_3 \\ F_4 \end{bmatrix} = \begin{bmatrix} k_{11} & k_{12} & k_{13} & k_{14} \\ k_{12} & k_{22} & k_{23} & k_{24} \\ k_{13} & k_{23} & k_{33} & k_{34} \\ k_{14} & k_{24} & k_{34} & k_{44} \end{bmatrix} \begin{bmatrix} x_1 \\ x_2 \\ x_3 \\ x_4 \end{bmatrix} \quad (3.1)$$

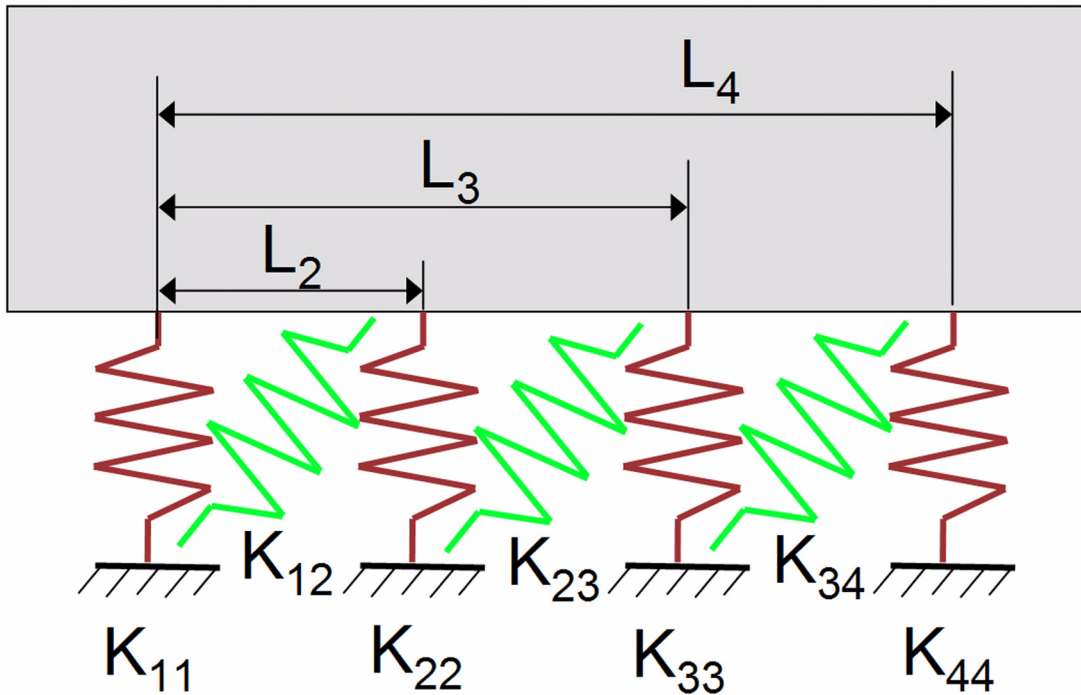


Figure 3.10 - Example of elastic averaging including force cross coupling

Force cross coupling is present in almost any elastically averaged coupling, although the effect may be negligible in some cases. For closed form models, the complete stiffness matrix can be determined by analyzing the coupling as a multi-degree of freedom system using equilibrium equations [23]. The stiffness matrix can be formed directly from the FEA formulation, if the model is created manually, or by mapping forces and deflections within a particular software package.

The second form of cross coupling is the relationship between a deflection at one point to a deflection at the point of interest. This cross coupling can exist when one contacting element is physically connected to another element, but it does not exist in cases where each contacting element is physically independent. For the torsional coupling, displacement cross coupling does not exist. Since each finger is relatively compliant compared to the base, a displacement at one contact is not transmitted to neighboring elements. Displace-

ment cross coupling would exist for a simplified case where a rigid part is mounted on a large number of springs connected to a common flexible member.

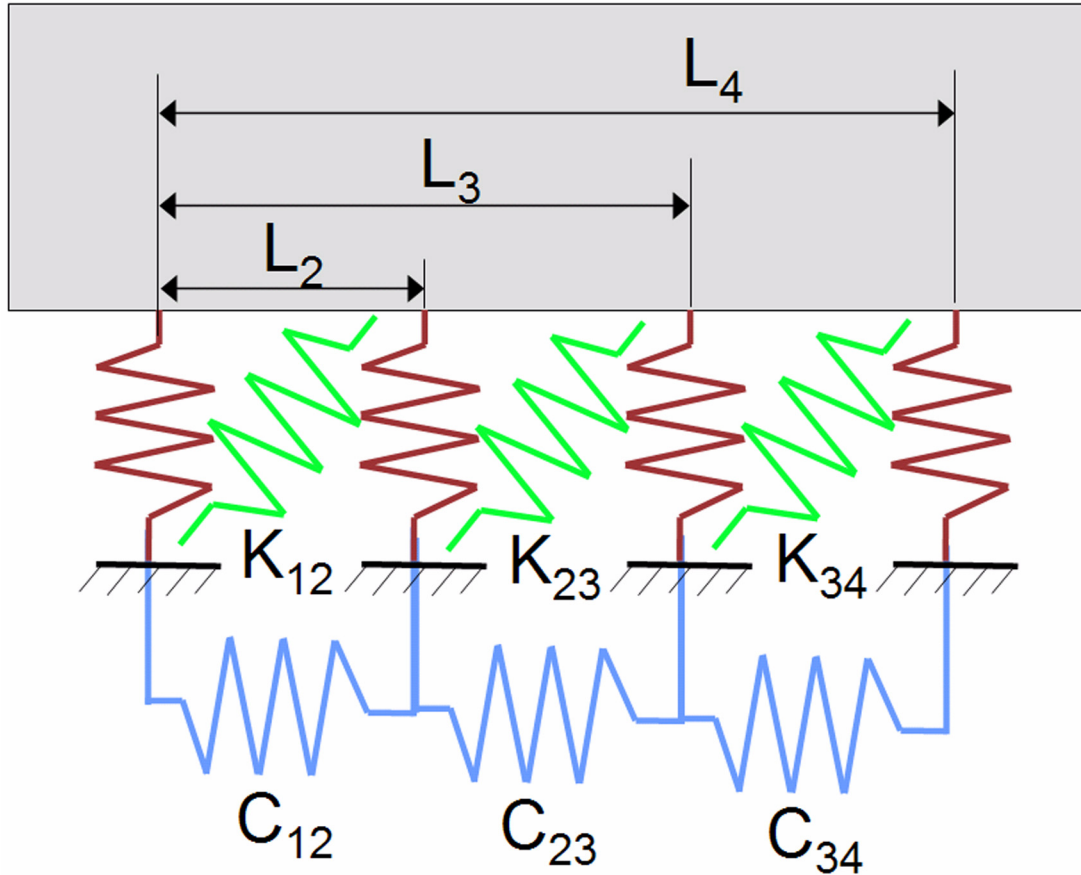


Figure 3.11 - Example of elastic averaging including force and displacement coupling

Based on the relative compliance between the springs and the flexible member, an error motion at one point on the member would be observed at the neighboring contact points. A rigid beam would show almost a solid body motion and rotation, while a more compliant beam would exhibit relative deflections between the contact points. This simple case could be modeled simply using beam equations, while the behavior of more complex geometry can be mapped using an FEA model. In the FEA model, the contact points should have an initial force or deflection corresponding to the nominal preload or press fit configuration, then individual contact points can be disturbed to determine the coupled motions. Symmetry in the coupling design is beneficial as less contact points require probing to completely understand the coupling effect. In Equation 3.2, an example of the dis-

placement cross coupling is shown for the four spring system in Figure 3.11 through the matrix composed of cc elements.

$$\begin{bmatrix} F_1 \\ F_2 \\ F_3 \\ F_4 \end{bmatrix} = \begin{bmatrix} k_{11} & k_{12} & k_{13} & k_{14} \\ k_{12} & k_{22} & k_{23} & k_{24} \\ k_{13} & k_{23} & k_{33} & k_{34} \\ k_{14} & k_{24} & k_{34} & k_{44} \end{bmatrix} \begin{bmatrix} cc_{11} & cc_{12} & cc_{13} & cc_{14} \\ cc_{12} & cc_{22} & cc_{23} & cc_{24} \\ cc_{13} & cc_{23} & cc_{33} & cc_{34} \\ cc_{14} & cc_{24} & cc_{34} & cc_{44} \end{bmatrix} \begin{bmatrix} x_1 \\ x_2 \\ x_3 \\ x_4 \end{bmatrix} \quad (3.2)$$

At this point, an interesting qualitative metric relating coupling to constraint can be noted. A ratio between the direct stiffness designed into the system and the cross coupling can be determined. For small values of this ratio, the direct stiffness between the components dominates their interaction and the system is elastically averaged. For large values of this ratio, the structure is much more compliant than the components intended to exhibit compliance or conversely the compliant structures are too stiff. In this case, the base part will exhibit elastically averaged like motion, although the parts can be damaged by this compliance. Ratio values close to one approach the case where the system is likely to be over-constrained, or possibly exactly constrained in cases of six contact points.

Step 5 - Form local stiffness matrices for each contact point and merge to form a global stiffness matrix for the system.

After determining the stiffness properties for each contact point, this stiffness should be expressed as a stiffness matrix in a local coordinate system for that point. It is useful to define the local coordinate system so that one axis is in the contact direction or normal to the contact surface while the other axis is tangential to the contact. By defining the local coordinates in this method, both normal and friction forces can be easily determined for a deflection. In Equation 3.3, an example local stiffness matrix is shown, where the line over the variable indicates that it is in local coordinates

$$\begin{bmatrix} \overline{F}_x \\ \overline{F}_y \end{bmatrix} = \begin{bmatrix} k_x & k_{xy} \\ k_{xy} & k_y \end{bmatrix} \begin{bmatrix} \overline{\Delta}_x \\ \overline{\Delta}_y \end{bmatrix} \quad (3.3)$$

The local stiffness matrices can then be transferred to a global coordinate system, which is common to all of the contacts and is typically defined with respect the coordinate system of one part as in Equation 3.4. This transformation is formed using the common tool called a transformation matrix, shown in Equation 3.5, where θ is the angle formed by \overline{x} and x , measured positive counterclockwise from x .

$$\begin{bmatrix} F_{x1} \\ F_{y1} \end{bmatrix} = T_1^T \begin{bmatrix} k_{x1} & k_{xy1} \\ k_{xy1} & k_{y1} \end{bmatrix} T_1 \begin{bmatrix} \Delta_{x1} \\ \Delta_{y1} \end{bmatrix} \quad (3.4)$$

$$T = \begin{bmatrix} \cos\theta & \sin\theta \\ -\sin\theta & \cos\theta \end{bmatrix} \quad (3.5)$$

Once the matrices are in the global coordinate system, the stiffness matrices for each contact point must be augmented to include the force cross coupling terms or zeros so that each contact's stiffness equation includes all possible displacements. These globalized, augmented equations can then be merged into a global stiffness matrix and combined with the displacement cross coupling terms to form a stiffness equation for the entire interface. This process of defining local stiffness equations and assembling into a global form is based on the Direct Stiffness Method, a precursor to the Finite Element Method [26], and it can be done simultaneously and automatically in most mathematics packages.

Step 6 - Combine force and moment equilibrium conditions with geometric constraint equations.

Using the completed global stiffness equations, form equations for force and moment equilibrium in all required degrees of freedom. To solve all of the system's unknowns, additional equations are required. These equations can be created using geometric constraint or compatibility equations such as constant slope

or specific displacements, which are highly dependent on the specific model. These equations can be arranged in a matrix format as demonstrated in Equation 3.6.

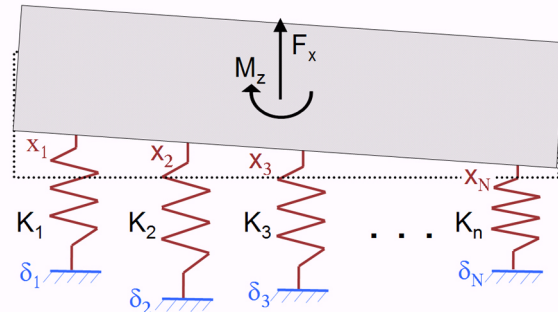


Figure 3.12 - Equilibrium for a simple 2D case where δ is the simulated tolerance of each contact point and x is the corresponding deflection of the part.

$$\begin{bmatrix} \text{force equilibrium equations} \\ \text{moment equilibrium equations} \\ \text{geometric constraints} \end{bmatrix} \begin{bmatrix} \text{vector of} \\ \text{displacements} \end{bmatrix} = \begin{bmatrix} \text{effective applied force} \\ \text{effective applied moment} \\ \text{zeros} \end{bmatrix} \quad (3.6)$$

Step 7 - Find deflections, forces, and other engineering quantities.

To find reactions of the coupling to applied or disturbance forces, the general form in Equation 3.6 can be applied. To simulate repeatability of a number of coupling pairs, a tolerance based statistical analysis is performed where a random normal distribution of dimensions is provided to a model in order to generate an output distribution of a variable such as total force or solid body motions. A Monte Carlo tolerance analysis is one of the most versatile statistical simulations using this method and is very accurate for large sample sizes. If the generated normal distributions have a mean at the nominal dimension and standard deviation of one third of the tolerance, the resulting output distribution can accurately predict the repeatability of the complete system. To use the elastic averaging model with statistical analyses, the effective applied force and moments terms on the right hand side of Equation 3.6 must be found by solving the force and equilibrium equations as shown in Equation 3.7.

$$\begin{bmatrix} F_{applied} \\ M_{applied} \\ 0 \end{bmatrix} = \begin{bmatrix} \text{uncoupled force \& moment equilibriums} \\ 0 \end{bmatrix} \begin{bmatrix} \text{vector of nominal displacements} \end{bmatrix} + \begin{bmatrix} \text{coupled force \& moment equilibriums} \\ 0 \end{bmatrix} \begin{bmatrix} \text{displacement coupling modifier} \end{bmatrix} \begin{bmatrix} \text{vector of tolerances} \end{bmatrix} \tag{3.7}$$

The elements in the vector of tolerances necessary for solving these equations can be formed by generating random values for dimensions and determining the change in location of the contact point. With the applied forces and moments, Equation 3.6 can then be solved for the displacement vector. Repeated generation of tolerance data and solution for the displacement vector can then be used to determine repeatability across a number of coupling pairs.

3.3 Simple Example - One Dimensional Rigid Beam

3.3.1 Example Description and Application of Model

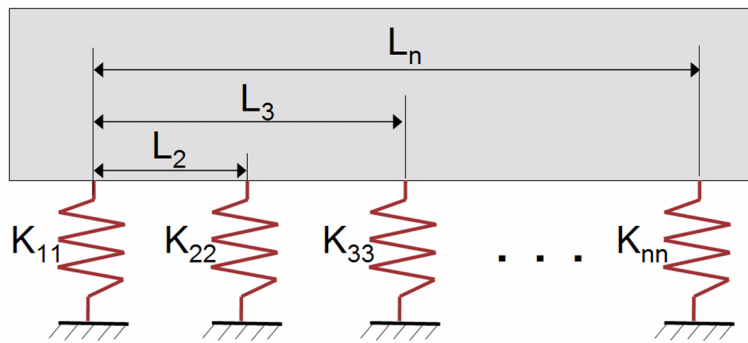


Figure 3.13 - Schematic of simple one dimensional rigid beam model

To illustrate the use of the elastic averaging model, it was applied to the simple one dimensional problem shown in Figure 3.13. The problem consists of a beam which is assumed to be rigid so that all deflections occur within the springs. Since the contacts are all fixed to the beam, the stiffness matrix will include the influence coefficients. To make this problem as simple and general as possible, it is assumed that the coupling effect will

follow St. Venant's Principle and be negligible after three critical dimensions. Therefore, the diagonal terms of the stiffness matrix are defined to have the stiffness values of that individual spring. The nearest neighboring contacts will have 10% of this value while the second neighbors will have 1%. Similarly, the displacement cross coupling is defined so that the first and second neighbors exhibit coupling. For this analysis, the effect of displacement cross coupling was varied to determine its effect on the $1/n^{1/2}$ behavior. When forming the matrices in Equation 3.6 and Equation 3.7, moment equilibrium was calculated with respect to the center of stiffness. The geometric constraints were applied by assuming that the beam remains rigid and the slope of the beam remains constant along its length. To simulate the tolerances of the system, a random distribution of displacements was provided with a mean of zero and a standard deviation of one. Since the mean displacement is zero, the vector of nominal displacements is zero and only the tolerances will cause motion of the beam. Effectively, these tolerances are applied to the ground shown in Figure 3.13. The complete mathematics and details of this model are shown in Appendix B. Mathematics are presented in MathCAD 11 from Mathsoft and are unitless.

3.3.2 Results from Simple Model

Since the primary goal of this analysis is to determine the effect of cross coupling on system repeatability, a number of studies were run with varied numbers of contacts and different combinations of cross coupling. In Table 3.1 and Figure 3.14, a summary of simulation results is shown consisting of the standard deviations from 2000 or more data points generated for each case.

TABLE 3.1 Summary of Results Statistics

Number of Contacts	$1/n^{1/2}$	Standard Deviation for No Cross Coupling	Standard Deviation for 10% Force Cross Coupling	Standard Deviation for 10% Displacement Cross Coupling
5	0.447	0.447	0.432	0.534
10	0.316	0.319	0.323	0.384
25	0.200	0.192	0.196	0.246
50	0.141	0.142	0.139	0.175
75	0.115	0.117	0.115	0.139
100	0.100	0.104	0.101	0.120
250	0.063	0.063	0.064	0.078
500	0.045	0.043	0.045	0.054

In each of the three cross coupling variations, it is expected that the standard deviation for location of the center of stiffness should follow the trend of $1/n^{1/2}$. Since the standard deviation placed on the random tolerance distribution is 1, it is also expected that the standard deviation for the output location be equal to the value of $1/n^{1/2}$. Without cross coupling, this expectation holds true with the resulting distribution being essential equivalent to the square root trend. For modest values of force coupling, a negligible change in output

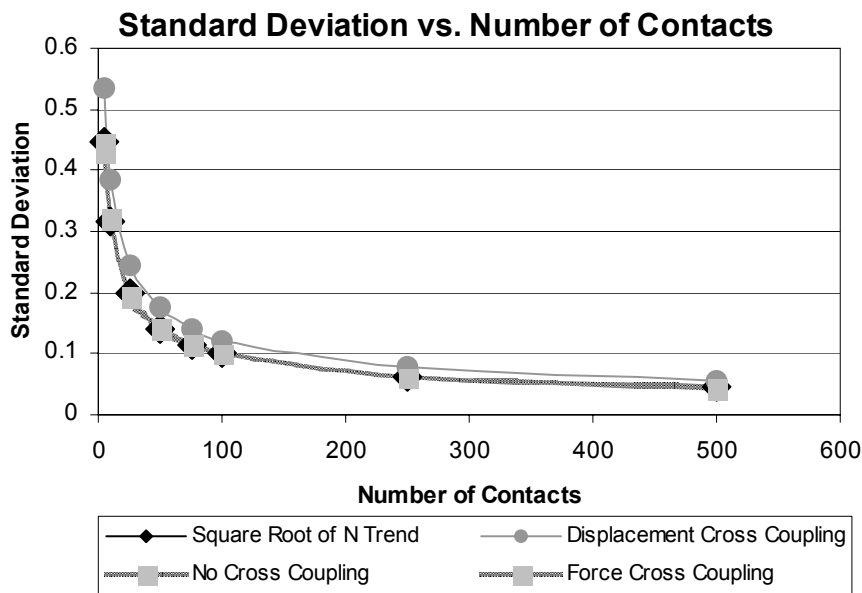


Figure 3.14 - Plot of standard deviation versus number of contact points for various cross coupling cases

repeatability is observed. However, even small values of displacement coupling have a noticeable effect on the repeatability of the system. Any change in displacement coupling appears as a polynomial effect as shown in Figure 3.15. This polynomial effect is called the *displacement cross coupling factor*, defined as shown in Equation 3.8, and has a polynomial function for this simple model shown in Equation 3.9.

$$\sigma = DCCF \frac{1}{\sqrt{N}} \quad (3.8)$$

$$DCCF = 2.01 \times \text{percent}^2 + 1.92 \times \text{percent} + 1.01 \quad (3.9)$$

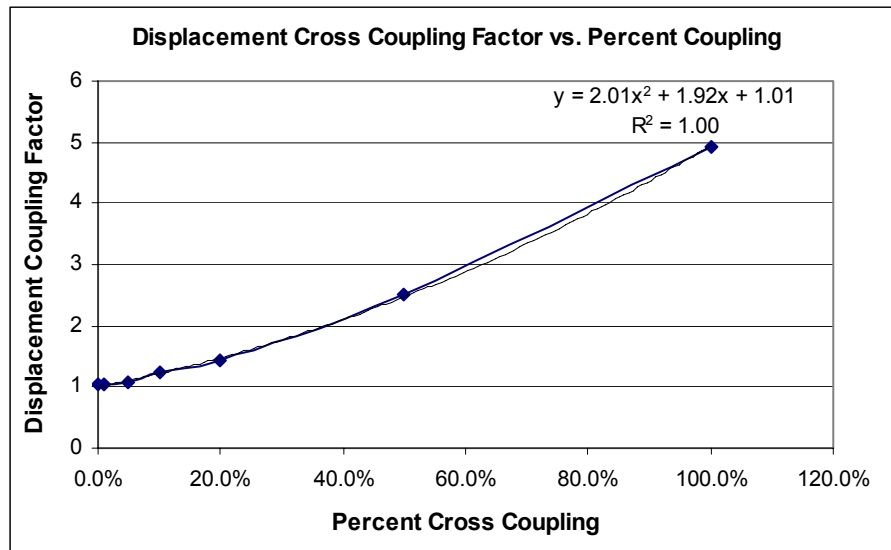


Figure 3.15 - Plot of displacement cross coupling factor based on percentage of cross coupling

Similarly, angular standard deviations show correlation to the $1/n^{1/2}$ trend, scaled into angular units. Also, displacement cross coupled cases show a degradation with increasing coupling percentage while force cross coupling has a negligible effect.

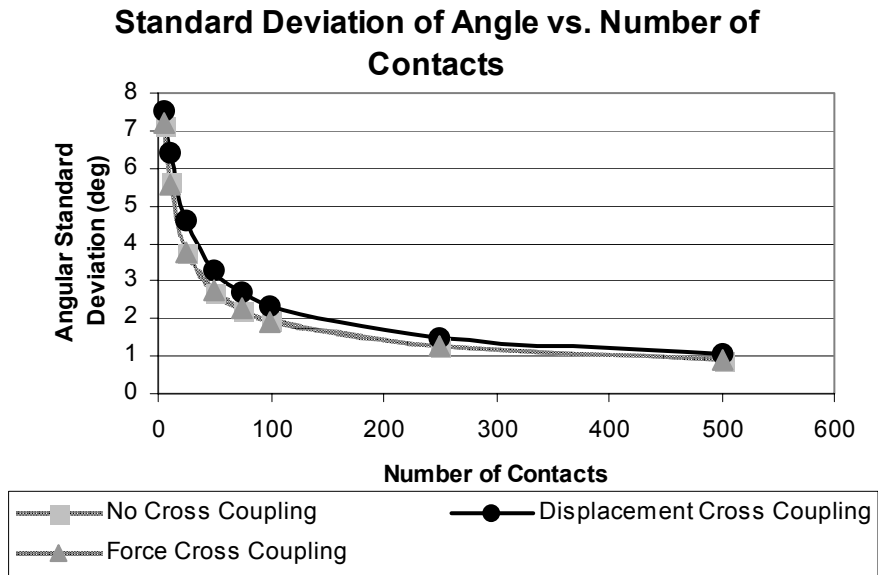


Figure 3.16 - Plot of standard deviation of angle versus number of contact points for various cross coupling cases

Chapter 4

DESIGN CASE STUDY: FIBER OPTIC CONNECTOR

4.1 Problem Description

Fiber optics can be considered one of the most important technological developments in the 20th century. While most people are unaware of their use, fiber optic cables have revolutionized the communications industry by improving the quality of telephone and television signals, as well as enabling the internet to drastically expand and develop. The first successful use of fiber optic technology occurred during the 1950's with the development of an image transmission device called a fiberscope. This device had a limited usefulness as original all-glass fibers exhibited excessive power loss. With the development of high quality light sources such as lasers and light emitting diodes, engineers realized that optical fibers could be used for communications if their lossiness could be reduced. This realization spurred a surge in the development of pure glasses, transmission and receiving devices, and techniques for joining fibers. During this development, a wide range of demountable connectors were created to allow a fiber cable to be separated and connected repeatably a number of times. However, connector designs were mostly limited to variations on a few concepts which could not be efficiently extended to house large numbers of cables. In addition, existing connectors are too costly and lossy to be used in plans for fiber connections to the home.

Therefore, an ideal example application for elastic averaging and the Silicon Insert Molded Plastics process (the SIMP process is described in Chapter 5) is the development

of a low cost method for the alignment and mating of optical fibers. Multi-mode fibers have fairly generous alignment tolerances, on the order of three to five microns, while single mode fibers require alignment on the order of a half micron. While current manufacturing methods work, the popular multi mode MT ferrule may cost on the order of \$50 and may have 1/2 - 1 dozen small parts, including the spring preloading mechanism. By combining elastic averaging and the SIMP process, a cost reduction of an order of magnitude should be possible without any reduction in precision, as well as a reduced part count to three parts.

In this chapter, some basic information regarding fiber optics will be discussed as background to connector design, then a design concept employing elastic averaging and the SIMP process will be described. The elastic averaging analysis process outlined in Chapter 3 will be applied to this new design, including simulations and some experimental results.

4.2 Background

4.2.1 Basic Optics for Fiber Optics

The theory of optics related to fiber optics is quite extensive, detailed, and complex. Only the basic relevant details pertaining to understanding connectors will be presented here and further detail can be found in many optics textbooks (e.g. [27] or [28]). The fundamental principle that makes optical fibers possible is total internal

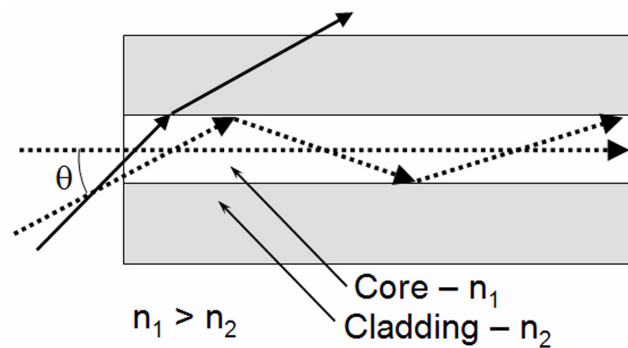


Figure 4.1 - Schematic of total internal reflection in optical fiber - dashed lines show reflected rays while solid lines show refracted or lost rays.

reflection (TIR). TIR is a property of light extending from the ray model of light, as shown in Figure 4.1. Rays of light entering the fiber travel down a core of material with a larger index of refraction than a thin outer layer called cladding. This difference in index causes

light to reflect inside the core when it is incident on the fiber's surface within a certain critical angle. The light within the fiber is then considered to be totally internally reflected inside the fiber, while light outside the angle is refracted into the cladding and lost. The critical angle can be determined from Snell's Law of Refraction, as it defines the angle when light will refract or reflect at this surface. In the case of a fiber in free air, this relationship can also be quantified by the parameter called numerical aperture which is constant for a specific fiber and is defined in Equation 4.1.

$$\sin\theta_{critical} = \frac{n_{clad}}{n_{core}} \quad (4.1)$$

$$NA = \sin\theta = n_0 \sin\theta_c = \sqrt{n_1^2 - n_2^2}$$

4.2.2 Fiber Types

Typically, optical fibers are thin and flexible cylinders made of transparent materials such as glass and plastics capable of acting as a dielectric wave guide. The most commonly used material is ultra-pure glass based on silica due to its extremely low loss properties, although they are more fragile and susceptible to bending losses. The general design of a fiber is a cylindrical core of index of refraction n_1 in which the light travels surrounded by a layer of glass of lower index of refraction n_2 called the cladding. The glass is then covered in protective layers of plastic and other materials. In a fiber, the number of modes that can be transmitted along the fiber is dependent on the diameter of the core. A mode is the distribution of electromagnetic energy that satisfies Maxwell's equations and boundary conditions within a fiber, essentially a possible path which the light rays can follow. As the diameter of the fibre is reduced to a few microns, it becomes possible that only one mode can exist within the fiber. This type of fiber is called single mode fiber.

Single-mode Fiber

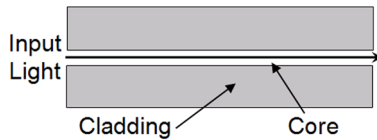


Figure 4.2 - Schematic of a single mode fiber

Since the core of a single mode fiber is so small, this form of fiber has essentially a step change in index of refraction at the core-cladding border. For a number of reasons, single mode fibers have less dispersion and attenuation over long distances, allowing them to transmit a higher capacity of data at a faster rate. These benefits indicate that single mode fiber is best applied for long distance communications. When designing connectors, single mode fibers have a number of disadvantages relating to the difficulty of launching light into the smaller core size. This difficulty directly relates to much tighter tolerances for connectors and splices that can be used for single mode fibers. Also, the geometric ray model of optics is less accurate for single mode fibers and the more unwieldy electromagnetic theory of light is required to model the interfaces.

Multimode Fiber

Multimode fiber was the first type of fiber to be manufactured and commercialized, simply due to the ease of creating the larger diameter. Compared to single mode fiber, this fiber type has a much larger core diameter, allowing for a larger number of modes. Because of the larger diameter, multimode fiber is easier to couple; however, these fibers exhibit more loss and are best used for short transmission distances such as local networks.

Multimode fiber may be further classified as step-index or graded-index fiber. If both n_1 and n_2 are uniform across the fiber cross section, the fiber is called a step index fiber, while fibers with decreasing n_1 along the core radius are called graded index fibers. The difference between stepped and graded index fibers becomes important when considering the different modes of light that can travel in a fiber. If multiple wavelengths of light are travelling down a stepped index fiber, all rays will reflect at the core-cladding interface. Since each ray has a slightly different wavelength, the rays will travel at slightly different

speeds. For long fiber lengths, this difference becomes important as the modes will disperse and simultaneously transmitted rays will arrive at separate times, causing loss of data when separate pulses merge. Figure 4.3 illustrates this problem for a multi-mode fiber.

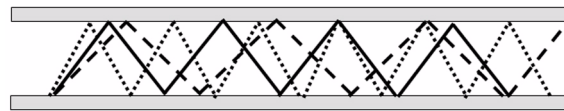


Figure 4.3 - Schematic of rays in a step-index multimode fiber

In a graded index fiber, the gradual change in index of refraction causes different modes to gradually decrease speed away from the core. This causes the rays to reflect at different diameters and the paths of each mode to become sinusoidal. In effect, the change in path reduces dispersion by directing each mode to travel along the fiber with the same effective velocity.

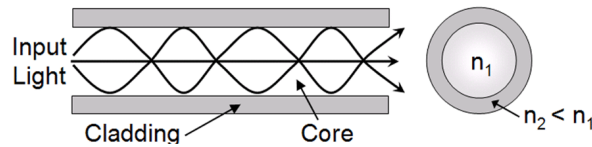


Figure 4.4 - Schematic of rays in a graded-index multimode fiber

In most cases, both single and multi-mode fibers have a cladding diameter of 125 μm . The core cladding varies depending on the number of modes. In Table 4.1, the most common fiber dimensions are listed.

TABLE 4.1 Common Fiber Core and Cladding Size

Fiber Type	Cladding Diameter	Core Diameter
Single Mode	125 μm	9 μm
Multimode	125 μm	50 μm
Multimode	125 μm	62.5 μm
Multimode	125 μm	100 μm

4.2.3 Connecting Fibers

In the past, the joining of fibers was considered somewhat a black art that required highly trained technicians. However, the development of improved fibers, joining processes, and

connecting devices have improved the reproducibility of joints. For a low loss joint, the parameters of the two fibers must be closely matched, including NA, index of refraction, and other quantities. Lateral, angular, and longitudinal misalignments between the two fibers also increase loss, in order of decreasing effect. Insertion loss, or the loss of power from inserting a component, is measured in decibels and is defined by:

$$Loss = -10 \log_{10} \left(\frac{P_{out}}{P_{in}} \right) = -10 \log_{10}(T) \quad (4.2)$$

The output to input power ratio in Equation 4.2 can be difficult to calculate for optical fibers, although a number of assumptions allow the equations for graded index multimode fibers to be solved relatively easily. These derivations and their resulting equations were first developed by Marcuse [29] and can be found in various forms from many sources ([30], [31] or [32]). All power loss calculations in the following analysis will be performed assuming multimode fibers are used. Each of the fiber parameters and misalignments mentioned above have a separate power ratio. The most critical values for fiber optic connectors are the lateral and angular misalignments:

$$T_{lateral} = \frac{2}{\pi} \left[\text{atan} \left(\frac{d \cdot e}{x} \right) - \frac{x \cdot e}{d} \right] \quad (4.3)$$

$$e = \sqrt{1 - \frac{x^2}{d^2}}$$

$$T_{angular} = 1 - \frac{n_0 \cdot \theta}{\pi \cdot NA} \quad (4.4)$$

where x is the lateral misalignment, θ is the angular misalignment, n_0 is the index of refraction for air, and NA is the numerical aperture.

Splices

Splicing is a permanent joint connection, generally used in the field to connect long sections of fiber cable due to low splice losses. To keep attenuation low, fibers must be joined

with lateral alignment precision of less $1\mu\text{m}$ which requires special equipment and magnification. There are two forms of splicing - mechanical and fusion. A mechanical splice uses an epoxy adhesive to match the refractive indices of the fibers and clamps are used to secure the fibers. A fusion splice uses heat to melt and fuses the two cables together. Fusion splices are very low loss if done properly and can retain the strength of the cable.

Demountable Connectors

While low-loss splices are beneficial for long cable lengths, demountable connectors are desired for shorter lengths which require repeated connect-disconnect cycles. Demountable connectors are permanently connected to the end of an individual fiber cable or a ribbon of fibers using adhesives or physical constraints. A wide variety of different connector

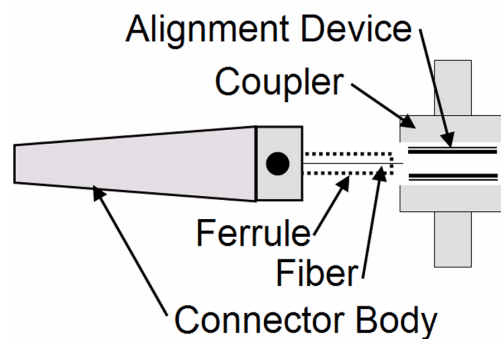


Figure 4.5 - Schematic showing components in a typical fiber connector

designs have been developed to meet a variety of different applications and each design has advantages and disadvantages. However, almost all connectors consist of the same three basic components, as shown in Figure 4.5.

1. The Ferrule:

The optical fibers are not actually mounted directly in the connector, but instead are precisely aligned and mounted into an intermediary part called a ferrule. In many connectors, the ferrule comprises a long, thin cylinder of ceramic with a hole through the center slightly larger than the diameter of the fiber cladding. In most existing multi-fiber ribbon connectors, a plastic rectangular ferrule is used. The most common, the MT ferrule, is a compression or transfer molded thermoset polymer with a series of twelve holes for the fibers and two holes for alignment pins. In most cases, the fiber is installed in the ferrule and then polished so that the fiber is coincident or slightly protruding off the end of the ferrule. The fiber-to-ferrule interface is the first location in the connector where error can be introduced.

2. Alignment Device:


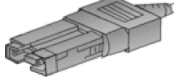
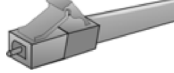

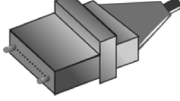
The second part in a connector is the alignment device which is the part that mates two connectors and defines the location of one ferrule with respect to another. In cylindrical connectors, the alignment device generally consists of a sleeve which slides over the ends of two ferrules and constrains their relative motions. For the MT ferrule, alignment and mating occurs using two precision pins fit into highly toleranced holes in the ferrule.

3. The Connector Body or Housing:

The connector body is a sub-assembly consisting of multiple metal or plastic pieces which holds the ferrule and cable. The exact design and features of the connector body varies drastically from model to model, although common features include applying preload, providing strain relief, providing a load bearing interface between connectors, and attachment locations for cable strength members and cable jackets. The connector body may sometimes have an additional component called a coupler which is used to connect two cables together. The coupler typically has no alignment function and is used solely for connection strength.

As mentioned previously, lateral and angular alignment are crucial elements of a connector and the connectors are typically the largest source of error in a fiber optic systems. In the past, connector systems were difficult to use until manufacturers standardized and simplified their designs. In the multitude of different fiber optic connectors available, most variation is present in the connector body, while the ferrule designs remain relatively standard. Table 4.2 shows loss characteristics and sketches of a selection of the more common connector types [32]

TABLE 4.2 Common Forms of Commercial Connectors (SM is single mode and MM is multimode)

Connector Name	FC	FDDI	LC	ST	MT or MT-RJ
Picture					
Insertion Loss	0.50-1.00 dB	0.20-0.70 dB	0.15 dB (SM) 0.10 dB (MM)	0.40 dB (SM) 0.50 dB (MM)	0.30-1.00 dB
Repeatability	0.20 dB	0.20 dB	0.20 dB	0.40 dB (SM) 0.20 dB (MM)	0.25 dB
Application	Data and telephone communications	Fiber Optic Network (obsolete)	High Density Interconnection	Inter-/Intra-Building, Security, Navy	High Density Interconnection

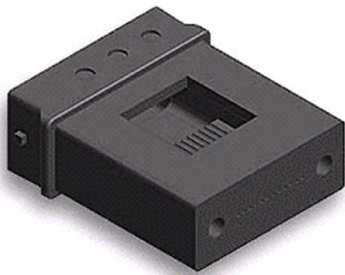


Figure 4.6 The MT Connector Ferrule

For this research, the MT array ferrule was targeted for redesign. The MT ferrule is one of the most common connector types and is available from a number of manufacturers. While the MT connector system is one of the few ferrules that aligns multiple fibers simultaneously, it has been difficult for the design to scale up to allow for a large number of fibers. Existing scaled design stack multiple rows of fibers in one connector with moderate success [33]. Also, a completed MT ferrule is too expensive for large scale distribution in fiber-to-the-door plans.

4.3 New Connector Design

In the new design, elastic averaging techniques are applied to two separate hexagonal connector ferrules containing a row of fibers. As shown in Figure 4.7, the hexagonal ferrules are formed by joining two injection molded trapezoidal halves containing a number of V-groove features. The use of KOH etched features in silicon mold tools will enable the angled part features to be precisely controlled. Before joining, the fibers are placed in the grooves of one trapezoidal ferrule half. The second ferrule half is aligned to the first using elastic deformation of each groove-cylinder interface, averaged across the set of grooves.

The optimal number of grooves is a balance between the increase in repeatability between the ferrule halves and the decrease in the accuracy of ferrule alignment due to a large number of contacts. As the number of fibers increases, sine errors about the center of stiffness cause misalignment between fibers in separate ferrules.

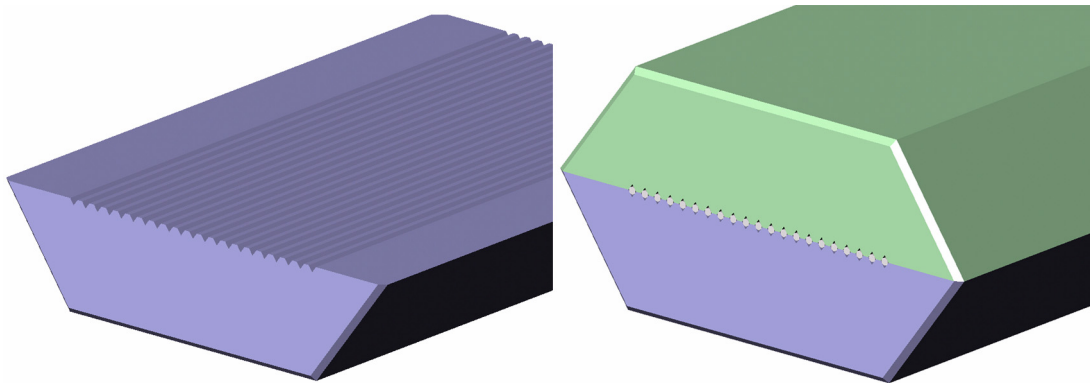


Figure 4.7 - Trapezoidal half showing grooves (top) and Joined hexagon element with 21 cylinders laid in V-grooves (bottom)

Two separate connector ferrules are subsequently aligned using a separate sleeve element employing elastic averaging in a circular fashion. This sleeve combines the functions of the alignment device with preload and some structural functions of the coupling body. In summary, the sleeve is a series of 12 line contacts located around a thin circular metal extrusion. During assembly, each of the side surfaces on the hexagonal ferrules will connect with two of these bumps, causing the metal sleeve to deform elastically in the radial direction. To maintain contact between the two ferrules, beam springs are formed into the

sleeve to provide a preload force along the axis of the sleeve. In Figure 2, the springs are shown as fixed-free cantilever beams but can also be realized as simply supported beams.

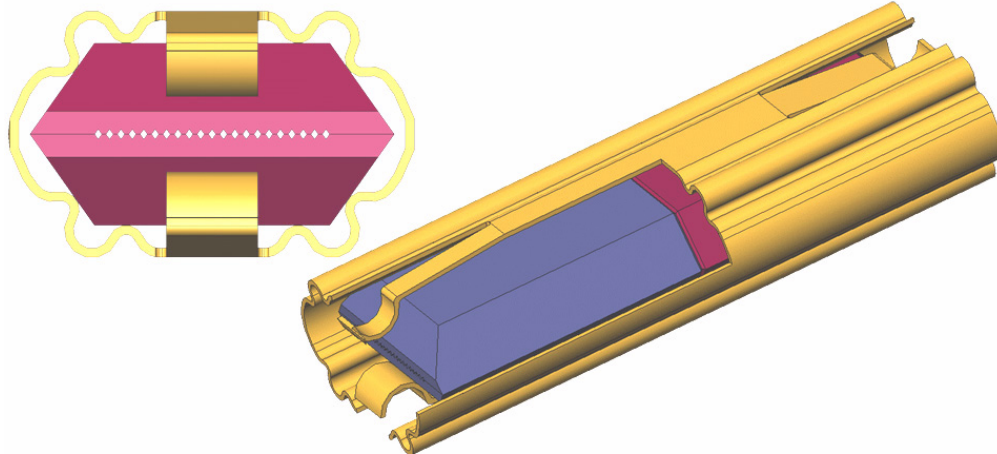


Figure 4.8 - Two connector elements shown mated inside sleeve - end view (left) and isometric view with cutout showing preload beam (right)

4.4 Large Scale Connector Simulations

To apply elastic averaging to the connector design, a 5X scale version was used for design and experiments. The ferrule was chosen to be commercially available plastic, either nylon or HDPE, in a hexagonal shape with a 1 inch dimension from a flat to an opposing flat. The alignment sleeve was intended to be one millimeter thick aluminum extrusion produced with an initial press fit between the sleeve and hexagonal ferrule of approximately $25\mu\text{m}$. However, the commercially obtained custom extrusion used in experiments could only be obtained with a 2 millimeter thickness, with tolerances of 0.001 inches on all dimensions. The finite element simulations and resulting stiffness equations were capable of predicting the stiffness variation for this change and the subsequent repeatability analysis was performed using the obtained dimensions and tolerances.

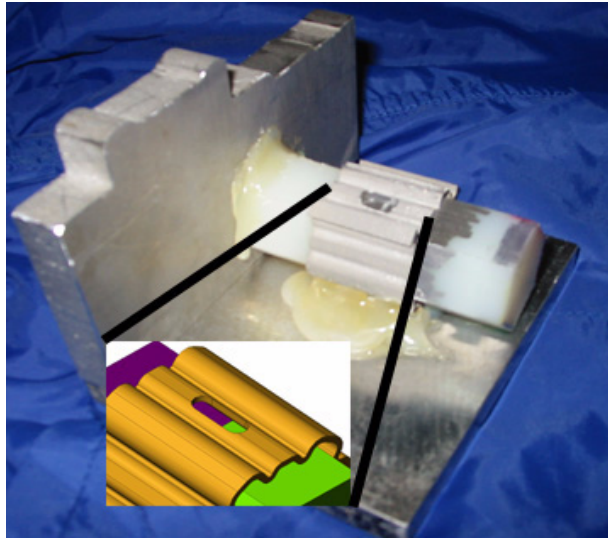


Figure 4.9 - Bench-level experimental setup including a waterjet aluminum sleeve and a Delrin ferrule

Initial large-scale bench-level models of the connector were created using approximately 1mm thick waterjet aluminum for the sleeve and a 1-inch wide Delrin hexagonal rod for the ferrules. These models were joined, then measured using a white light profilometer to determine the repeatability of the height difference between the two ferrules. As white Delrin is difficult to measure using a profilometer, small silicon targets were glued to the plastic. Figure 4.9 illustrates the test setup for this experiment. Results with this fairly basic model show that the standard deviation of the height difference is approximately 5 micrometers and the angular difference is 0.03 degrees. Complete results for 20 trials are shown in Figure 4.10. However, baseline repeatability of the measurement system is on the same order as these results, indicating that the models should be more repeatable. The main source of measurement error is the motion of the x-y stage when traveling between the two targets.

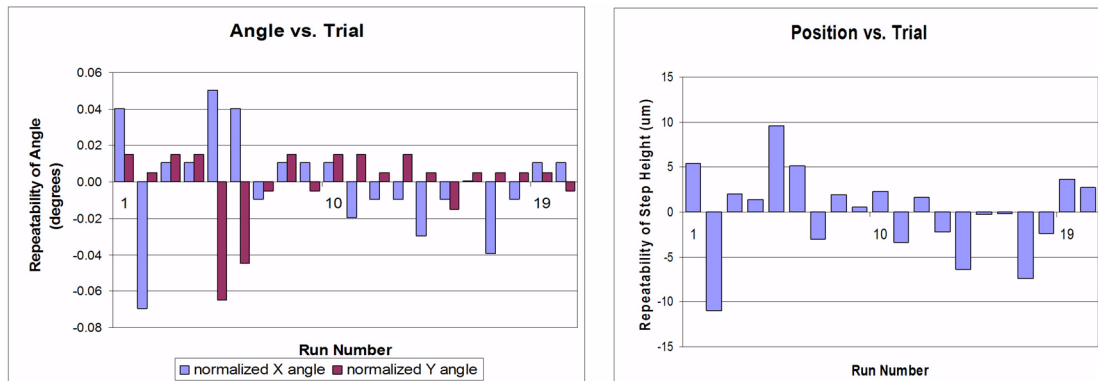


Figure 4.10 - Angle vs. Trial and Position vs. Trial result for large-scale model of assembly

4.4.1 Elastic Averaging Model Application

Using the elastic averaging model, the repeatability of the connector due to manufacturing variation can now be predicted.

Step 1 - Build a model of the flexible elements in the coupling.

Due to the complex geometry of the alignment sleeve, a closed form model of the geometry was not attempted and FEA modeling was used. A model of the connector was built using the IDEAS NX 11 computer aided engineering software from UGS. The FEA model used a mapped mesh of quadrilateral elements to represent the sleeve geometry. Since the geometry is symmetric, the FEA model would typically be divided into a quarter model with symmetry boundary conditions to simplify the solution. However, initial simulations comparing a quarter and full model demonstrated that the cross coupling effect between contacts around the sleeve were significant enough to warrant using a full model of the geometry for detailed stiffness analysis. Material properties for 6061-T6 Aluminum were specified in the model and several different boundary conditions strategies were used, depending on the analysis performed.

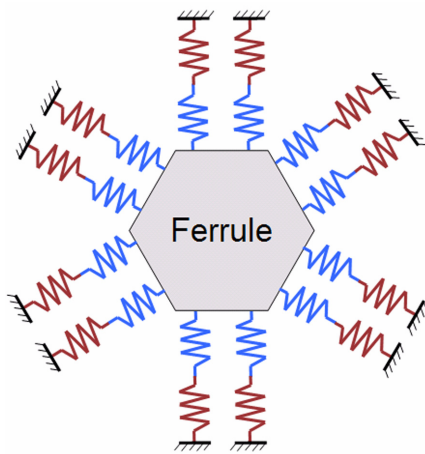


Figure 4.11 - Equivalent spring model of ferrule-sleeve interface

In order to model the behavior of the ferrule-sleeve interface, each contact point between the two parts is replaced by a number of springs. Each contact point consists of two springs in series - one to represent the elastic behavior of the sleeve geometry and one to represent a simplified stiffness model for Hertzian contact stiffness. When the connector is assembled, the springs all act in parallel to center the ferrule. Tolerances are applied to the model by effectively changing the location of the ground.

Step 2 - Determine sensitivity of dimensional parameters to tolerances.

To determine the sensitive geometric parameters, a simple quarter model mesh was applied to the model. Symmetric boundary constraints were applied to the split surfaces and force boundary conditions were used to simulate the interaction between the sleeve and contact. After probing several different dimensions, the list of sensitive parameters was limited to five parameters - thickness, gap, contact radius, arm length, and blend radius, as shown in Figure 4.12. The solver also produced a relative scaling for parameter sensitivity indicating that the thickness and gap are the most dominant parameters, with arm length, contact radius and blend radius in order of decreasing importance.

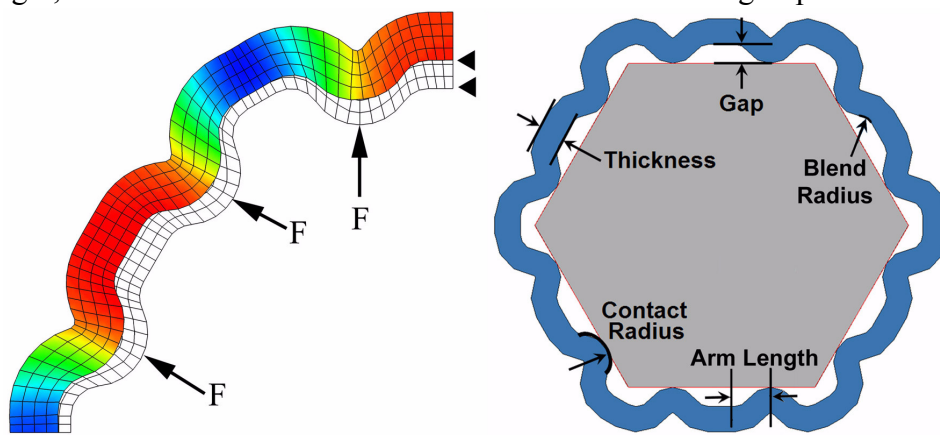


Figure 4.12 - Quarter FEA Model for Sensitivity Analysis (Left) and Critical Parameter Schematic (right)

Step 3 - Create a parameterized stiffness equation to predict the stiffness due to changes in the sensitive parameters.

Based on the results from the simple quarter model, a series of FEA experiments were performed to create a parameterized stiffness equation for the stiffness of each contact point. Instead of using the quarter model, the full cross section of the sleeve was meshed and used in the analysis. Displacement constraints could not be placed on the model to properly restrict free motion and allow forces to be applied, so displacement constraints were used to constrain the model and simulate the press-fit action. Resulting reaction forces could be measured to determine stiffness. Local coordinate systems were created at each contact point and outwards facing displacements constraints were applied at each point. Two different displacements were used, 1 μ m to easily calculate unit stiffness and 26 μ m to simulate the press-fit present in the bench level experiments. Example plots and details on the FEA model are available in Appendix A. To create a curve fit for the stiffness equation, simulations were performed with approximately 100 different variations of the five parameters within a range of 50% of the nominal value. Displacements and reaction forces at each contact probe were recorded, then analyzed to create a logarithmic curve fit in Excel. The curve fitting algorithm in Excel accepted rows of data from one simulation in an array format and outputs a product of exponential factors raised to the power of the dimension's value in millimeters. Since this initial curve fit was not sufficient to accurately predict stiffness, additional squared and cubed terms were added based on the sensitivity of the particular parameter. The variable form of this relationship is shown in Equation 4.5, with the exact values of the constants presented in Appendix C. While this may not be the most efficient method for curve fitting such a set of parameters, the speed of analysis was fast and the accuracy of the solution was sufficient for a number of extrapolated and interpolated data points, with no predicted value deviating more than 5% from the FEA value.

$$K = C \cdot (C_{t1}^t \cdot C_{t2}^{t^2} \cdot C_{t3}^{t^3})(C_{g1}^g \cdot C_{g2}^{g^2} \cdot C_{g3}^{g^3})(C_{rc1}^{rc} \cdot C_{rc2}^{rc^2})(C_{L1}^L \cdot C_{L2}^{L^2})(C_{rb1}^{rb} \cdot C_{rb2}^{rb^2}) \quad (4.5)$$

Stiffness plots and stiffness sensitivity plots were then created using this equation. Detailed plots are also shown in Appendix A, although summary plots for the stiffness versus one varying dimension with other dimensions at the nominal value are presented in Figure 4.13.

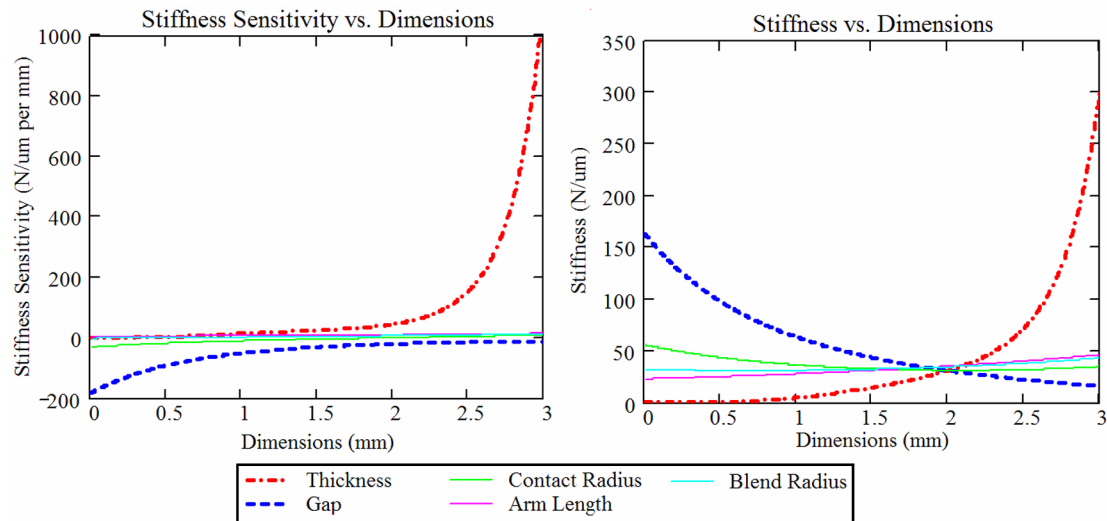


Figure 4.13 - Stiffness Sensitivity (left) and Stiffness (right) Plots for Critical Parameters. Horizontal axis is the value for the dimension listed in the legend.

In these two plots, the stiffness sensitivity trends noted previously were confirmed as the thickness and gap parameters had a much more significant effect on stiffness. As intuition would predict, the stiffness of the sleeve increases with increasing thickness. There is a noticeable increase in stiffness for a thickness greater than approximately 2mm, which is due to a change in the geometry from a thin, serpentine geometry into a thicker hexagonal shape with bumps on the inside surface. Several additional data points were taken in this region to confirm accurate stiffness prediction. The gap parameter shows a similar effect for small dimensions, although stiffness decreases with increasing dimension. In these plots, contact radius appears to have little effect on the stiffness. While this conclusion is correct for geometric behavior, the addition of Hertzian contact stiffness increases the importance of this parameter. Contact stiffness for the nominal dimensions is an order of magnitude greater than the geometric stiffness, indicating that the majority of elastic motion takes place through deflection of the sleeve.

By combining geometric stiffness with Hertzian contact stiffness and friction, the axial removal force for the nominal press-fit dimension can be calculated. A simple verification test using the prototype shown in Figure 4.9 matches the predicted removal force to within 2%. These forces can then be used to determine the required geometric and material parameters for the preload beams shown in Figure 4.8. The detailed mathematics for the preload beam are included in Appendix D.

Step 4 - Map the effect of cross coupling of contact points.

Due to cross coupling between the different contact points, the stiffness relationship in Equation 4.5 only provides the nominal stiffness value for each contact point. Any change in the force or displacement from the nominal will change the equivalent force or displacement at neighboring contacts. Therefore, the full stiffness equation is modeled as two parts shown in Equation 4.6.

$$F = K_{uncoupled} \cdot \delta_{pressfit} + K_{coupled} \cdot C_{displacement} \cdot \delta_{tolerances} \quad (4.6)$$

This equation correlates to the process used to map the stiffness in FEA. The uncoupled stiffness matrix is mapped using the press-fit deflection at each contact point, while the coupled stiffness is found by deflecting only one point by a micron and measuring the forces and deflections at other contact points. The coupled stiffness from FEA results in a combination of the K and C matrices shown in Equation 4.6. The coupled and uncoupled behaviors can then be superimposed to provide the complete force state in the coupling.

When creating the FEA model for the coupled case, the boundary conditions used for the uncoupled case no longer apply. Since the previous boundary conditions consist of fixed displacement constraints at each contact, a change at one contact would be seen only as a change in force at the other contact points. This behavior ignores the displacement coupling between neighboring contact points. If the deflection at one point exceeds the initial press fit, that contact point will lose contact as the point lifts off the ferrule surface. The lift off will affect the contact point on the same flat surface of the hexagon, causing it to also lift off by a significantly reduced amount. The other contact points around the sleeve

will slide along the ferrule to accommodate this motion until some value is reached where other neighbors will also lose contact. Fortunately, the connector design will not see this motion except for small initial press fits and exceptionally large errors beyond reasonable tolerances for this design. Because the displacement coupling is very light, the qualitative constraint metric indicates that this coupling is elastic averaging.

To model the realistic behavior of the sleeve, the fixed displacement constraints are replaced with gap elements. Gap elements are similar to contact elements, as the solver will calculate reaction forces when deflection occurs into the contacting surface and displacements when the deflections separate the contacting surfaces. However, the gap elements do not accurately model contact stress as all forces and displacements are applied to the node connecting the mesh to the gap element. If a large deflection is applied through the gap element, the connecting node can deform relative to neighboring nodes, creating an excessively high, imaginary stress condition. Contact elements would also affect the neighboring elements, causing neighboring nodes to also deflect and form a contact patch. However, contact solutions in IDEAS and most solvers require full 3D meshes rather than the simplified planar meshes used here. Because of this limitation, only small displacements can be applied using gap elements, which is acceptable for this linear case study.

Inside the property tables for each gap element, an initial displacement can be specified to model the starting location of the contact points. If these displacements are negative, the solver will interpret that the geometry is in a “press-fit” condition and first deflect the geometry to a zero configuration before applying boundary conditions. Without any error motions, the gap element model with just the press fit matches the previous constraint only simulation within the solver’s accuracy. To solve for the error motions, the gap elements were set to have zero initial displacement. One contact point can then be displaced with the same result using either force or position boundary conditions, or by specifying a positive displacement in a separate gap element for that contact.

Initially, the FEA results for the sleeve exhibited a somewhat strange displacement behavior where the contact points far away from the deflected point exhibited deflection before neighboring points. Several FEA verification trials were performed to examine this behavior. The first test was to verify that the gap element was accurately expressing the expected force deflection relationship for contact. A simple FEA model was constructed consisting of a square bar placed under axial compression and tension by a gap element. The results from this model matched expected values using traditional mechanics calculations.

Another possible reason for the strange behavior was thought to be due to the ability of the contact points to slide along the sides of the hexagon. To verify this behavior, a circular hoop was modeled with similar boundary conditions and gap elements. When put under a small error motion at one point, a similar behavior of slip along the hexagon and unexpected displacements was noticed. A final model was created with the basic interior shape of the sleeve, but with an extremely thick, circular outer dimension to model the sleeve as extremely stiff. When similar boundary conditions and gap elements were applied, similar behavior was seen, although there was less slip between the two surfaces. This relative displacement was replaced with much higher stress in the sleeve and excessive, extraneous deflection of the contacts. After more investigation, the strange behavior was discovered to be smaller than the accuracy of the 32-bit solver, indicating that the behavior is not actually occurring. To accurately describe the displacement coupling, a deflection slightly larger than the press fit was required and this relationship was assumed to scale down below the press fit dimension. Examples of the FEA models used in this case study in Appendix A.

Step 5 - Form local stiffness matrices for each contact point and merge to form a global stiffness matrix for the system.

This step is fairly algorithmic for this connector design. The contact points are numbered from 1 to 12 in clockwise manor, with the top right contact as contact 1. Each contact point is located by an angle β , which defines the perpendicular bisector of each hexagonal

flat, and by an angle α , which defines the location of the contact on the flat with respect to the bisector. The local x-direction is specified normal to the flat, while the local y-direction is parallel to the flat. In global coordinates, the x-direction is defined parallel to one flat containing contact points 12 and 1, while the global y-direction corresponds to the perpendicular bisector of the same flat. Homogeneous transformation matrices were formed to convert the local coordinates to global coordinates.

Step 6 - Combine force and moment equilibrium conditions with geometric constraint equations.

In global coordinates, there are two force equilibrium equations, one for each of the global coordinates, and one moment equilibrium equation taken about the ferrule center. Due to the symmetry of the sleeve, the error motion of the ferrule is restricted to only three degrees of freedom, the two translations and one rotation, and the equilibrium equations can be solved for the position. Essentially, the final location of each spring is grounded on the ferrule, so the displacement of each spring in each direction is the same.

Step 7 - Find deflections, forces, and other engineering quantities.

Using the above described model, the repeatability of the connector can be determined by repeatedly solving the model with randomly generated errors on each dimension within specified tolerances. The standard deviation for location in both directions is predicted to be $1.73\mu\text{m}$ for the nominal sleeve geometry with tolerances of $25\mu\text{m}$ on each dimension. Angular standard deviation is also predicted to be 0.26 degrees. If a sufficiently large number (>2500) of data points are collected, the mean of the data becomes approximately zero. The repeatability analysis is also performed with tolerances of $50\mu\text{m}$ and $12\mu\text{m}$, which predicts output standard deviations of $3.63\mu\text{m}$ and $0.92\mu\text{m}$ respectively. Comparing these three values to the repeatability suggested by the $1/n^{1/2}$ trend indicates that the trend is more conservative than the analysis predicts, with trend repeatabilities of $1.16\mu\text{m}$, $2.41\mu\text{m}$, and $4.81\mu\text{m}$ in order of increasing tolerance. For a 1X scaled down version, standard deviation is predicted to be approximately $0.096\mu\text{m}$ by the trend with tolerances of $1\mu\text{m}$, while analysis indicates that the standard deviation should be $0.069\mu\text{m}$.

TABLE 4.3 Standard Deviation from Simulations and Elastic Averaging Trend for 5X and 1X Models (All tolerances and results in μm)

Scale	Sensitive Tolerances	Standard Deviation from Simulations	Standard Deviation from $1/n^{1/2}$ Trend
5X	12	0.92	1.16
	25	1.73	2.41
	50	3.63	4.81
1X	1	0.09	0.07

Similar to the sensitivity data generated for stiffness, repeatability data was generated with variations of the five primary dimensional parameters. The repeatability trends mirrored the stiffness trends, with the arm length and blend radius parameters having very little effect on repeatability. Increasing thickness by $\pm 25\%$ worsened the repeatability by 5-10%, while increasing the gap improved the repeatability by the same amount. Increases in the contact radius improved repeatability by less than 5%, while the other parameters' effect was negligible.

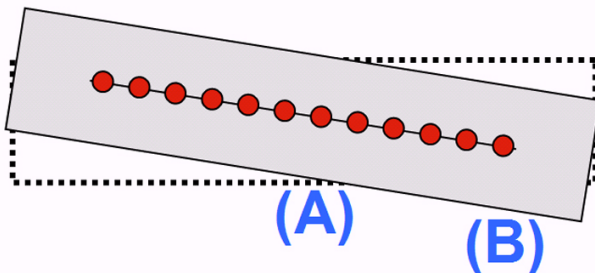


Figure 4.14 - Error calculation locations for power loss

By assuming that two ferrules are connected with the worst case position errors (three times the standard deviation for x, y, and angle), optical power loss can be calculated using the relationships in Equation 4.3 and Equation 4.4. The lateral error can be calculated using a combination of the x and y errors, plus the sine error cause by tilt of the ferrule and manufacturing uncertainty of each groove location. Angular error can be estimated by assuming one end of the ferrule will move by the given x and y errors while the other end has the same errors in the opposite direction. For the 5X scale version of the connector, the worst case possible power loss due solely to manufacturing variation at the connector center is 0.70dB, although loss increases to 5dB as little as 5mm away from the center. The actual scale connector is predicted to have loss of 0.11dB at the connector center (point A in Figure 4.14) and 0.20dB at the furthest away fiber position (point B in Figure 4.14), assuming a fiber spacing com-

parable to the MT ferrule. However, since this model does not account for random errors due to effects such as environmental contaminants, friction, wear-in, etc., the repeatability and power loss listed here are the best possible values for the worst possible combination of dimensions. Based solely on these estimates, the SIMP connector design is comparable to the MT ferrule in optical performance.

Systematic Errors

While the elastically averaged coupling successfully improves accuracy due to random errors, it remains susceptible to systematic errors. For example, the accuracy of the SIMP created grooves in the ferrule were experimentally determined to be between 1 and 5 μm . The elastically averaged design would reduce the effect of this error when aligning two ferrules; however, a fiber placed in the ferrule would still be subject to the errors in the location of the groove, regardless of the connector design. This error could be minimized by keying or marking the ferrules so they are assembled in a configuration that consistently aligns the grooves with similarly offset grooves.

Similarly, the elastically averaged design can compensate for random errors at each contact point, but cannot correct a systematic error such as an localized change in sleeve thickness consistent across a number of parts. In this case, the ferrules aligned using that sleeve would exhibit an offset due to the sleeve's local change in stiffness and the displacement of the contacts points. The repeatability and interchangeability of the coupling remains the same as any two ferrules joined using the sleeve would be displaced by an equivalent amount, assuming the thickness change is minimal along the length of the sleeve. Only the accuracy of the coupling with respect to the nominal zero point would be affected, which is unimportant for any two coupled ferrules. An interesting effect in this case is the possibility of the elastically averaged coupling becoming an almost exactly constrained design. If the stiffness of three contacts were to become much larger than other contacts, the stiff contacts would define the location of the coupling while the compliant contacts would serve simply as preload.

4.5 Experiments

In addition to the previously mentioned 5X scale bench level experiments, additional experiments were performed to help assess the accuracy of the coupling using a small number of samples. Without measuring a large number of samples, the full repeatability of the coupling cannot be measured experimentally. Instead, a sample of three ferrules and sleeves were measured to determine the actual combination of dimensional parameters. The hexagonal ferrules could be measured easily using a micrometer to find the samples' actual width from flat to flat. To measure the sleeve, a small sample was sectioned and measured using an optical comparator and the Zygo white light interferometer. Since it was necessary to move the x-y table in the interferometer, the accuracy of the measurements were valid only to 5 μ m. These dimensions were then used in the elastic averaging model without the randomly distributed tolerances in order to predict the displaced position. For example, the aluminum sleeve on a brass ferrule was predicted to have a position offset of 0.1 μ m. While initially plastic ferrules were to be used, obtaining an accurately machined fit was difficult due to instability of the polymer during machining. Brass and magnesium hexagonal ferrules were used instead to allow for more stable manufacturing dimensions. This problem would not be present for the actual scale connector as the parts will be molded whole and not machined.

To experimentally determine the location of the ferrule, a test setup was built using capacitance probes to measure the location of the sleeve with respect to the ferrule. This system, shown in Figure 4.15, consists of a series of 0.5 inch thick aluminum plates mounted onto a 1 inch thick aluminum base plate. The vertical plate contains a hole threaded to accept a 3/8 inch diameter bolt which passes through a clearance hole in the center of the ferrule. A 1/4 inch hole on each side of the ferrule allows pins to connect to a removal plate. On the other side of the vertical plate, these pins butt up against the free moving aluminum plate labelled removal stage in Figure 4.15. To remove the ferrule, a 1/4-20 bolt threaded into a plate on the base is rotated using a power drill. As the bolt turns, it pushes against the removal stage, which transfers the force through the pins to the removal plate and the

sleeve. A similar system was mirrored on the right side of the figure to assist in repeatably pressing the sleeve onto the ferrule. This elaborate scheme was not necessary in the preliminary 1mm thick waterjet model, but is required for the 2mm thick extrusion due to the geometry's increased stiffness and increased frictional force. Attached to the vertical plate

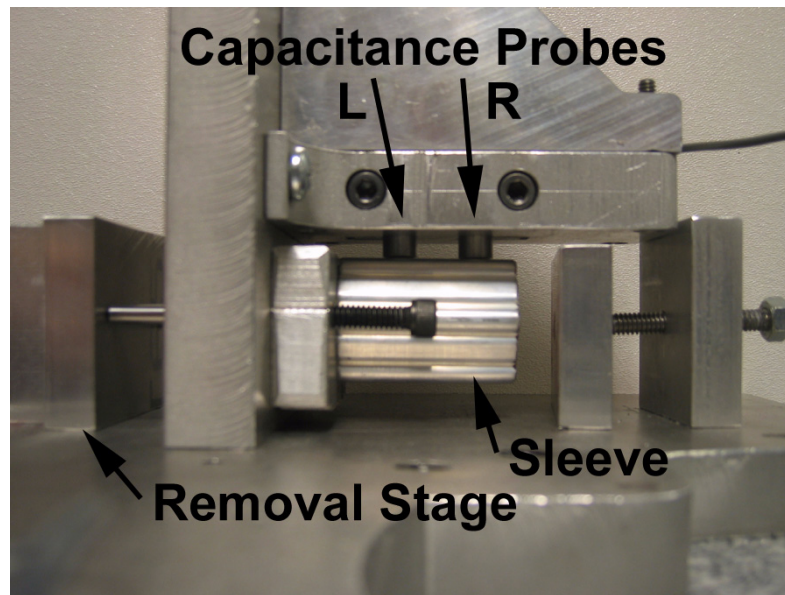


Figure 4.15 - Capacitance Probe Measurement System - Sleeve mounted on Ferrule.

is a 0.5 inch thick horizontal aluminum plate extending above the ferrule and sleeve. This plate contains two flexures designed to securely hold the Lion Precision capacitance probes above the sleeve. Each capacitance probe was operated in high resolution mode, allowing for a resolution of 3.5 nm RMS over a span of 75 to 125 μm between the probe tip and part surface. All measurements were controlled and recorded automatically using LabView with a National Instruments E-Series 16-bit DAQ Card, which has a resolution of 152 μV or an equivalent measurement resolution of 0.5 nm. Using this setup, the sleeve-ferrule combination with a predicted 0.1 μm position offset from the simulation was measured to have an offset of 0.07 μm . Using the same measurement system and ferrule-sleeve combination, a standard deviation for position of 1.08 μm was obtained. The other ferrule-sleeve combinations had similarly accurate correlations between the simulated and measured positions, as well as negligibly different standard deviations. This result indicates that the repeatability of the connector design due to random assembly variances

(assembly repeatability) is on the same order as random manufacturing variances (interchangeability). Therefore, repeatability and interchangeability could be easily combined in the analysis to quasi-deterministically determine their effect.

Chapter 5

PRECISION INJECTION MOLDING OF FIDELITY PARTS

5.1 Introduction to Precision Molding

As the demand for smaller and smaller devices continues to increase, current manufacturing processes will find it more challenging to meet cost, quantity, and dimensional requirements. While microfabrication technology processes can create electronic devices in vast quantities with increasingly smaller dimensions, they are challenged to do so for mechanical devices at low cost and in large quantity. More traditional manufacturing processes such as machining or plastic injection molding can more easily meet cost and quantity requirements, but cannot currently match the dimensional abilities of microfabrication processes. By merging microfabrication and traditional injection molding techniques, the benefits of both technologies can be combined to produce parts to meet all three requirements. Newer polymer processes such as hot embossing and LIGA (X-ray lithography, electroplating, and molding processes) are currently being developed to improve the resolution of some polymer parts. However, these processes suffer from expensive preprocessing and are limited to vertical-wall geometries. Accordingly, one of the objectives of this thesis is to investigate the possibilities of injection molding polymer parts with sub-micron three-dimensional features, such as angled planes, using a process called *Silicon Insert Molded Plastics* (SIMP).

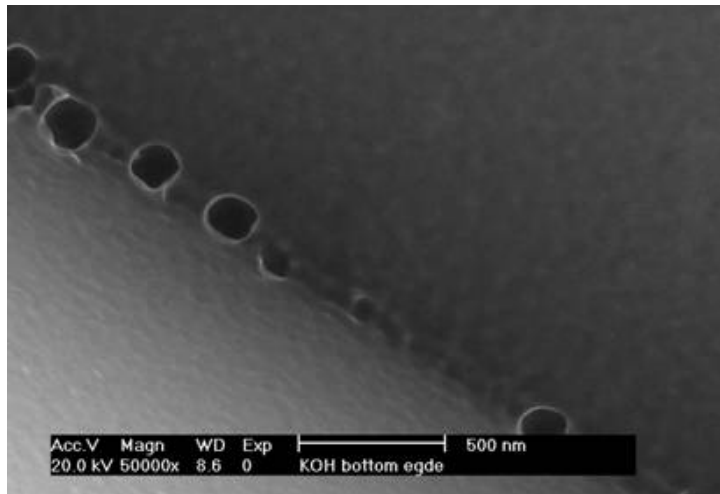


Figure 5.1 - SEM of KOH etched features in Silicon (500 nm scale)

Using traditional mold making processes, molds can be manufactured which allow for parts with features on the order of several microns. However, many medical, technical and consumer applications demand higher precision than the traditional techniques of injection molding can provide. To improve precision molding beyond the current limits, it is proposed that silicon inserts be placed inside the mold cavity. The silicon inserts would be manufactured using microfabrication techniques allowing for tolerances, smoothness, and dimensions at a nanoscale level. For example, silicon can be selectively etched using KOH to obtain nanometer smooth $\langle 111 \rangle$ planes at an inclination angle of 54.7 degrees from the wafer plane. Figure 3.1 shows the intersection of an etched $\langle 111 \rangle$ plane with the polished plane of the wafer, and it can be seen that both planes have nanometer smoothness, while the edge between them has 30-50 nm straightness. These features were obtained without any particular attention to the precision, therefore this research will seek to improve the precision of the edge straightness. Using these types of basic primitive features, more complex structures can be formed by bonding several sections of silicon to also include temperature control passages. This structure can then be interfaced to a traditional mold created using traditional machining operations and electro-discharge machining (EDM). By constraining the precise features within the silicon insert, parts can easily

transition between highly accurate regions and less precise regions, lowering the costs of manufacturing parts with combined meso and nanoscale features.

The details in the rest of this chapter cover some of the work done on SIMP as it relates to developing tool inserts for manufacturing the fiber optic connector. A discussion of silicon fabrication processes related to SIMP are available in Jaime Werkmeister's Engineer's Degree Thesis from MIT [34].

5.2 Review of Existing Technologies

In commercial operation, traditional mold manufacturing techniques are capable of producing parts with minimum wall thicknesses of $400\mu\text{m}$ and maximum part sizes of around one inch. These techniques can generally provide tolerances of approximately $\pm 130\mu\text{m}$ [35]. Traditional mold making techniques typically consist of casting processes, machining operations, and high precision grinding and polishing processes. State of the art commercial molding technology is micro-injection molding, where parts typically are in the range of less than 100 mg with critical dimensions of less than 1mm. Micro-injection molds can provide tolerances of less than $\pm 1\mu\text{m}$ to $\pm 50\mu\text{m}$ for such parts, depending on material [36]. In order to achieve these precision molds, mold makers employ a combination of traditional machining operations with electroforming and EDM. Wire EDM can provide $100\mu\text{m}$ surface roughness and approximately 400nm tolerances under best conditions. For applications requiring extremely smooth surfaces, EDM combined with lapping or polishing can create surfaces with $0.1\mu\text{m}$ - $1\mu\text{m}$ surface roughness [37]. Precision manufactured molds can be integrated into almost any standard injection molding machine to create reasonably accurate parts. For example, compact discs are micro-injection molded to have features of $3\mu\text{m}$ by $0.5\mu\text{m}$ with spacings of $1.6\mu\text{m}$ apart [38]. However, highly accurate parts require additional consideration in the design and control of the machine and process. Most industrial machines can apply large forces onto large mold bases and use large injection screws to supply large quantities of plastic quickly. Newer, small scale machines such as the Sesame Nanomolding machine [39] employ short injection strokes

and smaller screws to apply small shot sizes of polymer at higher pressures. In addition, hot runners are used to keep the non-part material in the mold from freezing.

While these machines and techniques can produce features on the micron scale, they have difficulty extending part capabilities into the nanoscale. Instead, researchers have turned to microfabrication processes such as lithography and etching to investigate new molding techniques. Many of these techniques have been directed towards developing soft lithographic processes, which allow for microfabrication of semiconductor devices on a wide variety of materials without the use of photolithography [40]. These techniques tend to lend themselves to three generic groupings - light based forming, embossing, and the LIGA process.

Light based forming consists of two major forms - laser micromachining similar to the process used to write CDs [38], [41] and photomolding through light induced reaction injection molding [42]. The photomolding process requires the use of photocurable polymers which are injected using a standard injection molding machine. After injection into the mold, the filled cavity is exposed to a high intensity UV source while under pressure to cure the polymer in the molded form. While photomolding is capable of producing parts with dimensions on the order of 200nm, the molds require complex transparent sections for UV exposure and long curing times.

The next form of molding consists of a variety of embossing, printing, and replication processes for replication of features on a silicon wafer. These processes are used almost exclusively to transfer a pattern from a die to a thin polymer layer on a wafer. Subsequent processes either deposit metal then remove the polymer to create a metal part or use the polymer as a pattern for etching a wafer. The metal nano-replication process is capable of reproducing dimensions of 25nm in both PMMA and aluminium [43]. Investigations into nano-imprint lithography have produced features with 10nm diameter pillars with 60nm spacing after reactive ion etching (RIE) [44] and 40nm features in PMMA layers which transfer to 100nm silicon features after RIE using house-made equipment [45]. While

these processes are capable of producing nanoscale features, they typically cannot produce complex three dimensional geometries, but rather produce high aspect ratio planar features in silicon. One company, Thermo RGL, uses an epoxy based replication procedure to create optical gratings with critical dimensions of 170nm [46]. 3M currently uses a silicon based tool to replicate v-grooves for their Volition series of connectors.

The final form of microfabrication techniques applied for injection molding is the LIGA process. LIGA is a German acronym for a process where lithography, electroplating, and injection molding are combined to create plastic parts. The LIGA process uses x-ray lithography to develop a thin layer of photoresist, which is used as a base for electroplating the complex geometry of the part [47], [48]. This metal structure can be removed and used as a part or as a mold for creating additional parts with dimensions of 1 μ m to 10 μ m [49]. In experiments using LIGA formed structures as casting molds for PDMS, researchers created high aspect ratio microstructures on the metal mold inserts with surface roughness of 204nm, which yielded roughness of 215nm when replicated into PDMS [50]. The casting process used by the researchers was to spin the PDMS on the LIGA formed structures to obtain a uniform layer, then to vacuum degass and cure the polymer in an oven [51]. In addition to the casting procedure, LIGA molds have found application in injection molds. However, LIGA mold geometries are also restricted to high aspect ratio two dimensional microstructures. Cost restrictions are also a concern with LIGA, primarily due to the high cost of x-ray lithography and multiple steps require to fabricate the mold. A typical LIGA mold produced at Sandia National Labs costs approximately \$10,000 for a single 3- or 4-inch diameter wafer, [47].

5.3 The Silicon Insert Molded Plastics (SIMP) Process

As discussed previously, many of the current methods of injection molding or precisely forming polymer parts lack sufficient dimensional capability to produce three dimensional nanoscale features at a low cost. The SIMP process combines intelligent use of microfabrication processes to create silicon molds with nanoscale features and surface roughness.

In order to create nanoscale features without high energy lithography, different fabrication procedures will be required, for example, KOH etching. KOH etching is unique as the etching process occurs more quickly along the $\langle 100 \rangle$ direction than along the $\{111\}$ planes in silicon, creating angles of 54.7 degrees along the $\{111\}$ planes [52]. This anisotropic etch creates nanometer smooth surfaces along the etched planes. Due to short etch times, KOH can create surface artifacts including jagged edges and scallops on the surface. An alternative etch chemistry is Tetramethyl Ammonium Hydroxide (TMAH), which removes material more slowly and tends to have better surface finish. Since the 54.7 degree angle may not be desired in many applications, off-axis cut wafers can be used. These wafers are cut so that the wafer plane is no longer the (100) plane, but instead some other plane such as the (113) plane. When this wafer is etched with KOH, the $\{111\}$ planes are still exposed, but the planes are at different angles with respect to the wafer surface. The (113) plane example will end up providing an approximately 30 degree tip.

By bonding an etched surface onto a flat wafer, a sharp edge can be formed with nanometer resolution. Other features can be created using high energy lithography or focused ion beam milling, if necessary. Based on the capabilities of the microfabrication processes, dimensions on the micron scale and tolerances in the nanometer to micron range should be possible in the molded parts. After the silicon mold insert is manufactured, it can be integrated into the metal mold base and the machine with attention placed on the thermal relationship between the silicon inserts and metal mold base. Precise control of mold motion and thermal profiles must be managed during the entire cycle to ensure proper filling of the part.

5.4 Research to Date

5.4.1 Edge and Surface Capabilities

To first understand the capabilities of the KOH etching process, the common razor blade was examined as a sample application for the SIMP process. Werkmeister's thesis concentrates on the development of this razor blade. Many people do not shave after showering, and thus their razors quickly dull unless they are willing to use

a new razor blade every time they shave. Based on environmental and recycling concerns, the questions was asked why molds cannot be formed accurately enough to enable single-use razor blades to be molded from plastic. The literature is packed with discussion on the use of PDMS for replication on the sub-micron level and LIGA research also abounds; however, neither of these processes are suitable for the low cost precision molding that would be required for making parts with tough precision edges such as razor blades [47] - [51]. By combining KOH etched features with wafer bonding techniques, molds can be created with nanometer smooth surfaces and a nanoscale tip as shown in Figure 5.2. The techniques described previously will be employed in this design to accurately control the thermal state of the mold as well as maintain the material's integrity.

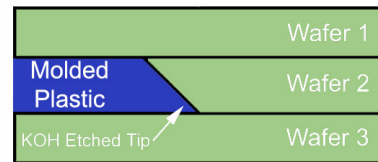


Figure 5.2 - Basic schematic of silicon mold for blade edge

The first step in understanding the razor blade was to compare the quality of the edges and surfaces available from traditional razor blades and a razor edge produced using anisotropic etching. In Figure 5.3, the edge of a traditional steel razor blade is compared with the edge created during a KOH etch. The edge of the steel blade has a tip radius of around 50-60nm, while the silicon blade tip is on the order of nanometers. In test shaves using a silicon blade, this tip dimension was actually found to be too sharp, although it is not intended that the plastic will replicate this edge.

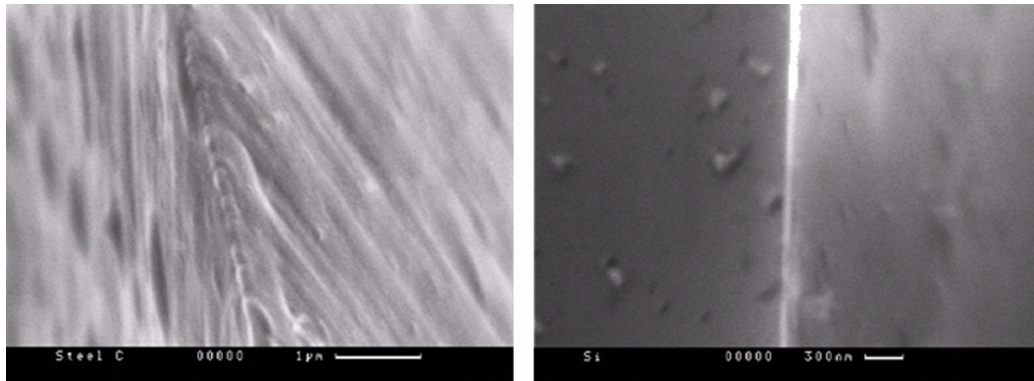


Figure 5.3 SEM photographs of conventionally ground steel razor blade tip (left - scale bar of 1 μm) and KOH etched Silicon edge (right - scale bar of 300 nm)

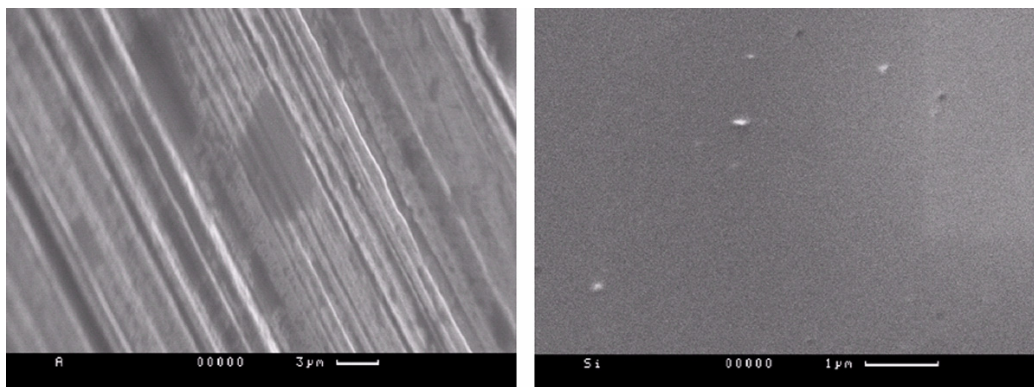


Figure 5.4 SEM photographs of conventionally ground steel razor blade surface (left - scale bar of 3 μm) and KOH etched Silicon surface (right - scale bar of 1 μm)

In Figure 5.4, the corresponding blade surfaces are shown. The steel blade exhibits noticeable grooves caused by the grinding process, while the silicon surface is atomically smooth, showing no defects over a several micron square section.

5.4.2 Mask to Wafer Alignment

During the etching trials, it was discovered that misalignment between the photolithography mask and wafer could cause surface irregularities during a anisotropic etch such as those shown in . Typically, wafer manufacturers specify that the wafer flat is cut within ± 1.0 degrees, although off-axis wafer were obtained with a tolerance closer to 2.5 degrees. Additional alignment methods were investigated to determine methods for aligning the

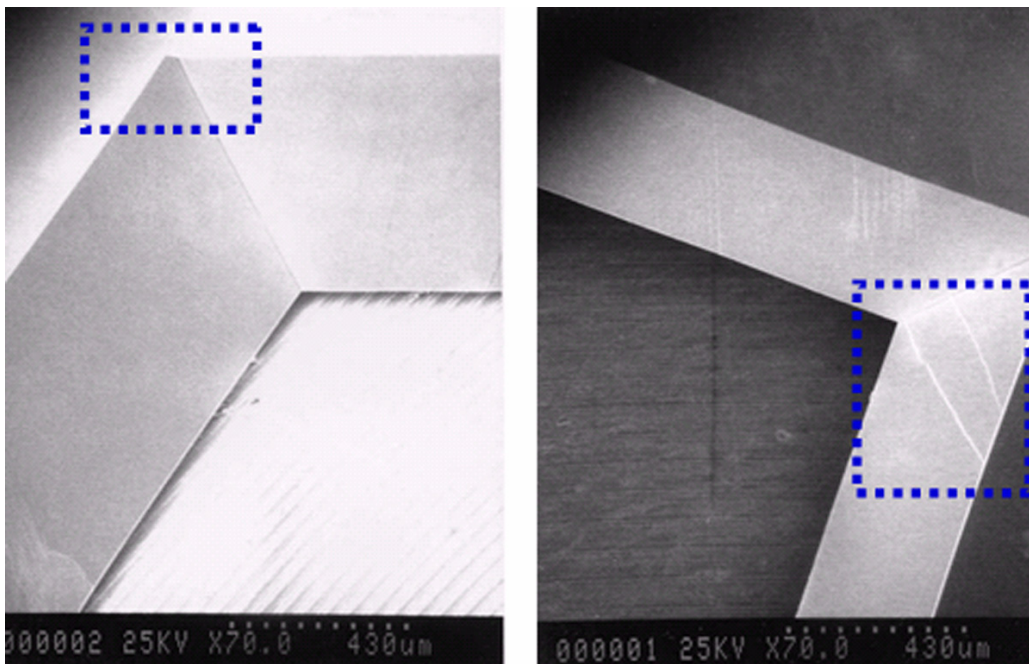


Figure 5.5 KOH Etching errors on $\langle 100 \rangle$ Silicon wafer due to mask misalignment - Edge mismatch (left) and surface terraces (right)

mask and wafer more accurately. As a result of Werkmeister, Hart, and Weber's research, it was determined that a preliminary KOH etch could be used to determine the orientation of the crystal plane more accurately than the wafer flat. Using a pattern of circles and rectangles, the test etch features can be inspected under a microscope to determine the correct orientation.

5.4.3 Backside Protection

Another processing parameter that was critical in producing the connector was protection of the wafer backside during etching. To control the etching locations on the wafer, a layer of silicon nitride is deposited and patterned. During through wafer etches, the flow of etchant and vibration of the wafer can cause the thin layer of nitride spanning the etch pit to break. When the nitride layer breaks, it tends to remove small amounts of the silicon wafer, leaving small scallop marks at the wafer tip. These features are undesirable in a final part, so a special plastic handle was used during etching to reduce the likelihood of the nitride breaking.

5.5 Preliminary Mold Trials

Using the processes outlined above, silicon wafers were processed to produce mold geometry capable of molding the connector parts as shown in Figure 4.7. Two mold tools were required to create the part. A top mold insert contained four etched sidewalls which could produce the hexagonal sides of the ferrule to contact the sleeve. To create the sidewalls, a (100) wafer was through-etched in KOH, leaving an open window through the wafer. This open surface is filled by the aluminum mold surfaces when installed in the mold. The bottom mold insert consisted of a series of long triangular features etched from the original wafer surface. When pressed into a compliant material, these features would create v-shaped grooves of approximately 145 μm wide and 100 μm deep. CAD models of the masks used to generate these features are shown in Figure 5.6, while the final etch wafers are shown in Figure 5.7.

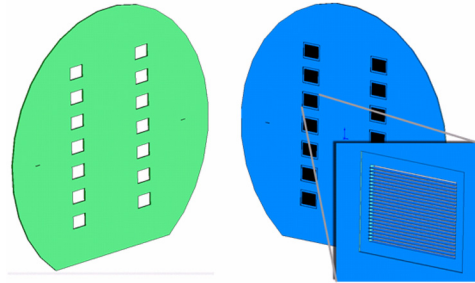


Figure 5.6 CAD Models of Wafer Masks for Fiber Optic Connector

These mold tool inserts were installed in an aluminum mold at Custom Engineering Plastics of San Diego, California¹. Parts were injection molded out of optical grade polycarbonate resin using a Arburg Molding Press. Over 100 connector parts were molded using one groove insert. However, the top mold insert providing the trapezoidal connector shape was limited to under 40 parts before the silicon insert would break. In each trial, the silicon insert would repeatedly break at the corners of the insert, which indicates that the

1. Custom Engineering Plastics (CEP) currently has a website at <http://www.cepi.com/>.

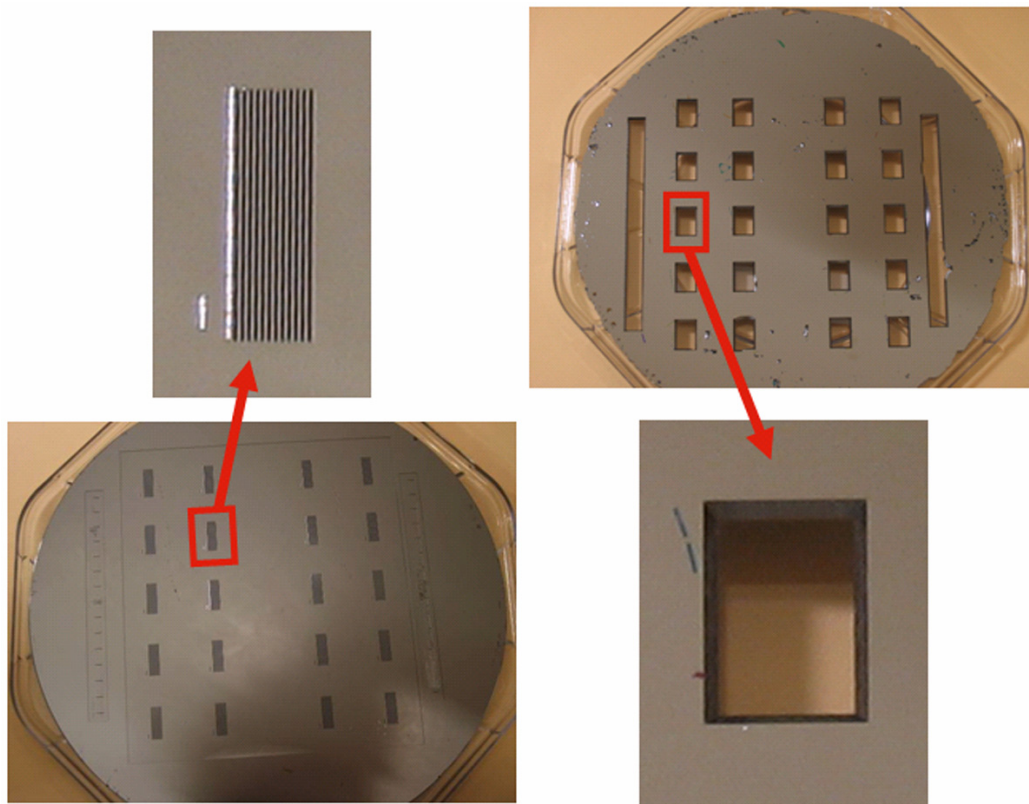


Figure 5.7 Final Silicon Mold Inserts for Fiber Optic Connector

etched surfaces create a stress concentration at the surface intersections. When plastic is injected into the mold, these surfaces experience the injection pressure of the plastic and the sharp intersection line acts as a location for crack initiation. In future trials, this cavity can be changed to remove the stress concentrations or machined using more traditional operations as these features can be made accurately. In Figure 5.8, the silicon mold inserts are shown installed in the aluminum mold base.

After molding the parts, several parts were measured using an optical microscope to determine the repeatability of the open loop molding process. Each groove dimension was repeatable to approximately $5\mu\text{m}$, which was the measured repeatability of the microscope's measuring system. However, significant variation was noticed in the groove dimensions along the length of the connector. This variation is due to an unbalanced gate location at one end of the ferrule. Proper gating would distribute the flow throughout the

ferrule more evenly and prevent the changing groove dimensions. Photographs of the injection molded parts are shown in Figure 5.9 and Figure 5.10, including a ferrule with fibers mounted in the grooves.

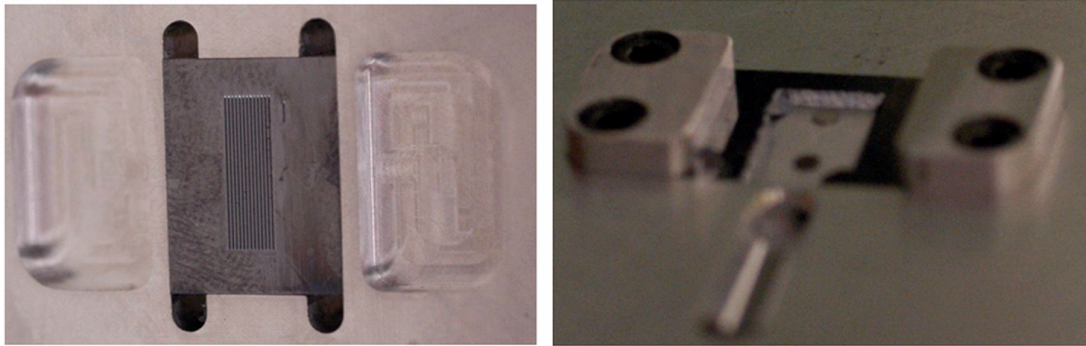


Figure 5.8 Silicon mold inserts installed in aluminum mold - Groove insert (left) and Top trapezoidal shape insert (right)

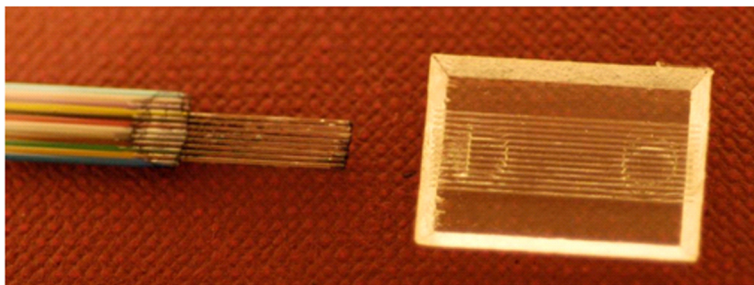


Figure 5.9 Full scale connector shown next to a 12-fiber ribbon cable.

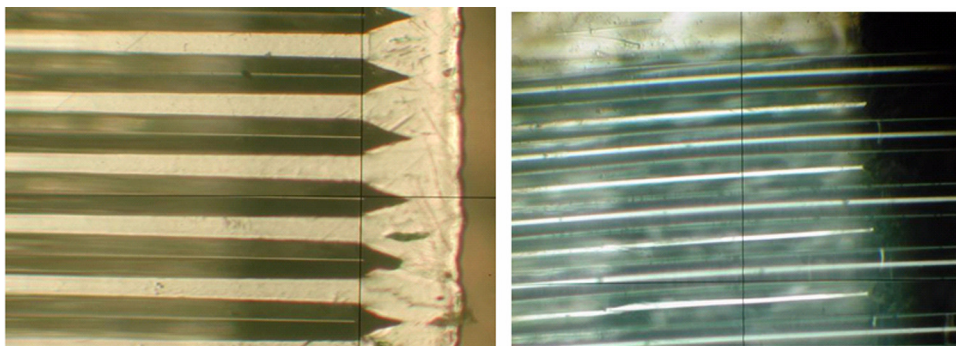


Figure 5.10 Photographs of injection molded ferrules - Plastic grooves (left) and grooves with optical fibers installed (right)

Chapter 6

CONCLUSION

6.1 Contributions of this Thesis

The two major contributions of this thesis are development of a framework that can be used to model an elastically averaged connector and co-development of new precision injection molding process. Within the elastic averaging framework, a method is presented that allows for complex systems to be decomposed into simpler, analytically tractable elements. Using this framework, an analysis process can be used to solve for forces and displacements in the system, allowing Monte Carlo simulations to predict the repeatability of the coupling due to manufacturing tolerances. A simple example and a more complex case study allow for the following design rules and metrics to be confirmed or developed:

- Confirmation of the $(\text{sensitive tolerances})/n^{1/2}$ repeatability trend for elastically averaged designs.
- Development of a correction factor that can be applied based on the amount of cross coupling in the system.
- Development of a qualitative metric for determining whether a system is over constraint, elastically averaged, or exactly constrained.

The major implication of the development of this model is that elastic averaging can be a powerful design alternative to traditional exact constraint design. Exact constraint design can be overemphasized, causing designs to trend towards expensive components, low stiffness, and high contact stresses. In cases where the highest precision or robustness and assembly tolerances are required, exact constraint may still be required. But in cases

where the highest precision is not required, an elastically averaged design can provide low cost, high stiffness, and acceptable accuracy. The emphasis on exact constraint design could then be shifted towards an emphasis on controlled constraint design, where a menu of different constraint options are available based on trade-offs between stiffness, accuracy, and cost. In the case study on the fiber optic connector, elastic averaging presents a viable alternative to the existing over-constrained and expensive solutions. Such a design combined with a low cost precision injection molding process could lower the cost of optic connectors to a level where fiber-to-the-door plans become reasonable.

In addition to the elastic averaging model framework, fidelity development of the Silicon Insert Molded Plastics indicates that the process can provide micron level dimensions with repeatability of less than 5 μ m. The further development of the SIMP process will greatly improve the resolution and accuracy of features currently available in injection molded polymers. While micron and sub-micron features can currently be injection molded or stamped, the processes used to create such parts are prohibitively expensive or limited to 2 or 2.5 dimensions. The SIMP process is one of the few currently feasible processes capable of creating true 3D geometry at a low cost, indicating that the possibilities for the process are excellent.

6.2 Future Work

6.2.1 Further Development of SIMP and Actual Scale Model Connector Tests

In Chapter 4, experiments were conducted on a 5X scale version of the connector. To properly determine the repeatability and accuracy of the elastic averaging design for this application, further experimentation is required at the actual scale size. A Small Business Innovative Research Grant from the National Science Foundation was obtained to produce more robust “production” style silicon inserts to be produced at MIT in 2005. These mold inserts can be used to generate high quality connector ferrules which can be assembled and tested.

In this research, a number of factors must be considered to make the precision parts a reality. While a detailed analysis of these factors is beyond the scope of this thesis, some issues to be addressed include the proper selection of a stable material, determination of the best processing parameters used during molding, a study of silicon mold tool wear and lifetime, and investigation into the best location for gating and venting, including possibilities such as mold evacuation and thermal strategies. Typically, most fiber optic connector designs avoid common thermoplastic materials such as polycarbonate due to their tendency to be hygroscopic and swell due to moisture absorption, to have poor dimensional stability, and to have relatively higher thermal expansion than some metals. These behaviors negatively affect connector loss as they can alter the position of fiber within the connector, as well as change the structure of the connector itself. Many connectors use materials such as ceramics and compression molded phenolics to avoid these issues. Newer studies have shown that these effects may not be as critical as once thought, so that resistance to using these materials may decrease. Proper selection and processing of the materials will allow for the connector to be made out of different engineering plastics.

Once these issues have been addressed, usable test parts can be molded and tested. Experiments that would be required include repeatability measurements across a sample of molded parts to accurately capture total repeatability, including interchangeability due to manufacturing variations and non-deterministic variations due to friction, assembly order, thermal variations, etc. Due to the small size of the connectors, designing a position measurement system for the complete system would be fairly difficult, although the individual ferrule halves and the assembled ferrules could be easily measured. Therefore, it may be more effective to install fibers into the connectors and measure the optical performance of the connectors. Another point to address in the scale versions is the robustness of the sleeve's preload beams. Other preload concepts similar to those used in other connector designs may be more robust during assembly.

6.2.2 Extension of Symmetric Elastically Averaged Design

While developing the design of the fiber optic connector, 5X scaled versions of the design were built to simplify testing procedures. The goal of the thesis was to directly apply these models to the connector. However, the 5X scale models could also be expanded upon and used as a large scale shaft coupling in rotating systems. Two shafts could be formed with hexagonal or any number of sides, then aligned using an elastically averaged sleeve segment. The sleeve would provide high accuracy interconnection between shafts with little or no backlash. To permit minor misalignment between the shafts, slits could be cut along its length to permit some relative motion along the shaft.

Furthermore, the design concept for the connector provided in Chapter 4 is primarily a refinement on existing designs. One adaptation of the design adds a larger groove on each side of the fiber grooves which could accommodate the pins used in the MT ferrule design. This design would leverage the improved accuracy due to the SIMP manufacturing process while remaining compatible with the existing dominant design. The principle of elastic averaging could be extended beyond the limited case discussed here to create designs which have the alignment features integrated into the ferrule, eliminating the need for a separate sleeve. In this case, the high quality grooves produced using SIMP could allow for elastic averaging between two ferrules in a similar way to the method where the two ferrule halves are joined.

6.2.3 Metric for Determinism of Elastic Averaging

Since the border between elastic averaging and improper over-constraint can be easily crossed, it would be useful for the designer to have a metric available to indicate when their design is near this border. In Chapter 3, a qualitative metric for describing this relationship was briefly discussed. While this metric is intuitively useful, it would be more useful to have a more quantitative understanding of this metric. Future work to develop this metric would include a method to evaluate the relationship between the cross coupled stiffness values to the designed compliant structure. This metric would then allow for a

designer to quickly test if the compliant components intended to allow elastic averaging are deterministically constraining the device within manufacturing variation or if the compliant components are too stiff and create non-deterministic overconstrained. In order to test this metric, some of the elastically averaged devices previously considered would need to be analyzed and compared.

Using this metric and the design process discussed above, the concept of elastic averaging could be extended to other areas. For example, automotive applications such as sheet metal assemblies or engine block assemblies could benefit from the improved repeatability and robustness of an elastically averaged design. While these assemblies employ similar modeling methods, they essentially remain over-constrained assemblies without sufficient compliance. The addition of compliance or planar kinematic couplings could improve the accuracy of the assemblies while lowering cost.

REFERENCES

Precision Assemblies

- [1] Slocum, Alexander H. "Design of Three-Groove Kinematic Couplings." *Precision Engineering*, Vol. 14, No. 2, 67-76, 1992.
- [2] Culpepper, Martin L. "Design and Application of Compliant Quasi-Kinematic Couplings", Ph.D. Thesis, Massachusetts Institute of Technology, Cambridge, MA, 2000.
- [3] Culpepper, Martin L. "Design of Quasi-Kinematic Couplings." *Precision Engineering*, Vol. 28, No. 3, 338-357, 2004.
- [4] Slocum, Alexander H. Precision Machine Design. Prentice-Hall: Englewood Cliffs, NJ, 1992.
- [5] Blanding, Douglas K. Exact Constraint: Machine Design Using Kinematic Principles. ASME Press: New York, 1999.
- [6] Johnson, K.L. Contact Mechanics. Cambridge University Press: Cambridge, UK, 1985.
- [7] Bickford, John H. and Sayed Nassar, eds. Handbook of Bolts and Bolted Joints. Marcel Dekker, Inc.: New York, 1998.
- [8] A.J. Hart. "Design and Analysis of Kinematic Couplings for Modular Machine and Instrumentation Structures." Master's Thesis, Massachusetts Institute of Technology, Cambridge, MA, 2001.
- [9] P.J. Willoughby. "Kinematic Alignment of Precision Robotic Elements in Factory Environments." Master's Thesis, Massachusetts Institute of Technology, Cambridge, MA, 2001.

Elastic Averaging:

- [10] Merton, Thomas. "On the Reproduction and Ruling of Diffraction Gratings." *Proceedings of the Royal Society of London, Series A, Mathematical and Physical Sciences*, Vol. 201, No. 1065 (Mar. 22, 1950), 187-191.
- [11] Strong, John. "New Johns Hopkins Ruling Engine." *Journal of the Optical Society*, Vol. 41, No. 1, 1951, 3-15.
- [12] Sayce, L.A. "The production of accurate linear scales by means of the Merton nut." *Journal of Scientific Instruments*, Vol 32, 1955, 11-12.

- [13] Jones, R.V. "Some uses of elasticity in instrument design." *Journal of Scientific Instruments*, 1962, Vol.39, 193-203.
- [14] Moore, W. R. Foundations of Mechanical Accuracy. Moore Special Tool Company, Bridgeport Connecticut, 1970.
- [15] Smith, H. W. "Static test of an ultralight airplane." General Aviation Technology Conference of AIAA, Anaheim, CA, Sept. 29-Oct. 1, 1986.
- [16] K. Autumn, Y. Liang, W. P. Chan, T. Hsieh, R. Fearing, T. W. Kenny, and R. Full, "Dry adhesive force of a single gecko foot-hair," *Nature*, vol. 405, pp. 681–685, 2000.
- [17] G. K. Christiansen, "Toy Building Brick," U.S. Pat. 3 005 282, Oct. 1961.
- [18] Slocum, A. H., Weber, A. C. "Precision Passive Mechanical Alignment of Wafers" *Journal of Microelectromechanical Systems*, Vol 12, No 6, December 2003, 826-834.
- [19] M. Balasubramaniam, H. Dunn, E. Golaski, S. Son, K. Sriram, and A. Slocum, "An anti backlash two-part shaft with interlocking elastically averaged teeth," *Precis. Eng.*, vol. 26, no. 3, pp. 314–330, 2002.
- [20] Beer, Ferdinand P. and Russell Johnston, Jr. Mechanics of Materials. 2nd ed. McGraw-Hill, Inc.: New York, 1992.
- [21] Gere, J.M. Mechanics of Materials. 5th ed. Brooks and Cole: Pacific Grove, CA, 2001.
- [22] Young, Warren C. Roark's Formulas for Stress and Strain. 6th ed. McGraw Hill: New York, 1989.
- [23] S. S. Rao. Mechanical Vibrations. 3rd ed. Addison-Wesley Publishing Company: New York, 1995.
- [24] Strang, G. Introduction to Applied Mathematics. Wellesley-Cambridge Press: Cambridge, MA, 1986.
- [25] Bathe, K.J., Finite Element Procedures in Engineering Analysis. Prentice-Hall, Englewood Cliffs, NJ, 1982.
- [26] Przemieniecki, J. S., Theory of Matrix Structural Analysis, McGraw-Hill, New York, 1968; Dover edition 1986.

Fiber Optic Connector Chapter:

- [27] E. Hecht. Optics. 4th ed. Addison Wesley: New York, 2001.
- [28] M. Born and E. Wolf. Principles of Optics: Electromagnetic Theory of Propagation, Interference and Diffraction of Light. 7th ed. Cambridge University Press: 1999.

-
- [29] D. Marcuse. "Loss Analysis of Single-Mode Fiber Splices." *The Bell System Technical Journal*, Vol. 56, No. 5, June 1977, pp 703 - 718.
- [30] B. Elliott and M. Gilmore. Fiber Optic Cabling. 2nd ed. Newnes, Oxford, UK, 2002.
- [31] C.M. Miller. Optical Fiber Splices and Connectors. Marcel Decker, Inc: New York, 1986.
- [32] J.M. Trehwella, C.M. DeCusatis, and J. Fox. "Performance Comparison of Small Form Factor Fiber Optic Connectors." *IEEE Transactions on Advanced Packaging*, Vol. 23, No. 2, MAY 2000, pp 188-196.
- [33] M. Takaya, S. Nagasawa, and Y. Murakami. "Design and Performance of Very High-Density Multifiber Connectors Employing Monolithic 60-Fiber Ferrules." *IEEE Photonics Technology Letters*, Vol. 11, No. 11, pp1446 - 1448, November 1999.

Precision Molding and SIMP Chapter:

- [34] J.B. Werkmeister. "Design of Silicon Insert Molded Plastics." Engineer's Degree Thesis, Massachusetts Institute of Technology, June 2005.
- [35] H. E. Trucks. Designing for Economical Production. 2nd ed. Dearborn, Michigan: Society of Manufacturing Engineers, 1987.
- [36] Various articles available from Injection Molding Magazine Online at <http://www.immnet.com>
- [37] D. V. Rosato, D. V. Rosato, and M. G. Rosato. Injection Molding Handbook. 3rd ed. Boston: Kluwer Academic Publishers, 2000.
- [38] Pohlmann, Ken C. The Compact Disc Handbook. Madison: A-R Editions, Inc.: 1992.
- [39] Product information on Sesame NanoMolding Machine by Murray Engineering at <http://www.nanomolding.com>
- [40] Y. Xia and G. M. Whitesides. "Soft Lithography." Angewandte Chemie International Edition, 37 (1998): 550-575.
- [41] T. Hannemann, W. Pfleging, J. Hausselt, K.-H. Zum Gahr. "Laser Micromachining and Light Induced Reaction Injection Molding as Suitable Process Sequence for the Rapid Fabrication of Microcomponents." Microsystem Technologies, 7 (2002): 209 - 214.
- [42] V. Piotter, W. Bauer, T. Benzler, A. Emde. "Injection Molding of Components for Microsystems." Microsystem Technologies, 7 (2001): 99 - 102.
- [43] R. W. Jaszeqski, H. Schrift, J. Gobrecht, and P. Smith. "Nano replication in Polymers." Available online at <http://www.snf.ch/nfp/nfp36/progress/schrift.html>.

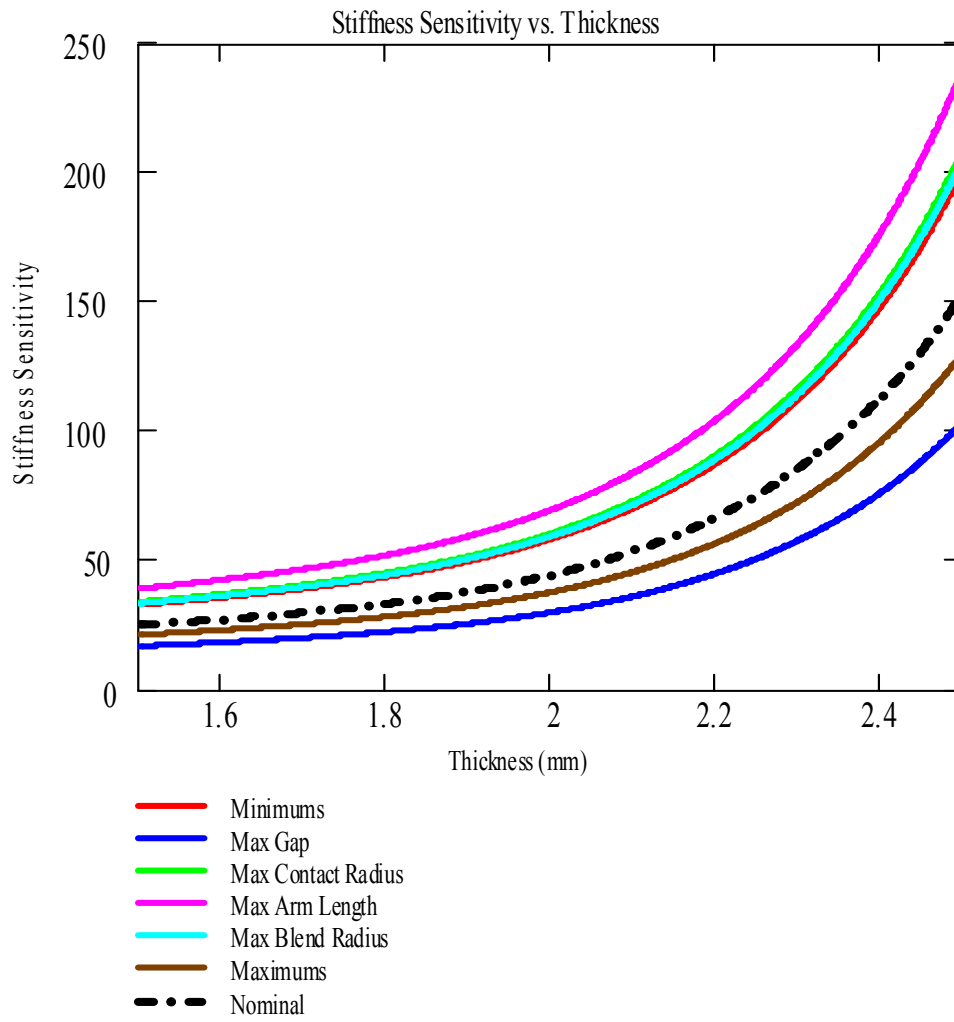
- [44] S. Chou, P. Krauss, W. Zhang, L. Guo, and L. Zhuang. "Sub-10 nm Imprint Lithography and Applications." Journal of Vacuum Science Technology, 1997: 2897 - 2904.
- [45] C. M. Park, B. H. Choi, C. K. Hyon, S. W. Hwang, D. Ahn, and E. K. Kim. "Nano Mold Lithography for 40-nm Patterns." Journal of the Korean Physical Society, 2001: 157 - 159.
- [46] Thermo RGL Company website. Online at <http://www.gratinglab.com/>
- [47] J. Hruby. "The State of LIGA Development at Sandia Labs." Semicon2000, 2000.
- [48] LIGA Process website at Forschungszentrum Karlsruhe. Online at http://www.fzk.de/pmt/arbeits Themen/datenblaetter_englisch/liga.htm
- [49] J. Hruby. "LIGA Technologies and Applications." MRS Bulletin, April 2001: 337 - 340.
- [50] K.S. Kim, S.W. Park, J.B. Lee, H. Manohara, Y. Desta, M. Murphy, and C.H. Ahn. "Rapid Replication of Polymeric and Metallic High Aspect Ratio Microstructures using PDMS and LIGA Technology", HARMST 2001, 2001.
- [51] S.W. Park, K.S. Kim, H. Manohara, and J.B. Lee, "Massive Replication of Polymeric High Aspect Ratio Microstructures Using PDMS Casting", SPIE 2001 Smart Electronics and MEMS, 2001.
- [52] M. Hoffman, S. Dickhut, and E. Voges. "Silicon Fibre Ribbon Pigtailed with Rhombus-Shaped Fibre Channels and Integrated Photodiodes." Micro Opto Electro Mechanical Systems, 1999: 206 - 209.
- [53] Balasubramaniam, M., Dunn, H., Golaski, E., Son, S., Sriram, K., Slocum, A., "An anti backlash two-part shaft coupling with interlocking elastically averaged teeth", Precis Eng., Volume 26, No. 3 pp. 314-330
- [54] Slocum, A. H. "Design of Three-Groove Kinematic Couplings," Precision Eng., Vol. 14, No. 2, April 1992, pp 67-76.

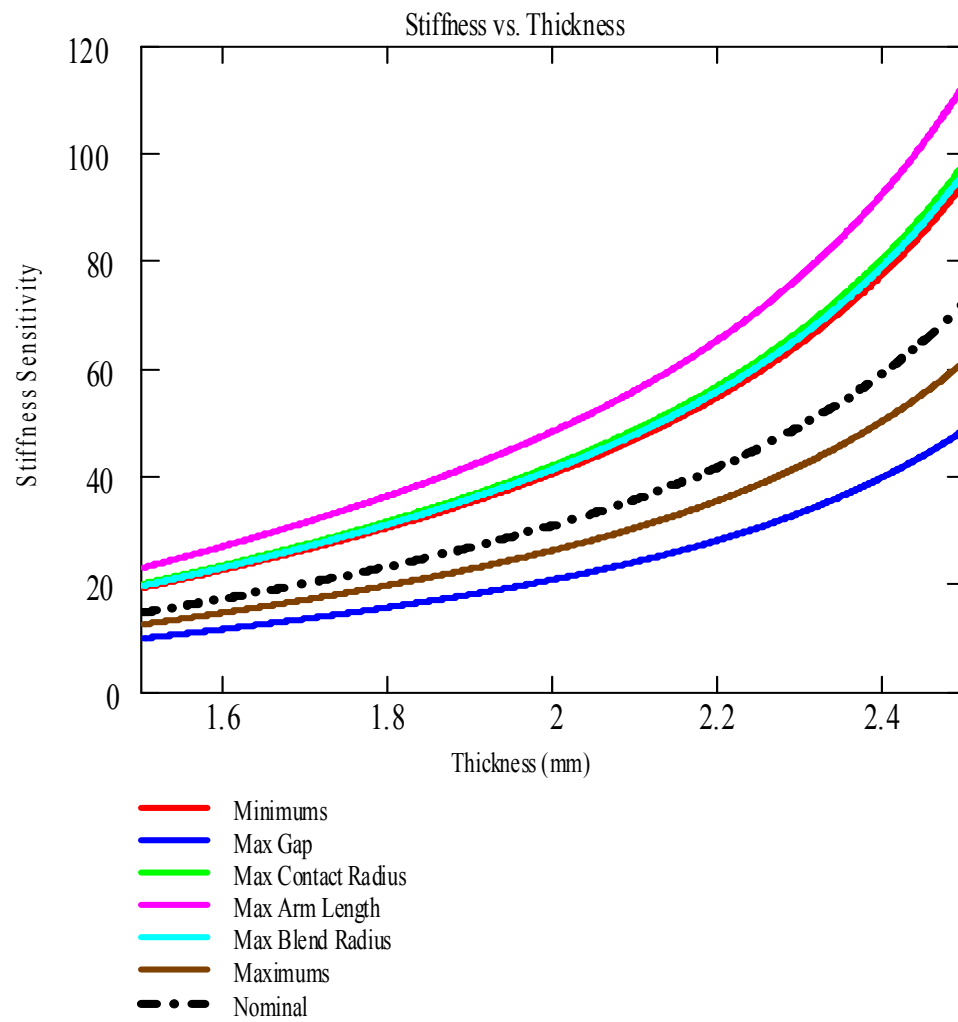
Appendix A

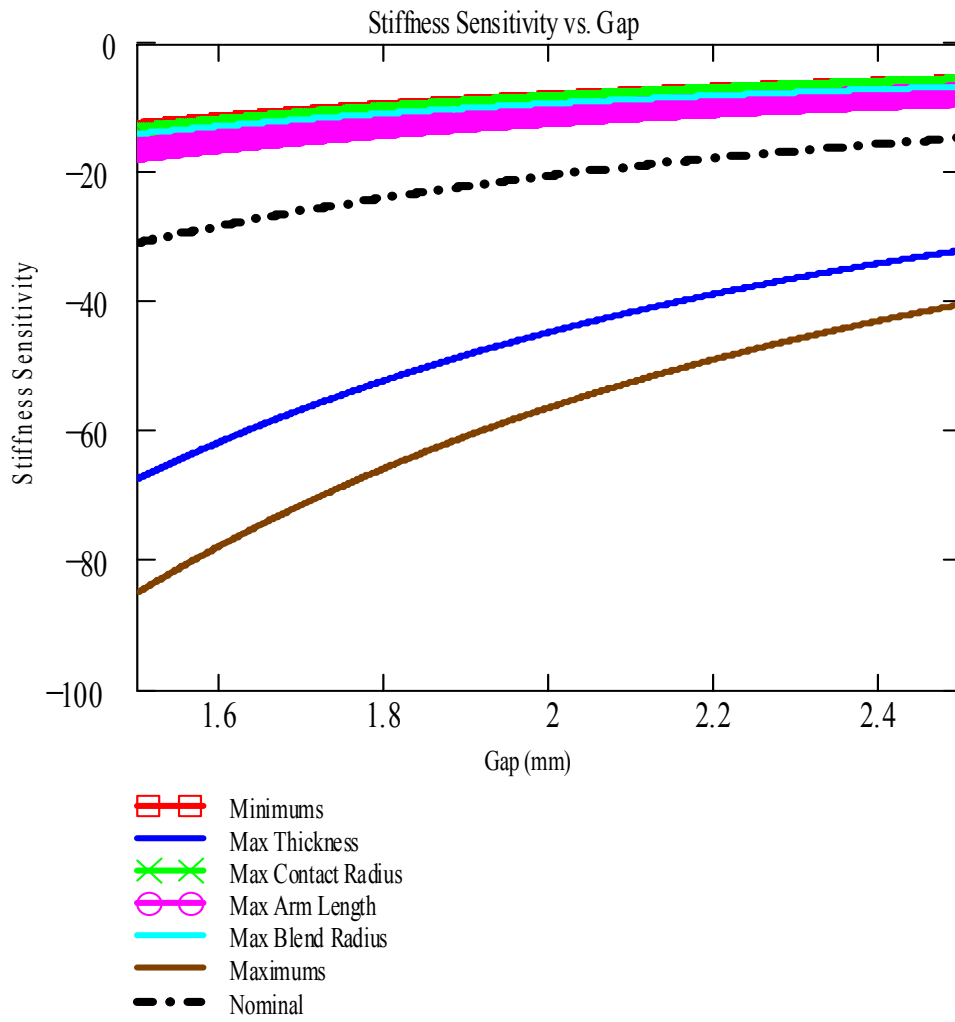
SENSITIVITY ANALYSIS PLOTS AND EXAMPLE FEA FIGURES

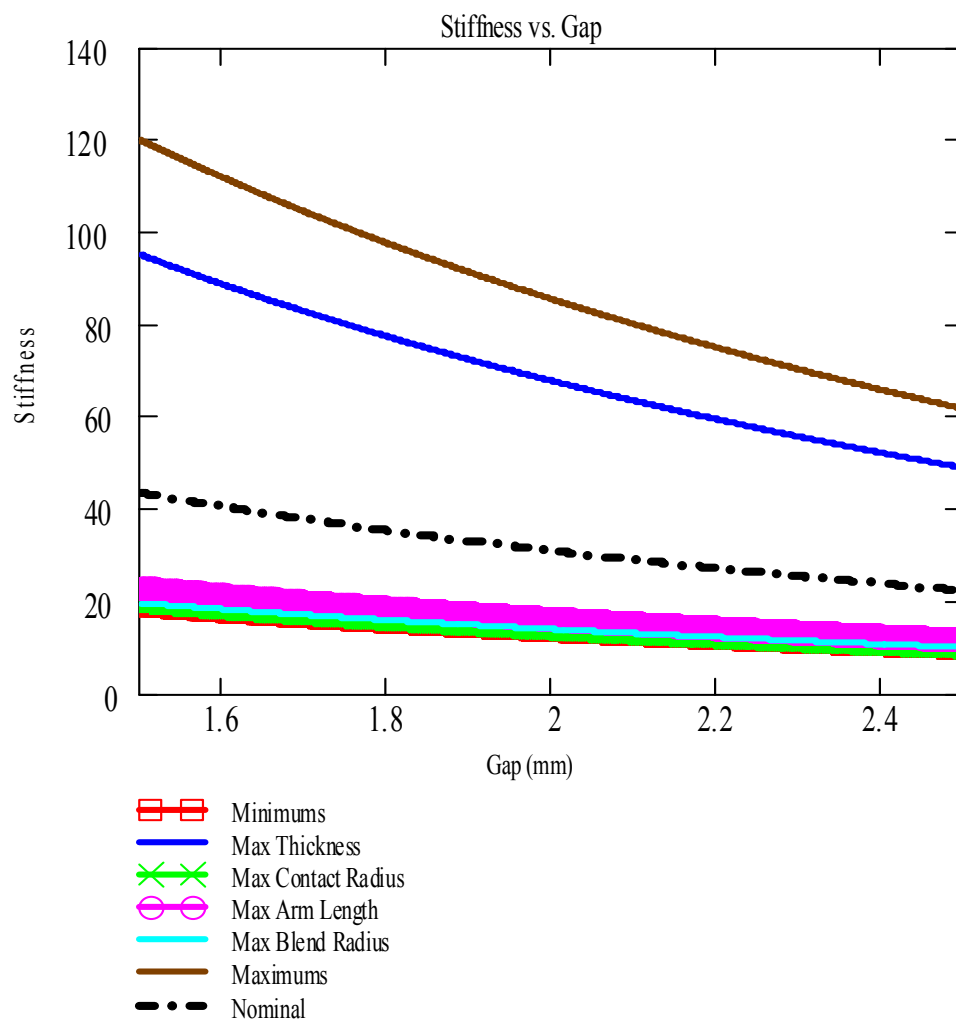
6.3 Sensitivity Plots

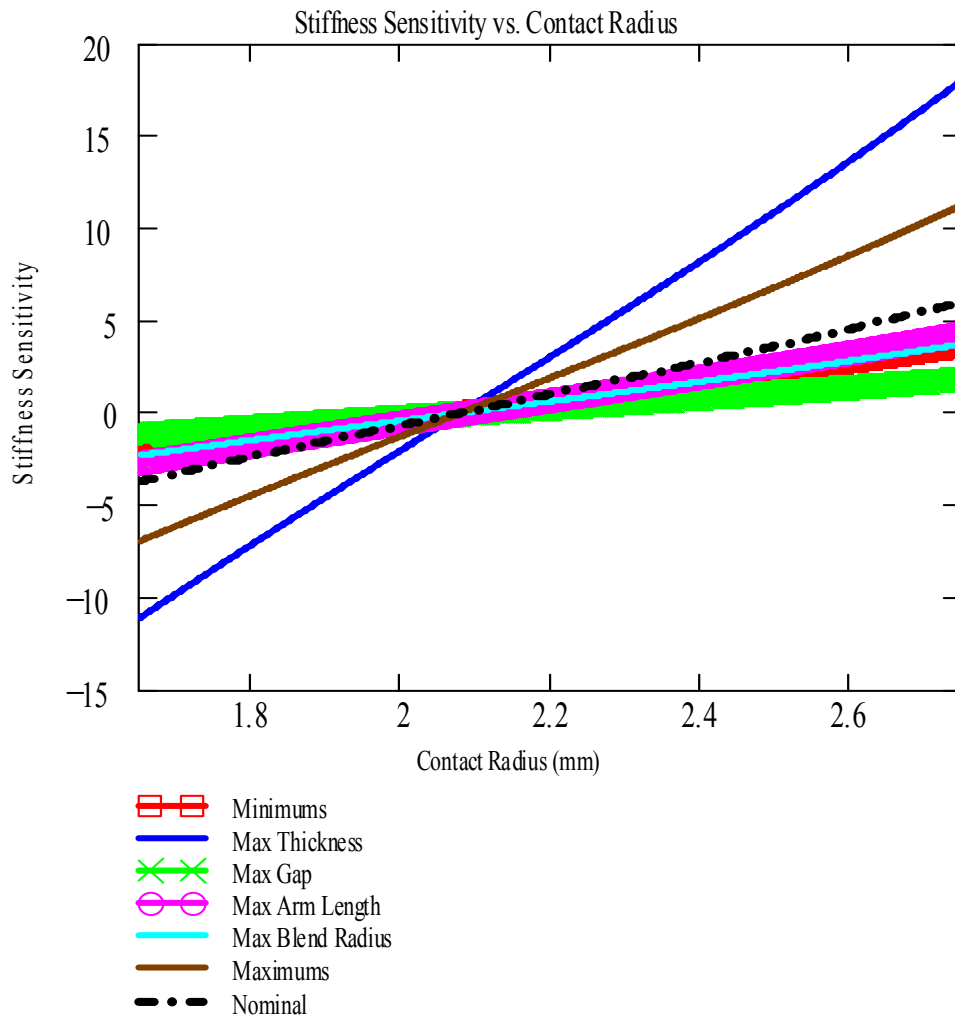
The first set of plots show stiffness sensitivity and stiffness versus different dimensions combinations for the sleeve. All plots show variation of -25% to +25% of the nominal values given in the commercially produced extruded sleeve.

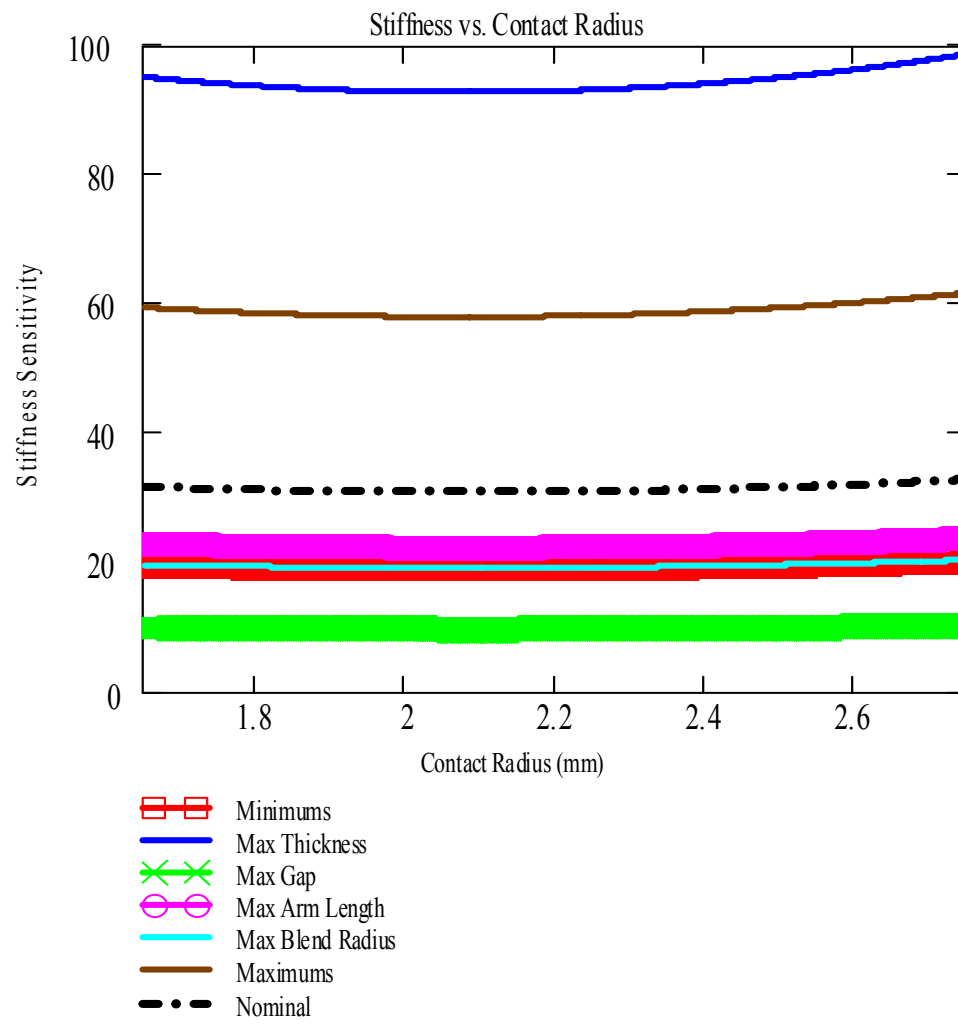


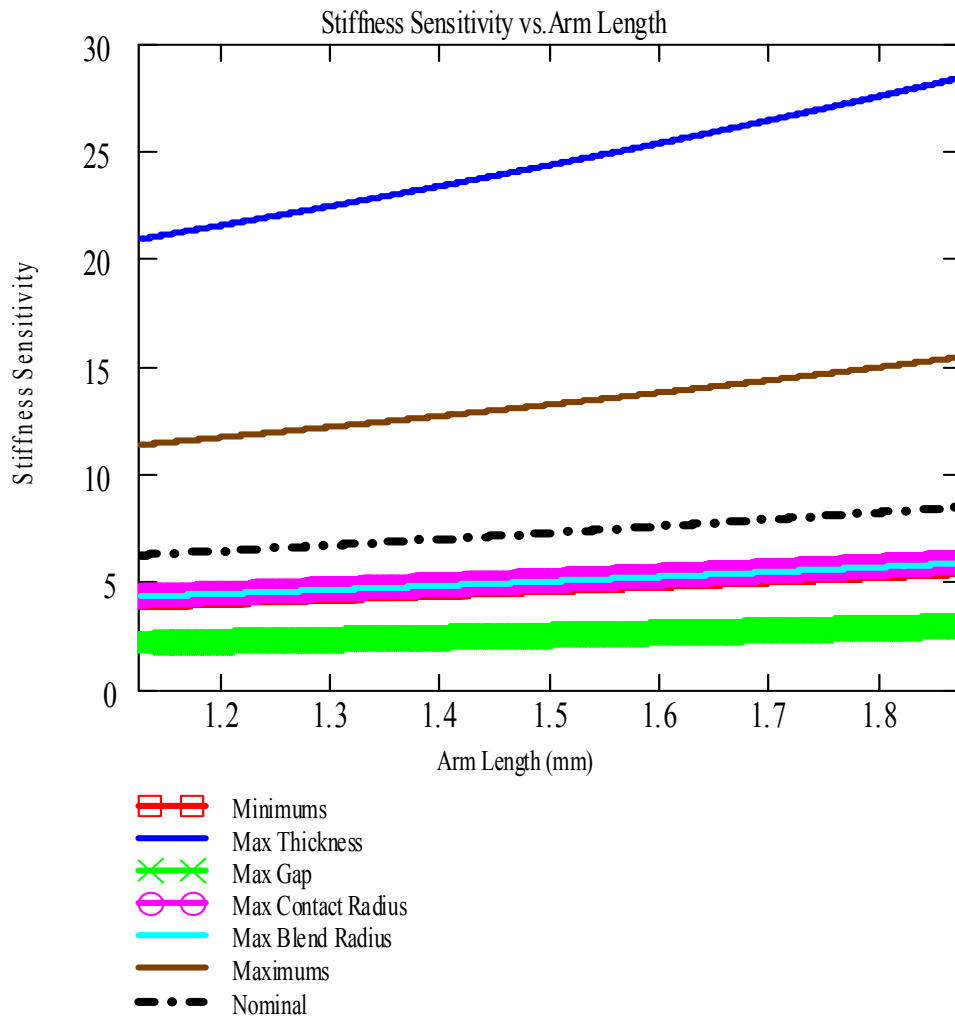


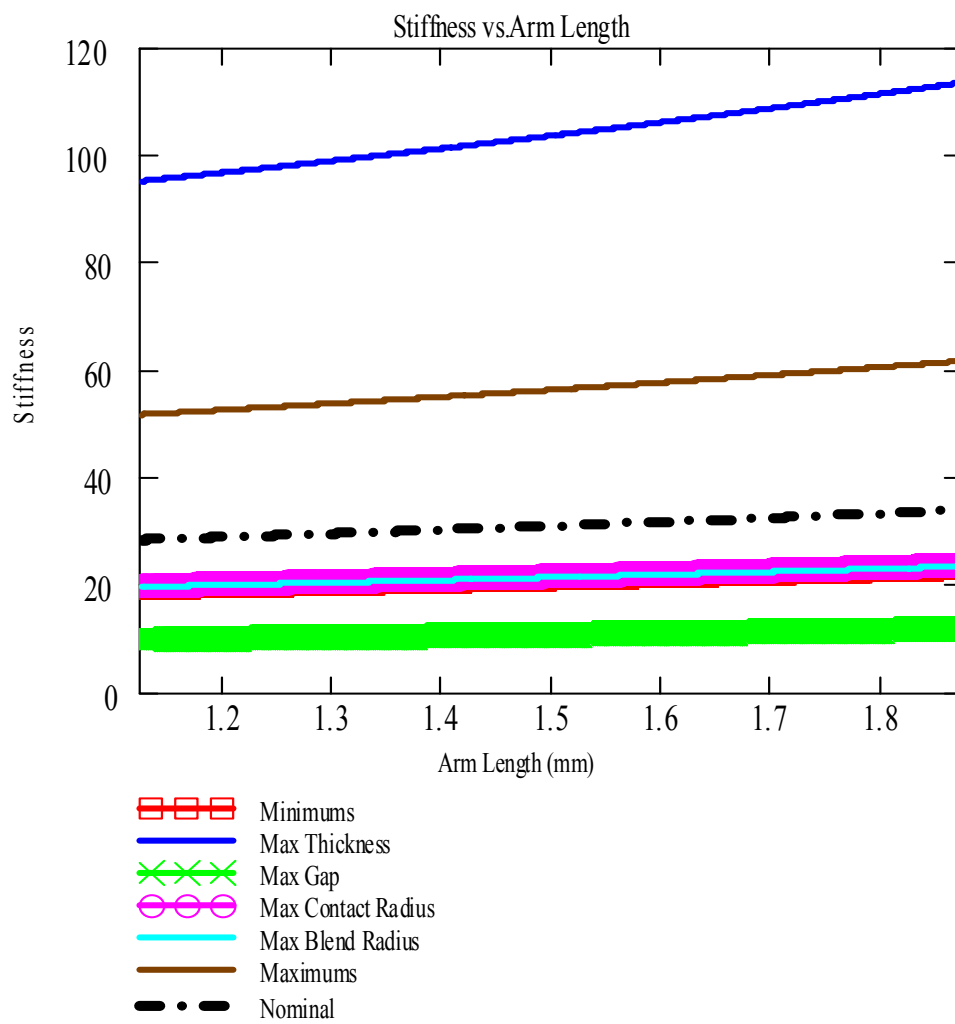


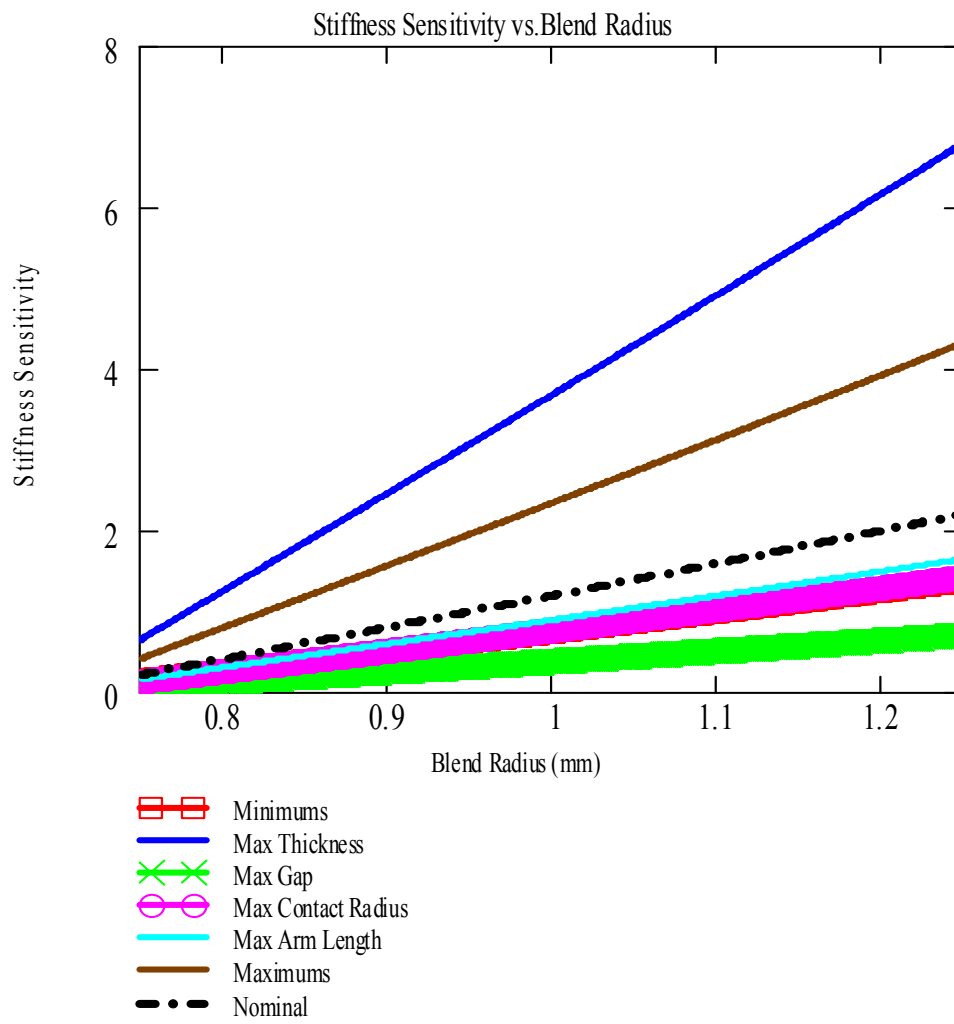


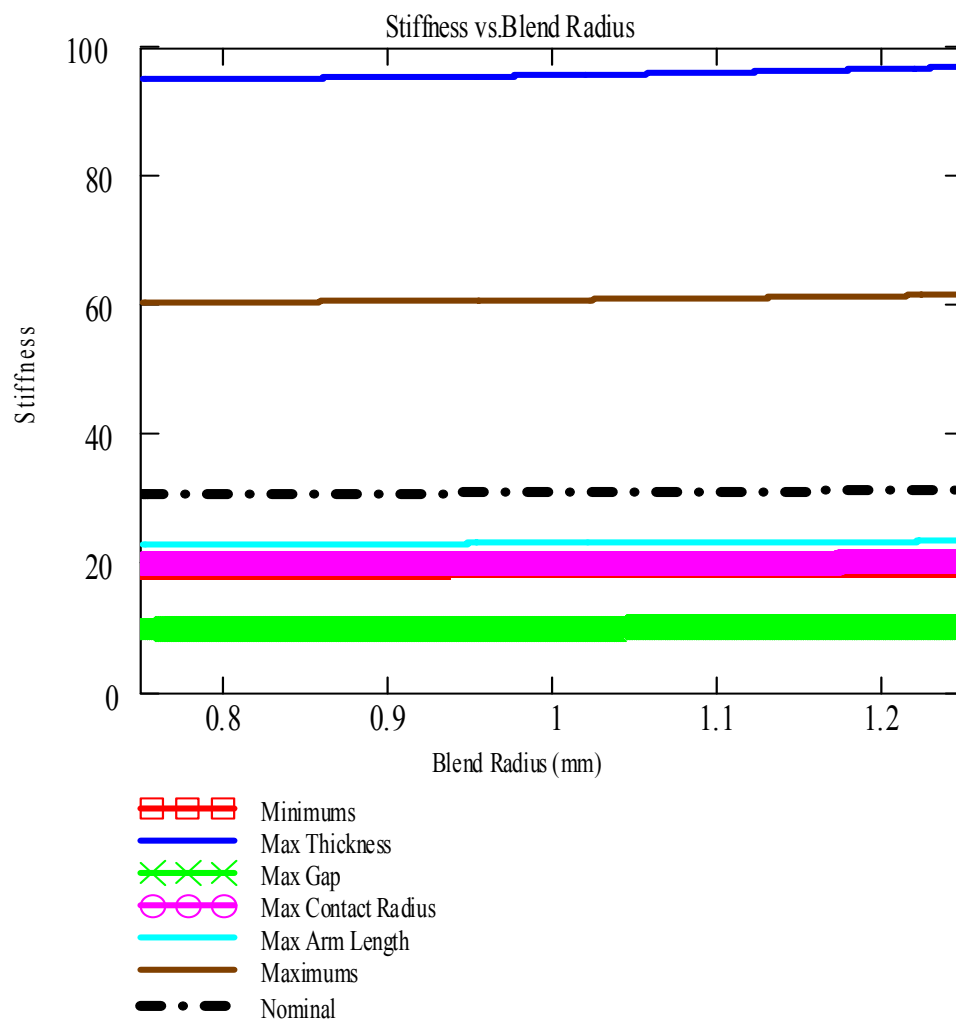


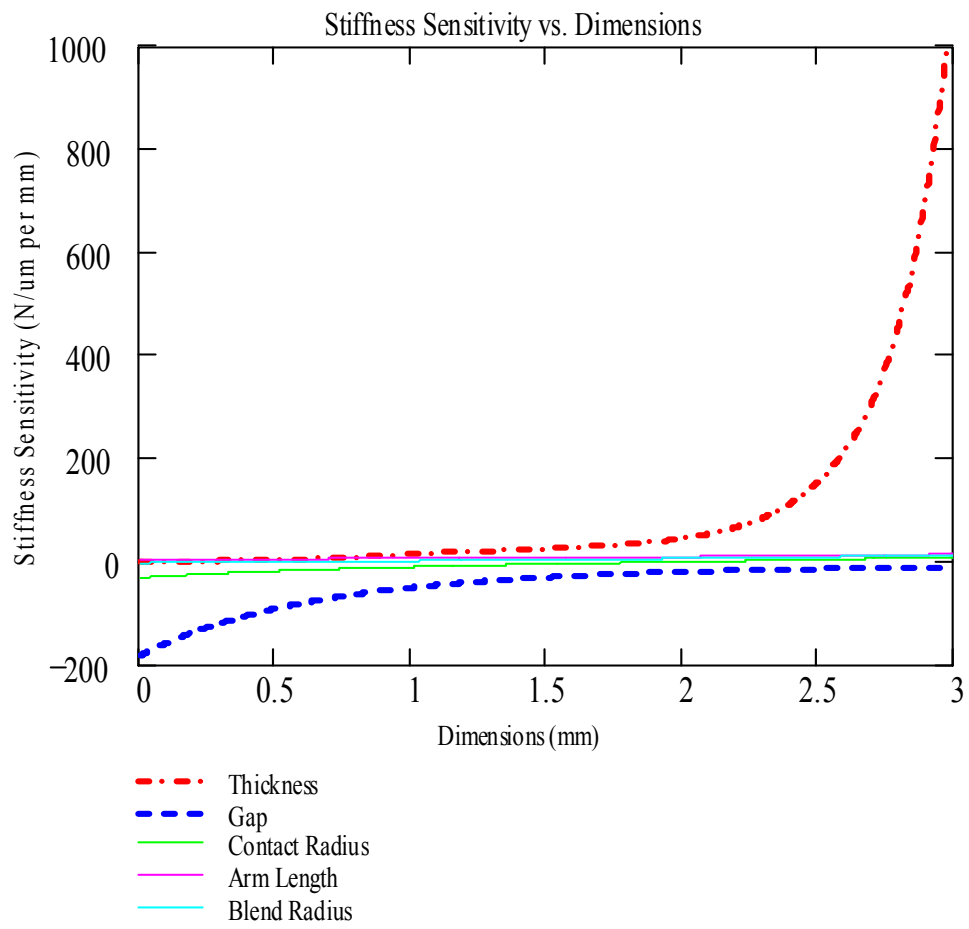


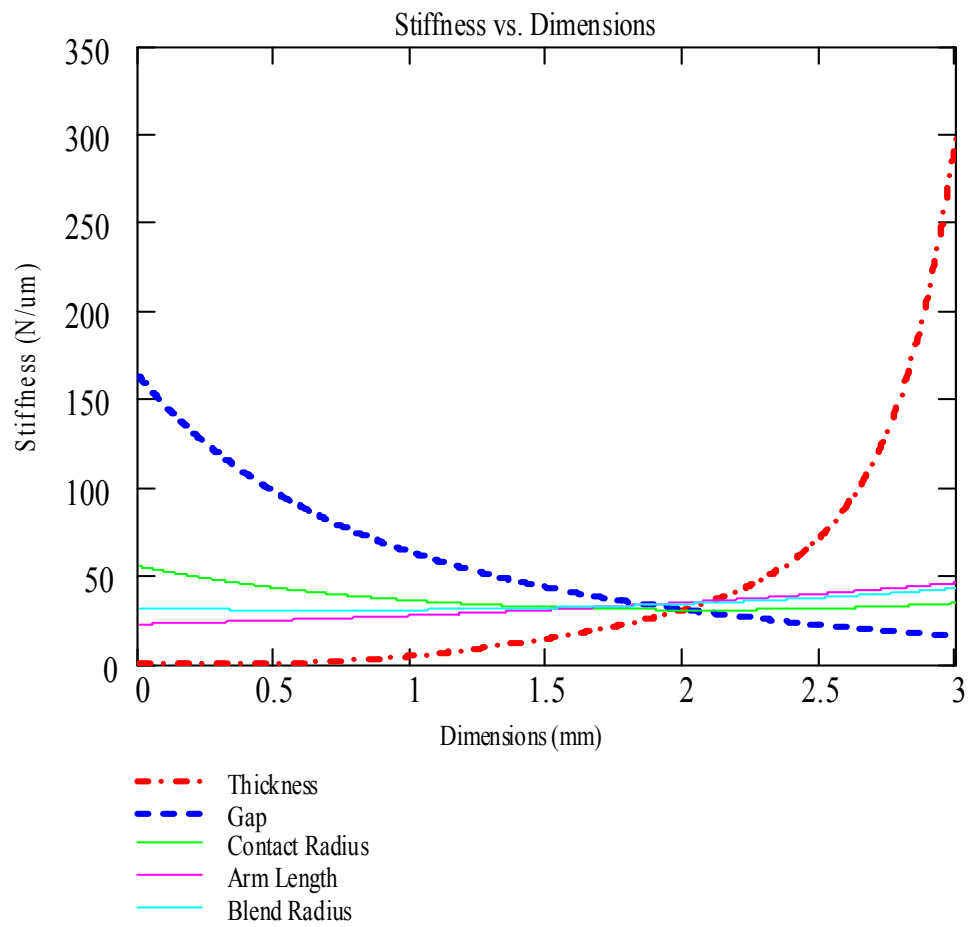












6.4 FEA Figures

The following FEA figures illustrate the mesh and different boundary conditions used for analyzing the 5X scale model of the fiber optic connector. Figure A.1 and Figure A.2 show the mesh and an example displacement plot for the sensitivity model. This model consists of a quarter model with appropriate symmetry boundary conditions applied at the edge. Symmetry boundary conditions allow motion along the plane of symmetry, but do not permit any nodes to cross the symmetry plane. Force boundary conditions were applied at the contact points to obtain a displacement profile. The FEA software automatically changes the dimensional parameters and determines sensitivities.

Figure A.3 and Figure A.4 show the mesh and an example displacement plot for the stiffness parameterization model for the non-coupled stiffness behavior. This model consists of a full model displacement constraints applied at each contact point. These constraints had two purposes - to prevent free motion and to simulate the press-fit action caused by the ferrule's insertion in the sleeve. Traditional boundary conditions could not be applied to allow force boundary conditions to be used, so reaction forces were calculated in the analysis. Multiple solver runs with dimensional parameter combinations are then performed to obtain data to create the parameterized stiffness equation.

Figure A.5 and Figure A.6 show the mesh and an example displacement plot for the FEA model for the coupled stiffness behavior. The boundary conditions from the previous analyses are replaced with gap elements, which obtain forces for motions which close the gap and create contact and obtains displacements for motions without contact. To prevent free motion, springs with negligible stiffness are placed on the model. These springs allow the solver to find solutions for the model without affecting results.

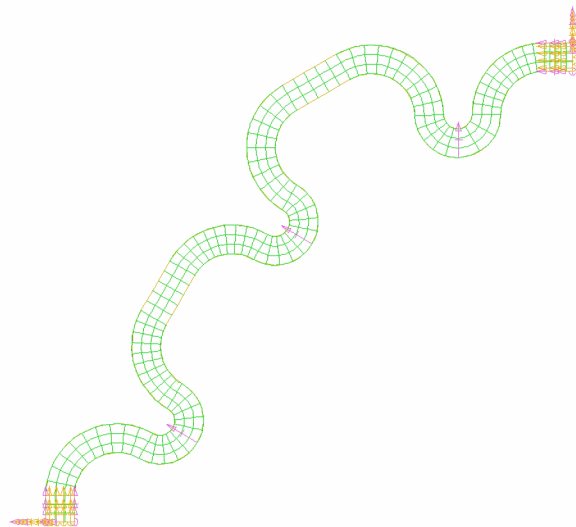


Figure A.1 FEA Mesh used for determining stiffness sensitivity

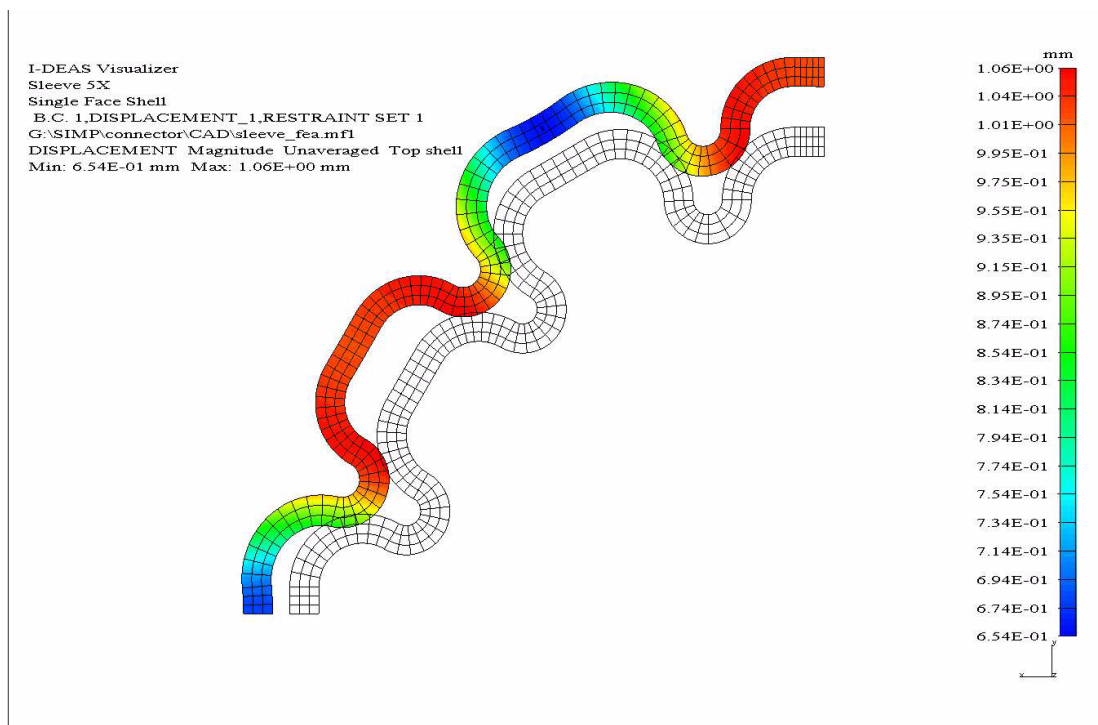


Figure A.2 Example displacement results from FEA mesh for quarter model of sleeve

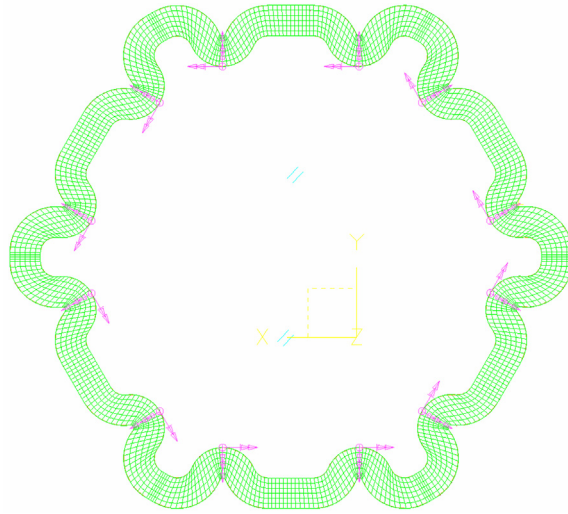


Figure A.3 FEA Mesh used for determining nominal stiffness behavior of sleeve using displacement boundary conditions

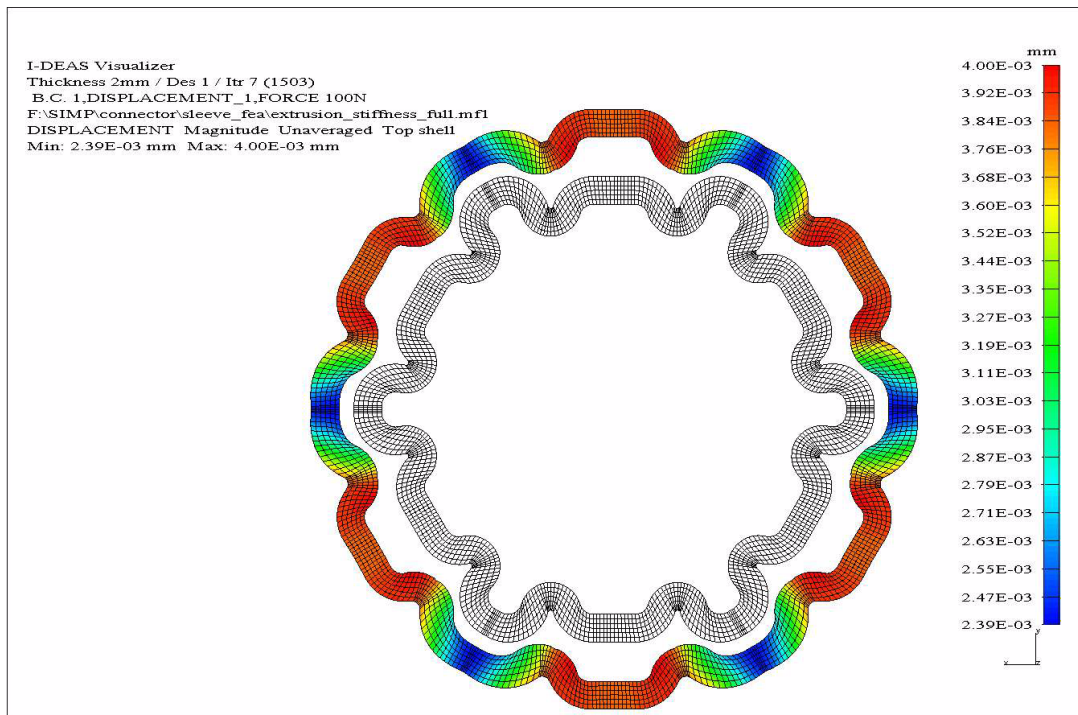


Figure A.4 Example displacement results from FEA mesh for full model of sleeve using displacement boundary conditions

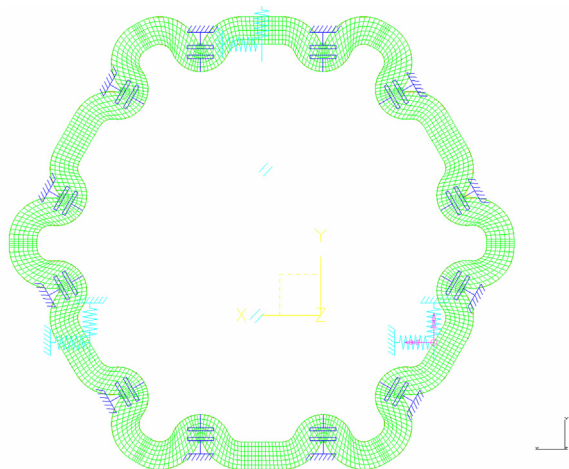


Figure A.5 FEA Mesh used for determining coupled stiffness behavior of sleeve using gap elements

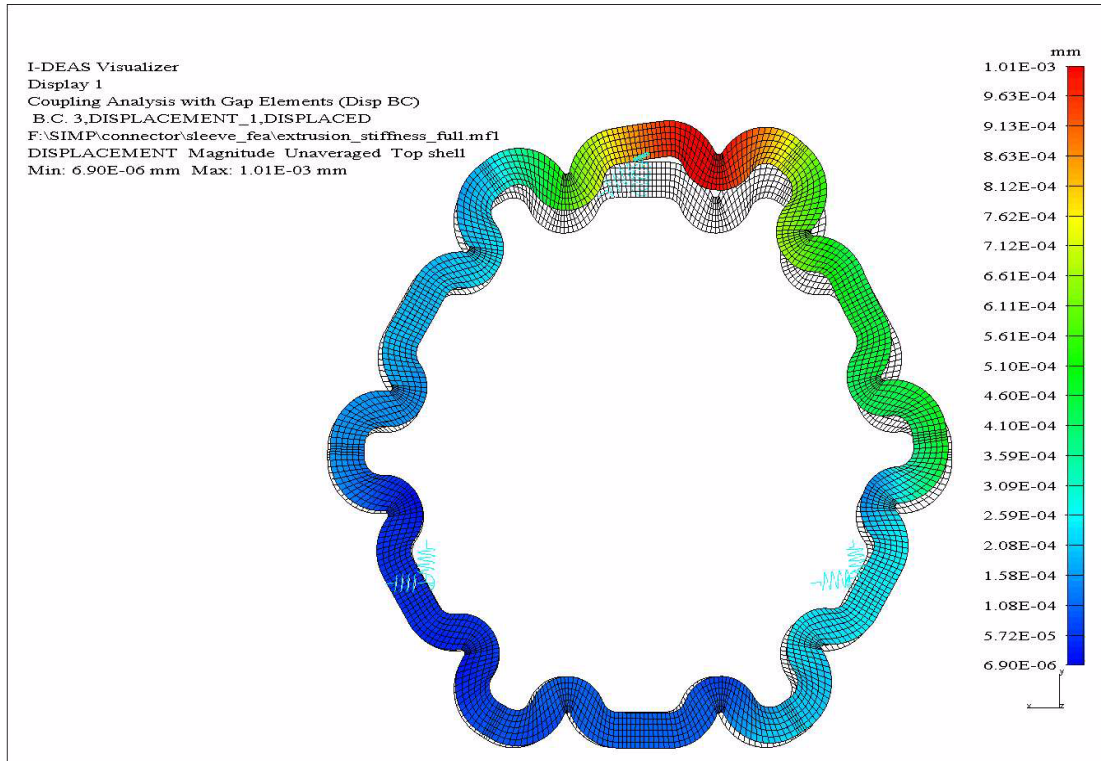


Figure A.6 Example displacement results from FEA mesh for full model of sleeve using gap elements and displacement at one contact point

Appendix B

MATHEMATICS FOR SIMPLE ELASTIC AVERAGING MODEL

A description of this simple model is available in Chapter 3. The schematic of the model is shown in Figure B.1 for reference. The following code is in MathCAD 11 format.

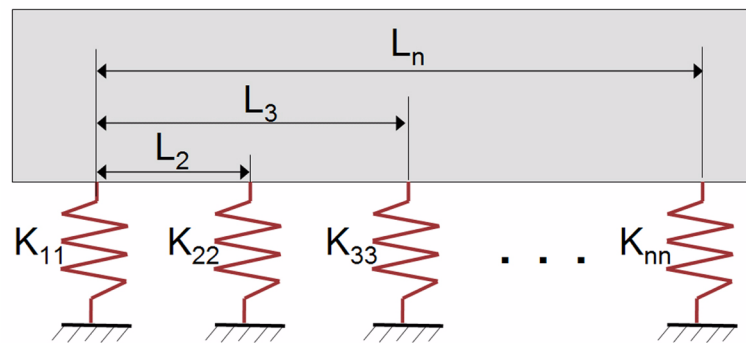


Figure B.1 - Schematic of simple one dimensional rigid beam model

Define the basic inputs for the analysis:

Number of contact points:	<code>contacts := 5</code>
Are the contacts in a continuous loop:	<code>circle := 0</code>
How many nearest neighbors are effected:	<code>neighbors := 2</code>
Stiffness of the main spring elements (assumed to be same for all springs):	<code>k₁ := 1</code>
Percentage dropoff in stiffness due to force cross coupling:	<code>k_percent := 10%</code>
Percentage dropoff in stiffness due to displacement cross coupling:	<code>d_percent := 10%</code>
Nominal value for input tolerances:	<code>x_{nom} := 0</code>
Standard deviation of input tolerances:	<code>x_σ := 1</code>
Length between first and last contact point:	<code>L_{total} := 10</code>

Create random normal distribution of tolerances:

$$x := \text{rnorm}(\text{contacts}, x_{\text{nom}}, x_{\sigma}) \quad x := \begin{pmatrix} -0.439 \\ -0.679 \\ -0.473 \\ -0.951 \\ -1.686 \end{pmatrix}$$

Define spacing between contact points to be equal:

$$L_{\text{spacing}} := \frac{10}{\text{contacts} - 1}$$

Form the complete stiffness matrix using MathCAD programming:

$$k_2 := k_{\text{percent}} \cdot k_1 \quad k_3 := k_{\text{percent}} \cdot k_2$$

$$\text{row} := 0 \dots \text{contacts} - 1 \quad \text{col} := 0 \dots \text{contacts} - 1$$

$$k_{\text{row, col}} := \begin{cases} k_1 & \text{if row} = \text{col} \\ \text{if row} \neq \text{col} \\ \quad k_2 & \text{if col} = \text{row} + 1 \\ \quad k_2 & \text{if col} = \text{row} - 1 \\ \quad k_3 & \text{if col} = \text{row} + 2 \\ \quad k_3 & \text{if col} = \text{row} - 2 \\ \quad k_2 & \text{if row} = 0 \wedge \text{col} = \text{contacts} - 1 \wedge \text{circle} = 1 \\ \quad k_3 & \text{if row} = 0 \wedge \text{col} = \text{contacts} - 2 \wedge \text{circle} = 1 \\ \quad k_3 & \text{if row} = 1 \wedge \text{col} = \text{contacts} - 1 \wedge \text{circle} = 1 \\ \quad k_2 & \text{if row} = \text{contacts} - 1 \wedge \text{col} = 0 \wedge \text{circle} = 1 \\ \quad k_3 & \text{if row} = \text{contacts} - 1 \wedge \text{col} = 1 \wedge \text{circle} = 1 \\ \quad k_3 & \text{if row} = \text{contacts} - 2 \wedge \text{col} = 0 \wedge \text{circle} = 1 \\ 0 & \text{otherwise} \end{cases}$$

$$k = \begin{pmatrix} 1 & 0.1 & 0.01 & 0 & 0 \\ 0.1 & 1 & 0.1 & 0.01 & 0 \\ 0.01 & 0.1 & 1 & 0.1 & 0.01 \\ 0 & 0.01 & 0.1 & 1 & 0.1 \\ 0 & 0 & 0.01 & 0.1 & 1 \end{pmatrix}$$

Determine the center of stiffness:

$$\text{col_ones}_{\text{row}} := 1 \quad \text{row_zeros}_{0, \text{col}} := 0$$

$$L_{\text{row}} := \text{row} \cdot L_{\text{spacing}}$$

$$L_k := \frac{k^T \cdot \text{col_ones} \cdot L}{k^T \cdot \text{col_ones} \cdot \text{col_ones}} \quad L_k = 5$$

Create stiffness and stiffness x length terms for force and moment equilibrium:

$$K := (k \cdot \text{col_ones})^T \quad KL := \left[k^T \cdot (L - L_k) \right]^T$$

Form geometric constraint equations by maintaining constant slope:

$$\theta_{1,2} = \frac{\delta_2 - \delta_1}{L_2 - L_1} \quad \theta_{2,3} = \frac{\delta_3 - \delta_2}{L_3 - L_2} \quad \dots \quad \theta_{n,n+1} = \frac{\delta_{n+1} - \delta_n}{L_{n+1} - L_n}$$

Solve the following constraint and manipulate to provide slope and C matrices below.

$$\theta_{1,2} = \theta_{2,3} \quad \text{and} \quad \theta_{2,3} = \theta_{3,4} \quad \dots \quad \theta_{n-1,n} = \theta_{n,n+1}$$

$$\text{slope}_{\text{row},\text{col}} := \begin{cases} \text{if } \text{col} = \text{row} + 1 \\ \quad \left| \begin{array}{l} 1 \text{ if } \text{row} = 0 \\ 1 \text{ if } \text{row} > 0 \wedge \text{row} < \text{contacts} - 1 \\ 0 \text{ otherwise} \end{array} \right. \end{cases} \quad \text{slope} = \begin{pmatrix} 0 & 1 & 0 & 0 & 0 \\ 0 & 0 & 1 & 0 & 0 \\ 0 & 0 & 0 & 1 & 0 \\ 0 & 0 & 0 & 0 & 1 \\ 0 & 0 & 0 & 0 & 0 \end{pmatrix}$$

$$C_{\text{row},\text{col}} := \begin{cases} 0 \text{ if } \text{col} < \text{row} \\ \text{slope}_{\text{row},\text{row}+1} \cdot (L_{\text{row}+2} - L_{\text{row}+1}) \text{ if } \text{col} = \text{row} \wedge \text{row} < \text{contacts} - 2 \\ \left[\begin{array}{l} \text{slope}_{\text{row},\text{row}+1} \cdot (L_{\text{row}+2} - L_{\text{row}+1}) \dots \\ + \text{slope}_{\text{row}+1,\text{row}+2} \cdot (L_{\text{row}+1} - L_{\text{row}}) \end{array} \right] \text{ if } \text{col} = \text{row} + 1 \wedge \text{row} < \text{contacts} - 2 \\ \text{slope}_{\text{row}+1,\text{row}+2} \cdot (L_{\text{row}+1} - L_{\text{row}}) \text{ if } \text{col} = \text{row} + 2 \wedge \text{row} < \text{contacts} - 2 \\ 0 \text{ if } \text{col} > \text{row} + 2 \\ 0 \text{ if } \text{row} \geq \text{contacts} - 2 \end{cases}$$

$$C = \begin{pmatrix} 2.5 & -5 & 2.5 & 0 & 0 \\ 0 & 2.5 & -5 & 2.5 & 0 \\ 0 & 0 & 2.5 & -5 & 2.5 \\ 0 & 0 & 0 & 0 & 0 \\ 0 & 0 & 0 & 0 & 0 \end{pmatrix}$$

Combine K, KI, and C matrices into equilibrium equations:

A_{step1} is used to find the applied force and moments.

$$A_{\text{step1}} := \begin{cases} A1 \leftarrow \text{stack}(K, KL) \\ \text{for } i \in 0.. \text{contacts} - 3 \\ \quad A1 \leftarrow \text{stack}(A1, \text{row_zeros}) \\ A1 \end{cases} \quad A_{\text{step1}} = \begin{pmatrix} 1.11 & 1.21 & 1.22 & 1.21 & 1.11 \\ -5.25 & -2.975 & 0 & 2.975 & 5.25 \\ 0 & 0 & 0 & 0 & 0 \\ 0 & 0 & 0 & 0 & 0 \\ 0 & 0 & 0 & 0 & 0 \end{pmatrix}$$

A_{step2} is inverted to find the displacements.

$$A_{\text{step2}} := \begin{cases} A2 \leftarrow \text{stack}(K, KL) \\ \text{for } i \in 0.. \text{contacts} - 3 \\ \quad A2 \leftarrow \text{stack}\left(A2, (C^T)^{(i,T)}\right) \\ A2 \end{cases} \quad A_{\text{step2}} = \begin{pmatrix} 1.11 & 1.21 & 1.22 & 1.21 & 1.11 \\ -5.25 & -2.975 & 0 & 2.975 & 5.25 \\ 2.5 & -5 & 2.5 & 0 & 0 \\ 0 & 2.5 & -5 & 2.5 & 0 \\ 0 & 0 & 2.5 & -5 & 2.5 \end{pmatrix}$$

Create displacement coupling matrix:

$$CC_{\text{row, col}} := \begin{cases} 1 & \text{if row} = \text{col} \\ d_{\text{percent}}^{-(\text{row}-\text{col})} & \text{if row} < \text{col} \wedge |\text{row} - \text{col}| \leq \text{neighbors} \\ d_{\text{percent}}^{(\text{row}-\text{col})} & \text{if row} > \text{col} \wedge |\text{row} - \text{col}| \leq \text{neighbors} \\ 0 & \text{otherwise} \end{cases}$$

$$CC = \begin{pmatrix} 1 & 0.1 & 0.01 & 0 & 0 \\ 0.1 & 1 & 0.1 & 0.01 & 0 \\ 0.01 & 0.1 & 1 & 0.1 & 0.01 \\ 0 & 0.01 & 0.1 & 1 & 0.1 \\ 0 & 0 & 0.01 & 0.1 & 1 \end{pmatrix}$$

Solve force and moment equilibrium equations for applied force:

$$F_{\text{applied}} := A_{\text{step1}} \cdot CC \cdot x \quad F_{\text{applied}} = \begin{pmatrix} -5.716 \\ -7.862 \\ 0 \\ 0 \\ 0 \end{pmatrix}$$

Solve the complete constraint equations for displacement vector:

$$\Delta := A_{\text{step2}}^{-1} \cdot F_{\text{applied}} \quad \Delta = \begin{pmatrix} -0.392 \\ -0.684 \\ -0.975 \\ -1.267 \\ -1.559 \end{pmatrix}$$

Calculate the deflection of each contact due to tolerances:

$$\delta := x - \Delta \quad \delta = \begin{pmatrix} -0.047 \\ 4.653 \times 10^{-3} \\ 0.502 \\ 0.316 \\ -0.127 \end{pmatrix}$$

Calculate the deflection of the center of stiffness:

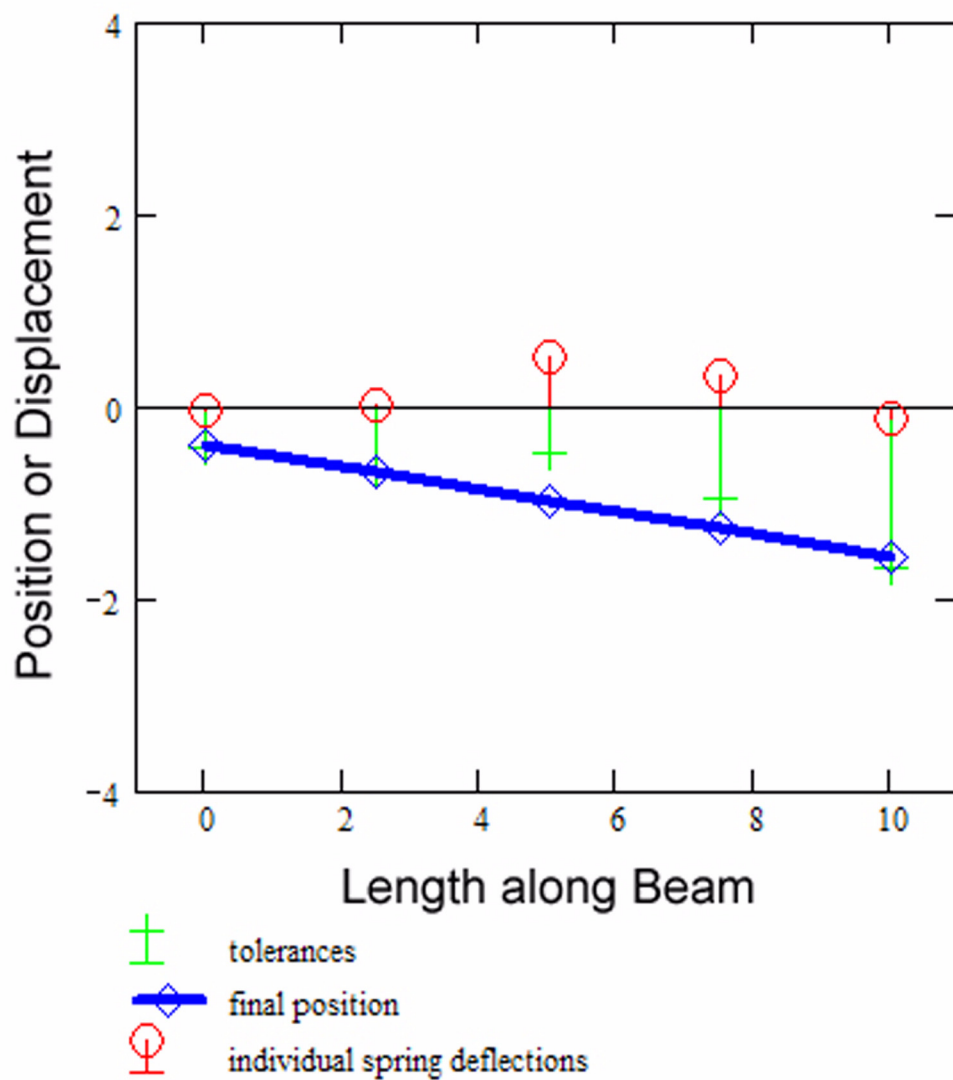
$$\Delta_{k_center} := \frac{\sum \Delta}{\text{contacts}} \quad \Delta_{k_center} = -0.975$$

Calculate the rotation of the beam about the center of stiffness:

$$\theta := \text{atan} \left[\frac{\Delta_{\text{contacts}-1} - \Delta_0}{(\text{contacts} - 1) \cdot L_{\text{spacing}}} \right] \quad \theta = -0.116 \text{ rad} \quad \theta = -6.655 \text{ deg}$$

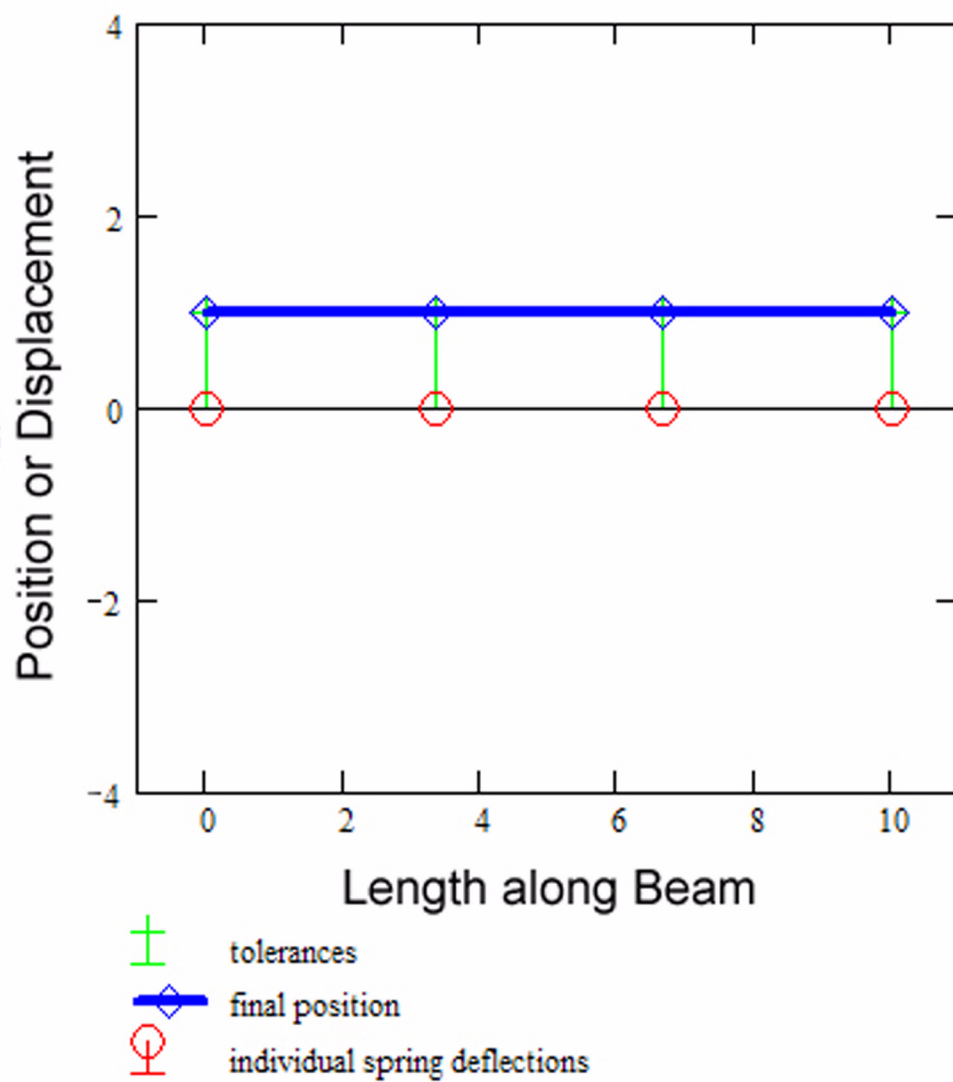
Plot the resulting beam for random distribution:

```
plot := augment(L,x, $\Delta$ , $\delta$ )
```



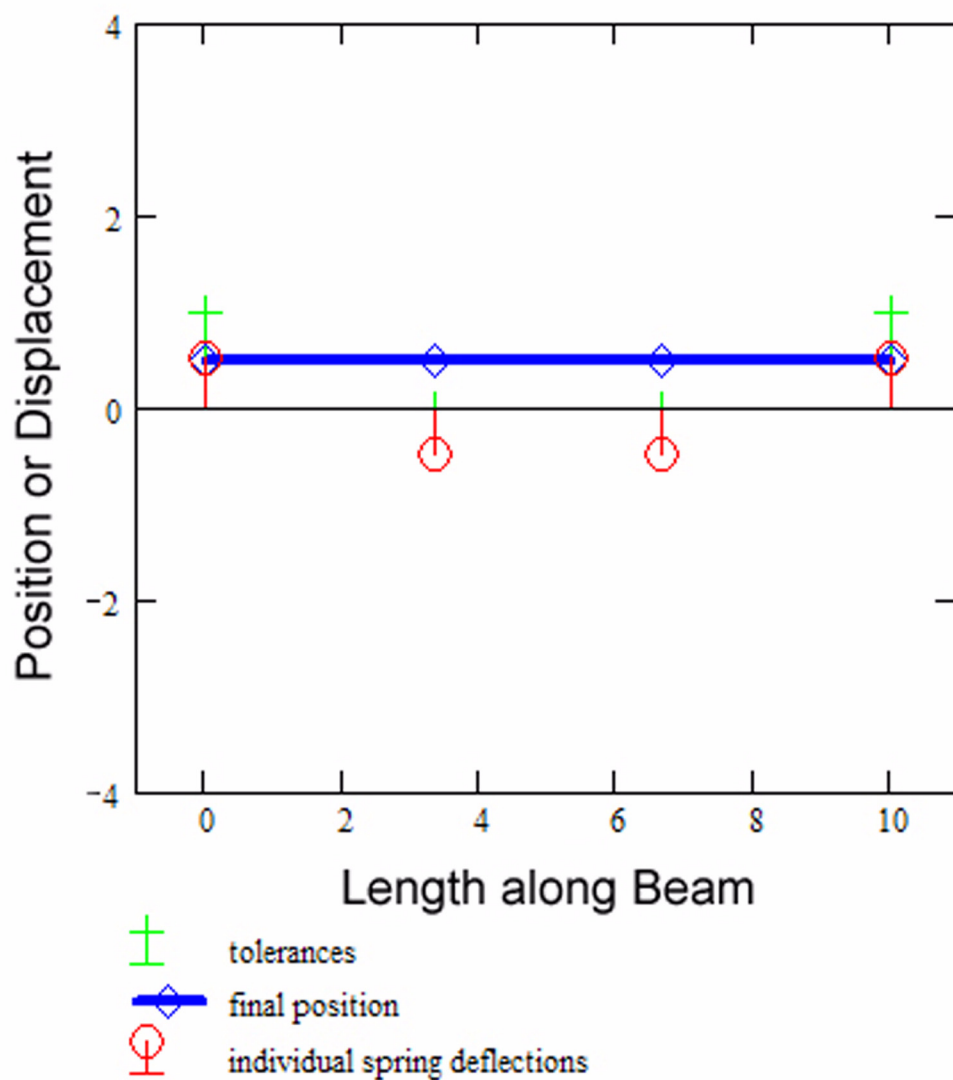
Verification plot for a displacement vector of 1 at each contact:

$$\mathbf{x} = \begin{pmatrix} 1 \\ 1 \\ 1 \\ 1 \end{pmatrix} \quad \Delta = \begin{pmatrix} 1 \\ 1 \\ 1 \\ 1 \end{pmatrix} \quad \delta = \begin{pmatrix} 0 \\ 0 \\ 0 \\ 0 \end{pmatrix} \quad \Delta_{k_center} = 1 \quad \theta = 0\text{-deg}$$



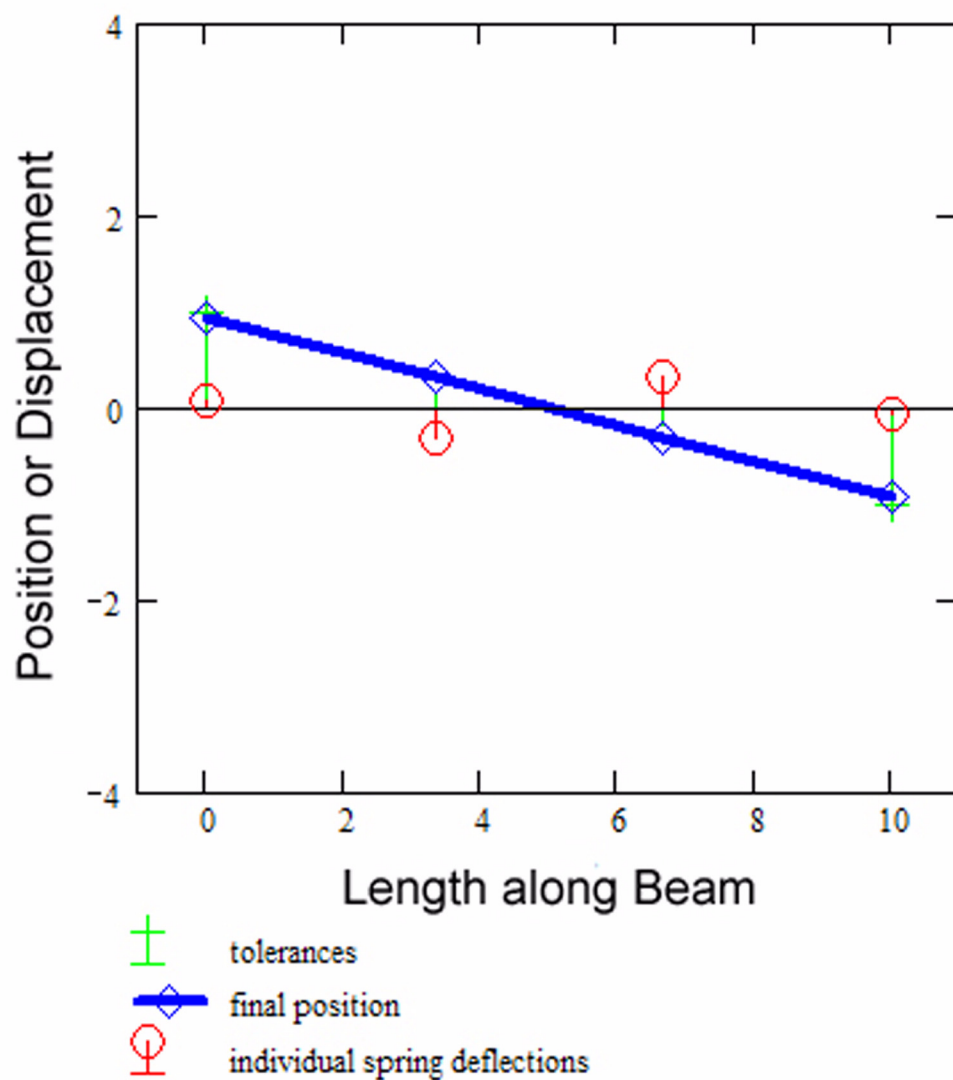
Verification plot for a displacement vector of 1 at each end:

$$\mathbf{x} = \begin{pmatrix} 1 \\ 0 \\ 0 \\ 1 \end{pmatrix} \quad \Delta = \begin{pmatrix} 0.536 \\ 0.536 \\ 0.536 \\ 0.536 \end{pmatrix} \quad \delta = \begin{pmatrix} 0.464 \\ -0.536 \\ -0.536 \\ 0.464 \end{pmatrix} \quad \Delta_{k_center} = 0.536 \quad \theta = 0\text{-deg}$$



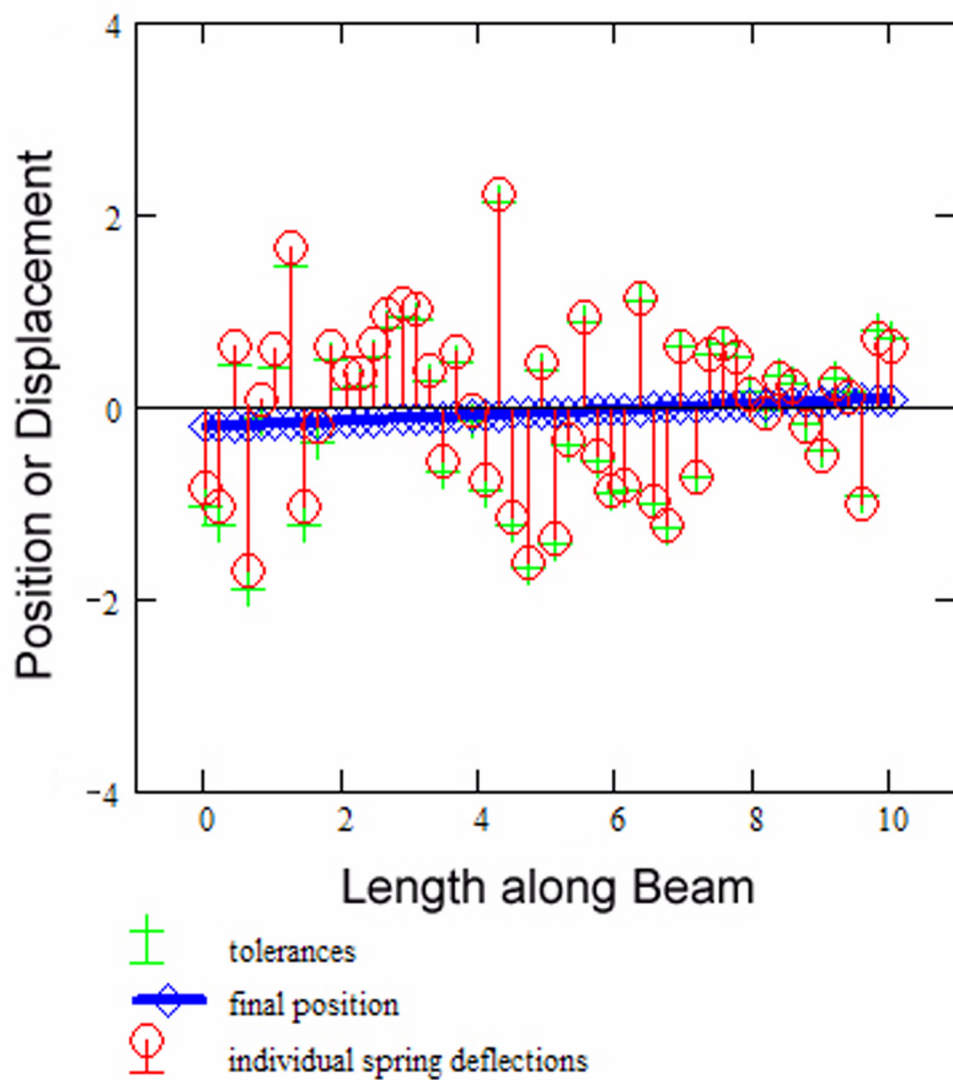
Verification plot for a displacement vector of 1 at one end and -1 at opposite:

$$x = \begin{pmatrix} 1 \\ 0 \\ 0 \\ -1 \end{pmatrix} \quad \Delta = \begin{pmatrix} 0.918 \\ 0.306 \\ -0.306 \\ -0.918 \end{pmatrix} \quad \delta = \begin{pmatrix} 0.082 \\ -0.306 \\ 0.306 \\ -0.082 \end{pmatrix} \quad \Delta_{k_center} = 0 \quad \theta = -10.406\text{-deg}$$



Verification plot for a random displacement vector and 50 contacts:

$$\Delta_{k_center} = -0.068 \quad \theta = 1.698\text{-deg}$$



Appendix C

ANALYSIS FOR AN ELASTICALLY AVERAGED CONNECTOR

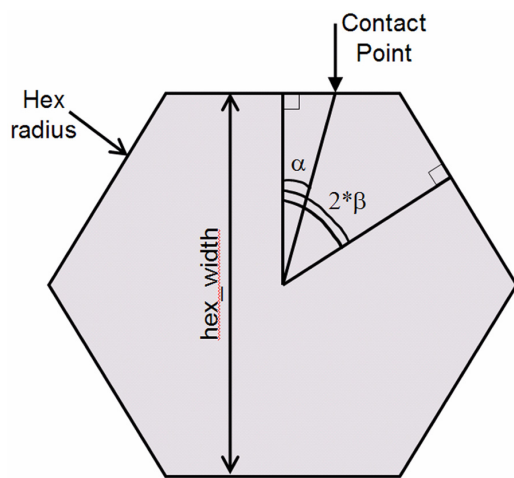


Figure C.1 - Ferrule Dimensions

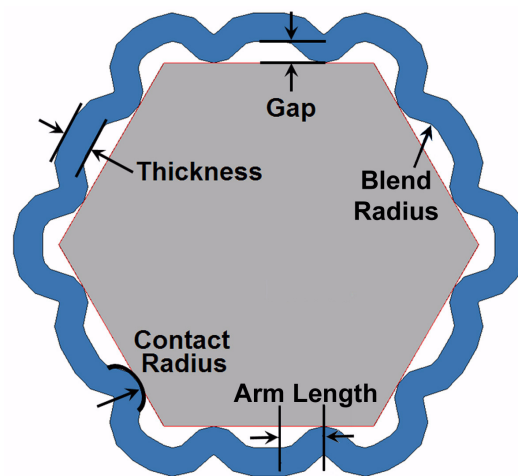


Figure C.2 - Sleeve Dimensions

Specify Geometric Parameters:

`contacts := 12` `n := 0..2contacts - 1`

Specify the nominal geometric parameters for the sleeve and tolerance value ($3^* \sigma$):

`thickness := 2mm` `gap := 2mm` `contact_radius := 2.2mm`
`th_tol := 25μm` `gap_tol := 25μm` `con_tol := 25μm`
`arm_length := 1.5mm` `blend_radius := 1mm`
`arm_tol := 25μm` `blend_tol := 25μm`

Specify the nominal flat-to-flat dimension for a hexagon the fits perfectly into the contact surfaces of the sleeve and tolerance value ($3^* \sigma$):

`sleeve_hex := 0.9822in`
`sleeve_tol := 10μm`

Specify the nominal geometric parameters for the ferrule and tolerance value ($3^* \sigma$):

`αcontact := 19.6627deg` `Δβ := 30deg` `hex_width := 25.0mm`
`αtol := 10-16` `βtol := 10-16` `width_tol := 0.001in`
`radiushex := 106m` `hexagon_length := 1.5in`
`radius_tol := 10-16m` `length_tol := 0.005in`

Material Properties:

Pick a material for the sleeve and ferrule by number:

- 0 - Aluminum
- 1 - Brass 360
- 2 - Magnesium
- 3 - Delrin
- 4 - RC62 Steel
- 5 - Custom1 (Enter values to right)
- 6 - Custom2 (Enter values to right)

`Ecustom1 := 100GPa` `Ecustom2 := 100GPa`
`vcustom1 := 0.3` `vcustom2 := 0.3`
`σy_custom1 := 100MPa` `σy_custom2 := 100MPa`
`μs_custom := 1.0`

`mat_sleeve := 0` `mat_ferrule := 1`

Sleeve Material:

`sleeve_material = "Aluminum"`
`Esleeve = 68.9GPa`
`vsleeve = 0.33`
`σy_sleeve = 145 MPa`
`μs = 0.03`

Ferrule Material:

`ferrule_material = "Brass"`
`Eferrule = 97GPa`
`vferrule = 0.35`
`σy_ferrule = 310MPa`

Form Dimensions into Matrices and Indexable Form:

NOTE: These matrices are highly dependent on part geometry. Any changes to these matrices must be reflected in how the parameters are passed to the rest of the analysis.

Create geometry matrix for sleeve part with tolerances:

```
sleeve := | sleeve2 ← tolerance(contacts, thickness, th_tol)
          | sleeve2 ← augment(sleeve2, tolerance(contacts, gap, gap_tol))
          | sleeve2 ← augment(sleeve2, tolerance(contacts, contact_radius, con_tol))
          | sleeve2 ← augment(sleeve2, tolerance(contacts, arm_length, arm_tol))
          | sleeve2 ← augment(sleeve2, tolerance(contacts, blend_radius, blend_tol))
          | sleeve2 ← augment(sleeve2, tolerance(contacts, sleeve_hex, sleeve_tol))
          | sleeve2
```

Create geometry matrix for ferrule part with tolerances:

$$\alpha_{\text{set}} := \text{tolerance}(1, \alpha_{\text{contact}}, \alpha_{\text{tol}})$$

$$\Delta\beta_{\text{set}} := \text{tolerance}(1, \Delta\beta, \beta_{\text{tol}})$$

$$\text{width} := \frac{\text{tolerance}\left(1, \frac{\text{hex_width}}{2}, \text{width_tol}\right)}{\text{UnitsOf}(\text{hex_width})}$$

$$\text{rad}_{\text{hex}} := \frac{\text{tolerance}(1, \text{radius}_{\text{hex}}, \text{radius_tol})}{\text{UnitsOf}(\text{hex_width})}$$

$$\text{hex_length} := \frac{\text{tolerance}(1, \text{hexagon_length}, \text{length_tol})}{\text{UnitsOf}(\text{hexagon_length})}$$

$$\text{ferrule1} := \begin{pmatrix} 1 & -\alpha_{\text{set}} & 0 \cdot \Delta\beta_{\text{set}} & \text{width} & \text{rad}_{\text{hex}} & \text{hex_length} \\ 2 & \alpha_{\text{set}} & 2 \cdot \Delta\beta_{\text{set}} & \text{width} & \text{rad}_{\text{hex}} & \text{hex_length} \\ 3 & -\alpha_{\text{set}} & 2 \cdot \Delta\beta_{\text{set}} & \text{width} & \text{rad}_{\text{hex}} & \text{hex_length} \\ 4 & \alpha_{\text{set}} & 4 \cdot \Delta\beta_{\text{set}} & \text{width} & \text{rad}_{\text{hex}} & \text{hex_length} \\ 5 & -\alpha_{\text{set}} & 4 \cdot \Delta\beta_{\text{set}} & \text{width} & \text{rad}_{\text{hex}} & \text{hex_length} \\ 6 & \alpha_{\text{set}} & 6 \cdot \Delta\beta_{\text{set}} & \text{width} & \text{rad}_{\text{hex}} & \text{hex_length} \\ 7 & -\alpha_{\text{set}} & 6 \cdot \Delta\beta_{\text{set}} & \text{width} & \text{rad}_{\text{hex}} & \text{hex_length} \\ 8 & \alpha_{\text{set}} & 8 \cdot \Delta\beta_{\text{set}} & \text{width} & \text{rad}_{\text{hex}} & \text{hex_length} \\ 9 & -\alpha_{\text{set}} & 8 \cdot \Delta\beta_{\text{set}} & \text{width} & \text{rad}_{\text{hex}} & \text{hex_length} \\ 10 & \alpha_{\text{set}} & 10 \cdot \Delta\beta_{\text{set}} & \text{width} & \text{rad}_{\text{hex}} & \text{hex_length} \\ 11 & -\alpha_{\text{set}} & 10 \cdot \Delta\beta_{\text{set}} & \text{width} & \text{rad}_{\text{hex}} & \text{hex_length} \\ 12 & \alpha_{\text{set}} & 12 \cdot \Delta\beta_{\text{set}} & \text{width} & \text{rad}_{\text{hex}} & \text{hex_length} \end{pmatrix} +$$

thickness - t gap distance - g contact radius - r_{con}
 arm length - L_{arm} blend radius - r_{blend} sleeve hex - d_{sleeve}
 alpha angle - α beta angle - β ferrule half width - W_{half}
 hex radius - r_{hex}

Stiffness based on Geometry

Run FEA Simulation to map stiffness of a contact point based on critical dimensional parameters. Create a curve fit for the stiffness versus this parameters and input the stiffness as a function of these parameters below.

$$C := 0.1812$$

$$C_{t1} := 3676.6715$$

$$C_{g1} := 0.3257$$

$$C_{rc1} := 0.5677$$

$$C_{arm1} := 1.1901$$

$$C_{rb1} := 0.9157$$

$$C_{t2} := 0.0274$$

$$C_{g2} := 1.2274$$

$$C_{rc2} := 1.1459$$

$$C_{arm2} := 1.0206$$

$$C_{rb2} := 1.0653$$

$$C_{t3} := 1.8863$$

$$C_{g3} := 0.9708$$

$$t1(n) := \frac{(1000 t(n))}{\text{UnitsOf}(t(n))} \quad g1(n) := \frac{(1000 g(n))}{\text{UnitsOf}(g(n))} \quad rc1(n) := \frac{(1000 r_{con}(n))}{\text{UnitsOf}(r_{con}(n))}$$

$$L_{arm1}(n) := \frac{(1000 L_{arm}(n))}{\text{UnitsOf}(L_{arm}(n))} \quad rb1(n) := \frac{(1000 r_{blend}(n))}{\text{UnitsOf}(r_{blend}(n))}$$

$$C_t(n) := C_{t1}^{t1(n)} \cdot C_{t2}^{t1(n)^2} \cdot C_{t3}^{t1(n)^3} \quad C_{rc}(n) := C_{rc1}^{rc1(n)} \cdot C_{rc2}^{rc1(n)^2}$$

$$C_g(n) := C_{g1}^{g1(n)} \cdot C_{g2}^{g1(n)^2} \cdot C_{g3}^{g1(n)^3} \quad C_{arm}(n) := C_{arm1}^{L_{arm1}(n)} \cdot C_{arm2}^{L_{arm1}(n)^2}$$

$$C_{rb}(n) := C_{rb1}^{rb1(n)} \cdot C_{rb2}^{rb1(n)^2}$$

$$k_{geom}(n) := C \cdot C_t(n) \cdot C_g(n) \cdot C_{rc}(n) \cdot C_{arm}(n) \cdot C_{rb}(n) \cdot \frac{N}{\mu m}$$

$$k_{avg_geom} := \frac{\sum_{n=1}^{\text{contacts}} k_{geom}(n)}{\text{contacts}} \quad k_{avg_geom} = 31.004 \frac{N}{\mu m} \quad k_{avg_geom} = 0.177 \frac{lbf}{\mu in}$$

Specify the distance between two parallel hex surfaces from the extruded sleeve:

$$\delta_{ferrule_sleeve}(n) := \frac{2 \cdot W_{half}(n) - d_{sleeve}(n)}{2}$$

Stiffness based on Hertzian Contact of Two Cylinders

This program uses Hertz equations to calculate deflection and stress between two elastic cylinders.
Ref. K. Johnson, 1985.

Radius of curvature:	$R_1(n) := r_{\text{con}}(n)$	$R_2(n) := r_{\text{hex}}(n)$
Depth of reference pt for deflection:	$\text{depth}_1(n) := r_{\text{con}}(n)$	$\text{depth}_2(n) := W_{\text{half}}(n)$
Load f and half length of contact a:	$f(n) := k_{\text{geom}}(n) \cdot \delta_{\text{ferrule_sleeve}}(n)$	$a(n) := \frac{L_{\text{hex}}(n)}{2}$
Calculate the line load.	$P(n) := \frac{f(n)}{2 \cdot a(n)}$	

Calculate the contact modulus.

$$E_c := \left(\frac{1 - \nu_{\text{sleeve}}^2}{E_{\text{sleeve}}} + \frac{1 - \nu_{\text{ferrule}}^2}{E_{\text{ferrule}}} \right)^{-1} \quad E_c = 45.497 \text{ GPa}$$

Calculate the relative radius equivalent to a cylinder on a flat.

$$R_c(n) := \left(R_1(n)^{-1} + R_2(n)^{-1} \right)^{-1}$$

Calculate the half width of contact.

$$b(n) := \sqrt{\frac{4 \cdot P(n) \cdot R_c(n)}{\pi \cdot E_c}}$$

$$\frac{\sum_{n=1}^{\text{contacts}} a(n)}{\sum_{n=1}^{\text{contacts}} b(n)} = 509.938 \quad \frac{\sum_{n=1}^{\text{contacts}} b(n)}{\sum_{n=1}^{\text{contacts}} a(n)} = 1.961 \times 10^{-3}$$

Calculate the max. contact pressure, the max shear stress and its z location below the contact.

$$p_{\text{con}}(n) := \frac{P(n)}{2 \cdot b(n)} \quad p_{\text{max}}(n) := \sqrt{\frac{P(n) \cdot E_c}{\pi \cdot R_c(n)}}$$

$$\tau(n) := 0.3 \cdot p_{\text{max}}(n) \quad z(n) := 0.78 \cdot b(n)$$

$$\tau_{\text{avg}} := \frac{\sum_{n=1}^{\text{contacts}} \tau(n)}{\text{contacts}} \quad z_{\text{avg}} := \frac{\sum_{n=1}^{\text{contacts}} z(n)}{\text{contacts}}$$

$$\tau_{\text{avg}} = 1.159 \times 10^8 \text{ Pa} \quad z_{\text{avg}} = 29.126 \text{ } \mu\text{m}$$

Equivalent ratio between tensile and yield:

$$\sigma_{\text{tensile_ferrule}(n)} := \frac{0.3 P_{\text{max}}(n)}{0.5 \cdot \sigma_{y_ferrule}}$$

$$\sigma_{\text{avg}} := \frac{\sum_{n=1}^{\text{contacts}} \sigma_{\text{tensile_ferrule}(n)}}{\text{contacts}}$$

$$\sigma_{\text{avg}} = 0.748$$

Calculate the normal displacement of each cylinder (approach of distant points).

$$\delta_1(n) := P(n) \cdot \frac{1 - \nu_{\text{sleeve}}^2}{\pi \cdot E_{\text{sleeve}}} \cdot \left(2 \cdot \ln \left(\frac{4 \cdot \text{depth}_1(n)}{b(n)} \right) - 1 \right)$$

$$\delta_2(n) := P(n) \cdot \frac{1 - \nu_{\text{ferrule}}^2}{\pi \cdot E_{\text{ferrule}}} \cdot \left(2 \cdot \ln \left(\frac{4 \cdot \text{depth}_2(n)}{b(n)} \right) - 1 \right)$$

Calculate the normal stiffness.

$$k_{\text{hertz}}(n) := \pi \cdot 2 \cdot a(n) \cdot \left[\frac{1 - (\nu_{\text{sleeve}})^2}{E_{\text{sleeve}}} \cdot \left(2 \cdot \ln \left(\frac{4 \cdot \text{depth}_1(n)}{b(n)} \right) - 1 \right) \dots \right. \\ \left. + \frac{1 - (\nu_{\text{ferrule}})^2}{E_{\text{ferrule}}} \cdot \left(2 \cdot \ln \left(\frac{4 \cdot \text{depth}_2(n)}{b(n)} \right) - 1 \right) - \frac{1}{E_c} \right]^{-1}$$

$$k_{\text{hertz_avg}} := \frac{\sum_{n=1}^{\text{contacts}} k_{\text{hertz}}(n)}{\text{contacts}} \quad k_{\text{hertz_avg}} = 525.68 \frac{\text{N}}{\mu\text{m}}$$

Combined Stiffness

$$k_{\text{total}}(n) := \left(\frac{1}{k_{\text{geom}}(n)} + \frac{1}{k_{\text{hertz}}(n)} \right)^{-1}$$

$$F_{\text{contact}}(n) := k_{\text{total}}(n) \cdot \delta_{\text{ferrule_sleeve}}(n)$$

$$k_{\text{avg_total}} := \frac{\sum_{n=1}^{\text{contacts}} k_{\text{total}}(n)}{\text{contacts}}$$

$$F_{\text{avg_contact}} := \frac{\sum_{n=1}^{\text{contacts}} F_{\text{contact}}(n)}{\text{contacts}}$$

$$k_{\text{avg_total}} = 29.277 \frac{\text{N}}{\mu\text{m}}$$

$$F_{\text{avg_contact}} = 815.506 \text{ N}$$

$$k_{\text{avg_total}} = 0.167 \frac{\text{lbf}}{\mu\text{in}}$$

Elastic Averaging - Equations for Contact Point Geometry:

$$\begin{aligned}
 L_0(n) &:= -W_{\text{half}}(n) \cdot \tan(\alpha(n)) \\
 D_0(n) &:= \sqrt{W_{\text{half}}(n)^2 + L_0(n)^2} \\
 l_1(n, \theta) &:= -W_{\text{half}}(n) \cdot \tan(\alpha(n) - \theta) \\
 d_1(n, \theta) &:= \sqrt{W_{\text{half}}(n)^2 + l_1(n, \theta)^2} \\
 \Delta d(n, \theta) &:= d_1(n, \theta) - D_0(n) \\
 \Delta l(n, \theta) &:= \Delta d(n, \theta) \cdot \frac{\sin(\alpha(n))}{\sin(90\text{-deg} - \theta)} \\
 L_1(n, \theta) &:= \Delta l(n, \theta) + l_1(n, \theta) \\
 D_1(n, \theta) &:= \sqrt{W_{\text{half}}(n)^2 + L_1(n, \theta)^2} \\
 \alpha_1(n, \theta) &:= -\text{atan}\left(\frac{L_1(n, \theta)}{W_{\text{half}}(n)}\right) + \theta \\
 \delta_y(n, \theta) &:= \Delta d(n, \theta) \cdot \frac{\sin(90\text{deg} + \theta - \alpha(n))}{\sin(90\text{-deg} - \theta)} \\
 L_{1\text{full}}_n &:= \begin{cases} L_1\left(\frac{n+1}{2}, 0\right) & \text{if } \text{mod}(n, 2) > 0 \\ 0\text{mm} & \text{otherwise} \end{cases} \quad L_{1\text{KL}}_n := \begin{cases} L_1\left(\frac{n+1}{2}, 0\right) & \text{if } \text{mod}(n, 2) > 0 \\ L_1\left(\frac{n+2}{2}, 0\right) & \text{otherwise} \end{cases}
 \end{aligned}$$

Setup Stiffness and Transformation Matrices:

$$\begin{aligned}
 \text{row} &:= 0.. \text{contacts} - 1 & \text{col_ones}_n &:= 1 \\
 \text{col} &:= 0.. \text{contacts} - 1 & \text{row_zeros}_{0, 2 \cdot \text{contacts} - 1} &:= 0 \\
 \text{row2} &:= 0.. 2 \cdot \text{contacts} - 1 \\
 \text{xy} &:= \begin{cases} \text{xy2} \leftarrow \begin{pmatrix} 1 & 0 \\ 0 & 1 \end{pmatrix} \\ \text{for } i \in 1.. \text{contacts} - 1 \\ \text{xy2} \leftarrow \text{augment}\left[\text{xy2}, \begin{pmatrix} 1 & 0 \\ 0 & 1 \end{pmatrix}\right] \\ \text{xy2} \end{cases} & \Delta(\Delta x, \Delta y) &:= \begin{cases} \Delta 2 \leftarrow \begin{pmatrix} \Delta x \\ \Delta y \end{pmatrix} \\ \text{for } i \in 1.. \text{contacts} - 1 \\ \Delta 2 \leftarrow \text{stack}\left[\Delta 2, \begin{pmatrix} \Delta x \\ \Delta y \end{pmatrix}\right] \\ \Delta 2 \end{cases} \\
 \text{xstrip} &:= \begin{cases} \text{xstrip2} \leftarrow \begin{pmatrix} 1 \\ 0 \end{pmatrix} \\ \text{for } i \in 1.. \text{contacts} - 1 \\ \text{xstrip2} \leftarrow \text{stack}\left[\text{xstrip2}, \begin{pmatrix} 1 \\ 0 \end{pmatrix}\right] \\ \text{xstrip2} \end{cases} & \text{ystrip} &:= \begin{cases} \text{ystrip2} \leftarrow \begin{pmatrix} 0 \\ 1 \end{pmatrix} \\ \text{for } i \in 1.. \text{contacts} - 1 \\ \text{ystrip2} \leftarrow \text{stack}\left[\text{ystrip2}, \begin{pmatrix} 0 \\ 1 \end{pmatrix}\right] \\ \text{ystrip2} \end{cases}
 \end{aligned}$$

Setup Stiffness and Transformation Matrices:

```

row := 0..contacts - 1      col_ones_n := 1
col := 0..contacts - 1      row_zeros_0,2,contacts-1 := 0
row2 := 0..2*contacts - 1

xy := | xy2 ← ( 1 0 )
      | ( 0 1 )
      | for i ∈ 1..contacts - 1
      | xy2 ← augment[ xy2, ( 1 0 ) ]
      | ( 0 1 )
      | xy2

Δ(Δx,Δy) := | Δ2 ← ( Δx )
              | ( Δy )
              | for i ∈ 1..contacts - 1
              | Δ2 ← stack[ Δ2, ( Δx ) ]
              | ( Δy )
              | Δ2

xstrip := | xstrip2 ← ( 1 )
           | ( 0 )
           | for i ∈ 1..contacts - 1
           | xstrip2 ← stack[ xstrip2, ( 1 ) ]
           | ( 0 )
           | xstrip2

ystrip := | ystrip2 ← ( 0 )
           | ( 1 )
           | for i ∈ 1..contacts - 1
           | ystrip2 ← stack[ ystrip2, ( 0 ) ]
           | ( 1 )
           | ystrip2

```

Noncoupled Stiffness:

$$k_{nc}(n) := \begin{pmatrix} k_{total}(n) & 0 \\ 0 & 0 \end{pmatrix} \quad k(n) = \begin{pmatrix} \text{"x-x stiffness"} & \text{"x-y stiffness"} \\ \text{"x-y stiffness"} & \text{"y-y stiffness"} \end{pmatrix}$$

Transformation Matrix for One Contact Point:

$$T(n) := \begin{pmatrix} \sin(\beta(n)) & \cos(\beta(n)) \\ -\cos(\beta(n)) & \sin(\beta(n)) \end{pmatrix}$$

$$Kx_0 := 60.19$$

$$Kx_4 := 3.908$$

$$Kx_8 := 0$$

$$Kx_1 := 11.91$$

$$Kx_5 := -0.003$$

$$Kx_9 := 0.007$$

$$Kx_2 := -0.020$$

$$Kx_6 := -0.005$$

$$Kx_10 := 0.01$$

$$Kx_3 := -0.005$$

$$Kx_7 := 0.003$$

$$Kx_11 := 32.745$$

$$Ky_0 := -0.202$$

$$Ky_4 := 13.322$$

$$Ky_8 := -0.406$$

$$Ky_1 := 38.056$$

$$Ky_5 := 3.766$$

$$Ky_9 := -9.054$$

$$Ky_2 := 24.933$$

$$Ky_6 := 6.462$$

$$Ky_10 := -13.483$$

$$Ky_3 := 7.518$$

$$Ky_7 := -3.606$$

$$Ky_11 := -14.255$$

Prepare full stiffness, length, and other internal matrices:

$$K_{\text{local_nc}} := \begin{cases} \begin{pmatrix} 0 & 0 \\ 0 & 0 \end{pmatrix} \frac{N}{\mu\text{m}} & \text{if row} \neq \text{col} \\ k_{\text{nc}}(\text{row} + 1) & \text{if row} = \text{col} \end{cases} \quad T_{\text{row, col}} := \begin{cases} \begin{pmatrix} 0 & 0 \\ 0 & 0 \end{pmatrix} & \text{if row} \neq \text{col} \\ T(\text{row} + 1) & \text{if row} = \text{col} \end{cases}$$

$$K_{\text{local_nc}} := \text{UnStack}(K_{\text{local_nc}}) \quad T := \text{UnStack}(T)$$

$$\text{CR} := \text{stack}(\text{KR1}, \text{KR2}, \text{KR3}, \text{KR4}, \text{KR5}, \text{KR6}, \text{KR7}, \text{KR8}, \text{KR9}, \text{KR10}, \text{KR11}, \text{KR12})$$

$$\text{KR} := \frac{\text{CR}^{-1}}{\left(\text{CR}^{-1}\right)_{0,0}}$$

$$K_{\text{local}} := \text{KR} \cdot K_{\text{local_nc}}$$

$$K_{\text{global}} := T^T \cdot K_{\text{local}} \cdot T \quad K_{\text{global_nc}} := T^T \cdot K_{\text{local_nc}} \cdot T$$

$$T_{\text{k}(n)} := \begin{pmatrix} -\cos(\beta(n)) & \sin(\beta(n)) \\ \sin(\beta(n)) & \cos(\beta(n)) \end{pmatrix}$$

$$T_{\text{k}_{\text{row, col}}} := \begin{cases} \begin{pmatrix} 0 & 0 \\ 0 & 0 \end{pmatrix} & \text{if row} \neq \text{col} \\ T_{\text{k}}(\text{row} + 1) & \text{if row} = \text{col} \end{cases}$$

$$T_{\text{k}} := \text{UnStack}(T_{\text{k}})$$

$$L_{\text{k}} := T_{\text{k}}^T \cdot L_{1\text{full}}$$

Define Tolerance and Nominal Deflections in Local Coordinates:

Note: x-direction is along length of spring and y-direction is normal to spring

$$u_x(n) := \delta_{\text{ferrule_sleeve}}(n) + \delta_y(n, 0)$$

$$u_y(n) := 0 \cdot m$$

Convert individual contact deflections into a column vector containing x and y local deflections.

$$u_{\text{local}}_{\text{row2}} := \begin{cases} u_x \left(\frac{\text{row2}}{2} + 1 \right) & \text{if } \text{mod}(\text{row2}, 2) = 0 \\ u_y \left(\frac{\text{row2} + 1}{2} \right) & \text{if } \text{mod}(\text{row2}, 2) > 0 \end{cases} \quad u_{\text{global}} := T^T u_{\text{local}}$$

Define Forces and Stiffness in Local and Global Coordinates:

Basic force equation for a contact point including deflection applied to common part and those defined above (excludes coupling):

$$F(n, \Delta x, \Delta y, \theta) := k_{\text{total}}(n) \cdot (\Delta x \cdot \sin(\beta(n)) + \Delta y \cdot \cos(\beta(n)) - u_x(n))$$

Forces in local coordinates and matrix form for each contact spring for a defined common deflection:

$$f_{\text{local}}(\Delta x, \Delta y) := K_{\text{local}} \cdot T \cdot \Delta(\Delta x, \Delta y) - K_{\text{local}} \cdot u_{\text{local}}$$

Forces in global coordinates and matrix form for each contact spring for a defined common deflection:

$$f_{\text{global}}(\Delta x, \Delta y) := T^T \cdot f_{\text{local}}(\Delta x, \Delta y)$$

Forces in global coordinates and matrix form for common part for a defined common deflection:

$$F_{xy}(\Delta x, \Delta y) := xy \cdot f_{\text{global}}(\Delta x, \Delta y)$$

Form Force and Moment Equilibrium Equations:

$$K := \left((K_{\text{global}})^T \cdot \text{augment}(x_{\text{strip}}, y_{\text{strip}}) \right)^T$$

$$K_x := (K^T)^{\langle 0 \rangle} \quad K_{xx} := \sum K_x \quad K_{xx} = 72.786 \frac{\text{N}}{\mu\text{m}}$$

$$K_y := (K^T)^{\langle 1 \rangle} \quad K_{yy} := \sum K_y \quad K_{yy} = 72.202 \frac{\text{N}}{\mu\text{m}}$$

$$KL := -\left[T^T \cdot (K_{\text{local}}^T \cdot L_{1KL}) \right]^T \quad KL2 := \left[T^T \cdot (K_{\text{local}}^T \cdot L_{1KL}^2) \right]$$

$$A_{\text{step1}} := \text{stack} \left(\frac{-K \cdot m}{N}, \frac{-KL}{N} \right)$$

Solve for Applied Forces:

$$F_{app} := A_{step1} \cdot \frac{u_{global}}{m}$$

$$\begin{array}{lll} F_x := F_{app_0} \text{ N} & F_y := F_{app_1} \text{ N} & M_z := F_{app_2} \text{ N}\cdot\text{m} \\ F_x = 42.657 \text{ N} & F_y = -7.55 \text{ N} & M_z = 1.028 \text{ N}\cdot\text{m} \end{array}$$

Center of stiffness:

$$x_k := \frac{K_x \cdot L_k}{\sum K_x} \quad x_k = 6.299 \mu\text{m}$$

$$y_k := \frac{K_y \cdot L_k}{\sum K_y} \quad y_k = -33.35 \mu\text{m}$$

Initial Offset Position of Common Part due to Tolerances:

$$\Delta x_{initial} := \frac{F_x}{K_{xx}} \quad \Delta y_{initial} := \frac{F_y}{K_{yy}}$$

$$\Delta x_{initial} = 0.586 \mu\text{m} \quad \Delta y_{initial} = -0.105 \mu\text{m}$$

$$\theta_{initial} := \frac{M_z}{\sum KL^2 \cdot m} \quad \theta_{initial} = 4.898 \times 10^{-3} \text{ deg}$$

$$\pi - \theta_{initial} = 179.995 \text{ deg}$$

Friction Forces for Removal or Insertion under No Disturbance:

$$F_{remove} := \left| \mu_s \cdot \sum_{n=1}^{\text{contacts}} F(n, 0\text{mm}, 0\text{mm}, 0) \right|$$

$$F_{remove} = 293.582 \text{ N} \quad F_{remove} = 66 \text{ lbf}$$

Kinetic Coefficient of Friction:

$$\mu_k := 0.03$$

$$F_{sliding} := \left| \mu_k \cdot \sum_{n=1}^{\text{contacts}} F(n, 0\text{mm}, 0\text{mm}, 0) \right|$$

$$F_{sliding} = 293.582 \text{ N} \quad F_{sliding} = 66 \text{ lbf}$$

Fiber Optic Power Loss:

$$d := 62.5 \mu\text{m}$$

$$n_0 := 1.00027$$

$$NA := 0.275$$

$$FD := 5 \text{mm}$$

$$\delta := \sqrt{\Delta x_{\text{initial}}^2 + \Delta y_{\text{initial}}^2}$$

$$\delta = 1.061 \mu\text{m}$$

$$\theta := \frac{2 \cdot \delta}{\text{hexagon_length}}$$

$$\delta_{\text{end}} := \delta + |FD \cdot \sin(\theta_{\text{initial}})|$$

$$\delta_{\text{end}} = 14.75 \mu\text{m}$$

Loss at center of connector:

$$e := \left(1 - \frac{\delta^2}{d^2}\right)^{0.5} \quad e = 1$$

$$L_{\text{lateral}} := -10 \cdot \log \left[\frac{2}{\pi} \cdot \left(\text{atan} \left(\frac{d \cdot e}{\delta} \right) - \frac{\delta \cdot e}{d} \right) \right]$$

$$L_{\text{lateral}} = 0.095 \text{ dB}$$

Loss at outer edge of connector (dimension FD):

$$e_{\text{tilt}} := \left(1 - \frac{\delta_{\text{end}}^2}{d^2}\right)^{0.5} \quad e_{\text{tilt}} = 0.972$$

$$L_{\text{lateral_tilt}} := -10 \cdot \log \left[\frac{2}{\pi} \cdot \left(\text{atan} \left(\frac{d \cdot e}{\delta_{\text{end}}} \right) - \frac{\delta_{\text{end}} \cdot e_{\text{tilt}}}{d} \right) \right]$$

$$L_{\text{lateral_tilt}} = 1.509 \text{ dB}$$

$$L_{\text{angular}} := -10 \cdot \log \left(1 - \frac{n_0 \cdot \theta}{\pi \cdot NA} \right)$$

$$L_{\text{angular}} = 2.801 \times 10^{-4} \text{ dB}$$

Appendix D

MATHEMATICS FOR PRELOAD BEAM

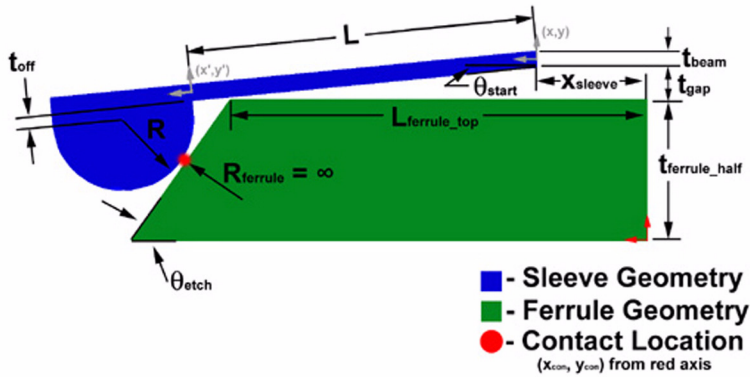
The following mathematics describe the deflection of the preload beam, assuming it is a cantilever beam following traditional small deflection beam equations.

Removal Force carried over from Elastic Averaging Model:

Reference: D:\SIMP\connector\connector_analysis\EA.mcc

$$F_{\text{remove}} = 256.966 \text{ N} \quad F_{\text{remove}} = 57.768 \text{ lbf}$$

Preload Beam Equations



Basic Geometric Parameters:

Sleeve Parameters:

Offset to contact center: $t_{\text{off}} := 0.2 \text{ mm}$

Nominal straight length of beam: $L := 5 \text{ mm}$

Radius of contact curve: $R_{\text{sleeve}} := 3 \text{ mm}$

Width of contact beam: (check for space!) $w_{\text{beam}} := 2 \text{ mm}$

Starting angle of beam: $\theta_{\text{start}} := 5.5 \text{ deg}$

Ferrule:

Angle of etched surfaces: $\theta_{\text{etch}} := 54.7 \text{ deg}$

Radius of ferrule contact: $R_{\text{ferrule}} := \infty \text{ m}$
(∞ for flat)

$$\delta_{\text{beam}} := \text{hex_width} - \text{sleeve_hex}$$

$$\text{th} := \text{thickness}$$

Various Calculated Parameters:

$$\theta_{\text{diff}} := \theta_{\text{etch}} - \theta_{\text{start}}$$

$$A := w_{\text{beam}} \cdot \text{th}$$

$$I := \frac{1}{12} \cdot w_{\text{beam}} \cdot \text{th}^3$$

$$y_{\text{sleeve}} := t_{\text{ferrule_half}} + t_{\text{gap}} + \frac{\text{th}}{2 \cdot \cos(\theta_{\text{start}})}$$

$$y_{\text{sleeve}} = 15.531 \text{ mm}$$

$$t_{\text{ferrule_half}} := \frac{\text{hex_width}}{2}$$

$$t_{\text{gap}} := \text{gap} + \frac{\delta_{\text{beam}}}{2}$$

$$t_{\text{gap}} = 2.026 \text{ mm}$$

$$t_{\text{short}} := \frac{\text{th}}{2} + t_{\text{off}}$$

Solve force vs. deflection angle equations:

Initial conditions:

$$\theta_{\text{defl}} := 1 \text{ deg}$$

$$C_x := \sin(\theta_{\text{diff}} - \theta_{\text{defl}}) + \mu_s \cdot \cos(\theta_{\text{diff}} - \theta_{\text{defl}})$$

$$C_y := \cos(\theta_{\text{diff}} - \theta_{\text{defl}}) - \mu_s \cdot \sin(\theta_{\text{diff}} - \theta_{\text{defl}})$$

$$F_{\text{beam}} := \frac{F_{\text{remove}}}{2 \cdot \cos(\theta_{\text{etch}})}$$

$$TOL := 0.0001 \mu\text{m}$$

$$CTOL := 0.0001 \mu\text{m}$$

Solving Block:

Given

$$C_x = \sin(\theta_{\text{diff}} - \theta_{\text{defl}}) + \mu_s \cdot \cos(\theta_{\text{diff}} - \theta_{\text{defl}})$$

$$C_y = \cos(\theta_{\text{diff}} - \theta_{\text{defl}}) - \mu_s \cdot \sin(\theta_{\text{diff}} - \theta_{\text{defl}})$$

$$\theta_{\text{defl}} = \frac{F_{\text{beam}} \cdot L}{2 \cdot E_{\text{sleeve}} \cdot I} \left[2 \cdot C_y \cdot [R_{\text{sleeve}} \cdot (1 - \sin(\theta_{\text{diff}} - \theta_{\text{defl}}))] \dots \right. \\ \left. + -2 \cdot C_x \cdot \left(\frac{th}{2} + t_{\text{off}} + R_{\text{sleeve}} \cdot \cos(\theta_{\text{diff}} - \theta_{\text{defl}}) \right) + C_y \cdot L \right]$$

$$\text{solution} := \text{Find}(\theta_{\text{defl}}, C_x, C_y)$$

$$\theta_{\text{defl}} := \text{solution}_0$$

$$C_x := \text{solution}_1$$

$$C_y := \text{solution}_2$$

Slope at end of beam:

$$\theta_{\text{defl}} = 3.247 \text{ deg}$$

Frictional and angular coefficients:

$$C_x = 0.74$$

$$C_y = 0.674$$

Determine geometric parameters:

$$x'_c := R_{\text{sleeve}} \cdot (1 - \sin(\theta_{\text{diff}} - \theta_{\text{defl}}))$$

$$y'_c := -\left(\frac{th}{2} + t_{\text{off}} + R_{\text{sleeve}} \cdot \cos(\theta_{\text{diff}} - \theta_{\text{defl}}) \right)$$

$$y_{\text{defl}} := \frac{F_{\text{beam}} \cdot L^2}{6 \cdot E_{\text{sleeve}} \cdot I} \cdot (3 \cdot C_y \cdot x'_c - 3 \cdot C_x \cdot y'_c + 2 \cdot C_y \cdot L)$$

$$\Delta L := \frac{20 \cdot (C_y \cdot F_{\text{beam}} \cdot x'_c - C_x \cdot F_{\text{beam}} \cdot y'_c)^2 \cdot L^3 \dots \\ + 25 \cdot C_y \cdot F_{\text{beam}} \cdot (C_y \cdot F_{\text{beam}} \cdot x'_c - C_x \cdot F_{\text{beam}} \cdot y'_c) \cdot L^4 + 8 \cdot (C_y \cdot F_{\text{beam}})^2 \cdot L^5}{120 \cdot E_{\text{sleeve}} \cdot I^2}$$

$$y_{\text{con}} := y_{\text{sleeve}} - \left[R_{\text{sleeve}} \cdot \cos(\theta_{\text{etch}}) + t_{\text{short}} \cdot \cos(\theta_{\text{start}} - \theta_{\text{defl}}) + R_{\text{sleeve}} \cdot \sin(\theta_{\text{start}} - \theta_{\text{defl}}) \dots \right. \\ \left. + (L - \Delta L) \cdot \sin(\theta_{\text{start}} - \theta_{\text{defl}}) + y_{\text{defl}} \cdot \cos(\theta_{\text{start}} - \theta_{\text{defl}}) \right]$$

$$x_{\text{con}} := \text{hexagon_length} + \frac{t_{\text{ferrule_half}} - y_{\text{con}}}{\tan(\theta_{\text{etch}})}$$

$$x_{\text{sleeve}} := x_{\text{con}} + R_{\text{sleeve}} \cdot \sin(\theta_{\text{etch}}) + t_{\text{short}} \cdot \sin(\theta_{\text{start}} - \theta_{\text{defl}}) \dots \\ + -R_{\text{sleeve}} \cdot \cos(\theta_{\text{start}} - \theta_{\text{defl}}) - (L - \Delta L) \cdot \cos(\theta_{\text{start}} - \theta_{\text{defl}}) - y_{\text{defl}} \cdot \sin(\theta_{\text{start}} - \theta_{\text{defl}})$$

Location of contact point in x', y' coordinates: $x'_c = 0.844 \text{ mm}$ $y'_c = -3.286 \text{ mm}$

Y deflection of contact point due to beam bending: $y_{\text{defl}} = 158.656 \mu\text{m}$

Change in length due to beam bending: $\Delta L = 3.192 \mu\text{m}$

Location of contact point from red coordinates (fiber location): $x_{\text{con}} = 38.365 \text{ mm}$ $y_{\text{con}} = 12.125 \text{ mm}$

Distance between start of beam and flat contact surface of ferrule: $x_{\text{sleeve}} = 32.864 \text{ mm}$

Determine Forces in x' and y' Frames:

$$F'_x := C_x \cdot F_{\text{beam}} \quad F'_x = 164.451 \text{ N}$$

$$F'_y := C_y \cdot F_{\text{beam}} \quad F'_y = 149.789 \text{ N}$$

$$M' := F'_y \cdot x'_c - F'_x \cdot y'_c \quad M' = 0.667 \text{ N}\cdot\text{m}$$

Double check that Vector Loop and Bending Equations are Satisfied:

$$\begin{aligned} x_{\text{check}} := & -x_{\text{sleeve}} + \left(\text{hexagon_length} + \frac{t_{\text{ferrule_half}} - y_{\text{con}}}{\tan(\theta_{\text{etch}})} \right) + R_{\text{sleeve}} \cdot \sin(\theta_{\text{etch}}) \dots \\ & + \left(\frac{th}{2} + t_{\text{off}} \right) \cdot \sin(\theta_{\text{start}} - \theta_{\text{defl}}) + -R_{\text{sleeve}} \cdot \cos(\theta_{\text{start}} - \theta_{\text{defl}}) \dots \\ & + -(L - \Delta L) \cdot \cos(\theta_{\text{start}} - \theta_{\text{defl}}) - y_{\text{defl}} \cdot \sin(\theta_{\text{start}} - \theta_{\text{defl}}) \end{aligned}$$

$$\begin{aligned} y_{\text{check}} := & -y_{\text{sleeve}} + y_{\text{con}} + R_{\text{sleeve}} \cdot \cos(\theta_{\text{etch}}) + \left(\frac{th}{2} + t_{\text{off}} \right) \cdot \cos(\theta_{\text{start}} - \theta_{\text{defl}}) \dots \\ & + R_{\text{sleeve}} \cdot \sin(\theta_{\text{start}} - \theta_{\text{defl}}) + (L - \Delta L) \cdot \sin(\theta_{\text{start}} - \theta_{\text{defl}}) + y_{\text{defl}} \cdot \cos(\theta_{\text{start}} - \theta_{\text{defl}}) \end{aligned}$$

$$y_{\text{defl_check}} := \frac{F_{\text{beam}} \cdot L^2}{6 \cdot E_{\text{sleeve}} \cdot I} \cdot (3 \cdot C_y \cdot x'_c - 3 \cdot C_x \cdot y'_c + 2 \cdot C_y \cdot L) - y_{\text{defl}}$$

$$\theta_{\text{check}} := \frac{L}{2 \cdot E_{\text{sleeve}} \cdot I} \cdot (2 \cdot M' + F'_y \cdot L) - \theta_{\text{defl}}$$

$$L_{\text{check}} := \frac{20 \cdot M'^2 \cdot L^3 + 25 \cdot F'_y \cdot M' \cdot L^4 + 8 \cdot F'_y{}^2 \cdot L^5}{120 \cdot E_{\text{sleeve}}{}^2 \cdot I^2} - \Delta L$$

$$\text{status} := \begin{cases} \text{"bad"} & \text{if } |x_{\text{check}}| > 1 \mu\text{m} \\ \text{"bad"} & \text{if } |y_{\text{check}}| > 1 \mu\text{m} \\ \text{"bad"} & \text{if } |y_{\text{defl_check}}| > 1 \mu\text{m} \\ \text{"bad"} & \text{if } |\theta_{\text{check}}| > 10^{-6} \text{ deg} \\ \text{"bad"} & \text{if } |L_{\text{check}}| > 1 \mu\text{m} \\ \text{"good"} & \text{otherwise} \end{cases}$$

$$x_{\text{check}} = 2.602 \times 10^{-12} \mu\text{m}$$

$$y_{\text{check}} = -6.505 \times 10^{-13} \mu\text{m}$$

$$y_{\text{defl_check}} = 0 \mu\text{m}$$

$$\theta_{\text{check}} = 0 \text{ deg}$$

$$L_{\text{check}} = 0 \mu\text{m}$$

status = "good"

Compare to standard beam bending limits:

$$y_{\max} := \frac{F'_y \cdot L^3}{3 \cdot E_{\text{sleeve}} \cdot I} + \frac{M' \cdot L^2}{E_{\text{sleeve}} \cdot I}$$

$$y_{\max} = 249.374 \mu\text{m}$$

$$\frac{F'_y \cdot L^3}{3 \cdot E_{\text{sleeve}} \cdot I} = 67.938 \mu\text{m}$$

$$\frac{M' \cdot L^2}{E_{\text{sleeve}} \cdot I} = 181.437 \mu\text{m}$$

Stiffness of Beam:

$$k_{x_prime} := \frac{F_{\text{beam}}}{\Delta L} \quad k_{x_prime} = 69.657 \frac{\text{N}}{\mu\text{m}}$$

$$k_{y_prime} := \frac{F_{\text{beam}}}{y_{\text{defl}}} \quad k_{y_prime} = 1.401 \frac{\text{N}}{\mu\text{m}} \quad +$$

$$k_{\theta_prime} := \frac{F_{\text{beam}}}{\theta_{\text{defl}}} \quad k_{\theta_prime} = 3.924 \times 10^3 \frac{\text{N}}{\text{rad}}$$

Check Stress from Bending Moment:

$$\sigma := \frac{M' \cdot \frac{t_h}{2}}{I} \quad \sigma = 500.04 \text{ MPa}$$

$$\frac{\sigma}{\sigma_{y_sleeve}} = 344.855 \%$$

Check Axial Elongation of Beam:

$$\delta := \frac{F'_x \cdot L}{A \cdot E_{\text{sleeve}}}$$

$$\delta = 2.984 \mu\text{m}$$

$$\frac{\delta}{L} = 5.967 \times 10^{-4}$$

$$\frac{\delta}{\Delta L} = 0.935$$

Hertzian Stress at Contact Point of Preload Beam:

Compute equivalent radius

$$R_{C2} := \left(\frac{1}{R_{\text{sleeve}}} + \frac{1}{R_{\text{ferrule}}} \right)^{-1}$$

$$R_{C2} = 3 \text{ mm}$$

Half width of contact b

$$F' := \frac{F_{\text{beam}}}{w_{\text{beam}}} \quad F' = 111.172 \frac{\text{N}}{\text{mm}} \quad b := \sqrt{\frac{4 \cdot F' \cdot R_{C2}}{\pi \cdot E_C}} \quad b = 96.61 \mu\text{m}$$

Calculate the max. contact pressure, the max shear stress and its z location below the contact.

$$p := \frac{2 \cdot F'}{\pi \cdot b} \quad p = 732.574 \text{ MPa} \quad p = 74.702 \text{ HBn}$$

$$\tau := 0.3 \cdot p \quad \tau = 219.772 \text{ MPa} \quad \text{Equivalent tensile:}$$

$$z := 0.78 \cdot b \quad z = 0.075 \text{ mm} \quad \tau \sqrt{3} = 380.656 \text{ MPa} \quad \frac{\tau}{2 \cdot \sigma_{y_{\text{sleeve}}}} = 0.758$$

Calculate the normal displacement of each cylinder (approach of distant points).

$$d1_{\text{beam}} := R_{\text{sleeve}} \quad d2_{\text{beam}} := d1_{\text{beam}}$$

$$\delta_1 := F' \cdot \frac{1 - \nu_{\text{sleeve}}^2}{\pi \cdot E_{\text{sleeve}}} \cdot \left(2 \cdot \ln \left(\frac{4 \cdot d1_{\text{beam}}}{b} \right) - 1 \right) \quad \delta_1 = 3.956 \mu\text{m}$$

$$\delta_2 := F' \cdot \frac{1 - \nu_{\text{ferrule}}^2}{\pi \cdot E_{\text{ferrule}}} \cdot \left(2 \cdot \ln \left(\frac{4 \cdot d2_{\text{beam}}}{b} \right) - 1 \right) \quad \delta_2 = 2.767 \mu\text{m} \quad \delta_1 + \delta_2 = 6.723 \mu\text{m}$$

Calculate the normal stiffness.

$$k := \pi \cdot 2 \cdot \frac{w_{\text{beam}}}{2} \cdot \left[\frac{1 - (\nu_{\text{sleeve}})^2}{E_{\text{sleeve}}} \cdot \left(2 \cdot \ln \left(\frac{4 \cdot d1_{\text{beam}}}{b} \right) - 1 \right) + \frac{1 - (\nu_{\text{ferrule}})^2}{E_{\text{ferrule}}} \cdot \left(2 \cdot \ln \left(\frac{4 \cdot d2_{\text{beam}}}{b} \right) - 1 \right) - \frac{1}{E_C} \right]^{-1}$$

$$k = 37.397 \frac{\text{N}}{\mu\text{m}} \quad k = 0.214 \frac{\text{lbf}}{\mu\text{in}}$$